Trapping Rydberg Atoms in Ponderomotive Optical Lattices

by

Sarah Elizabeth Anderson

A dissertation submitted in partial fulfillment
of the requirements for the degree of
Doctor of Philosophy
(Physics)
in The University of Michigan
2014

Doctoral Committee:

Professor Georg A. Raithel, Chair
Professor Paul R. Berman
Assistant Professor Hui Deng
Professor Roseanne J. Sension

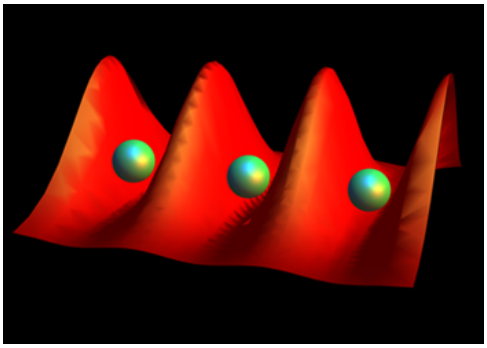

Illustration of Rydberg atoms trapped in the periodic wells of a ponderomotive optical lattice.

For my wonderfully supportive family, especially my parents Susan and Craig

ACKNOWLEDGEMENTS

I must first of all acknowledge my advisor, Georg Raithel, whose help and guidance have made this work possible. Georg's keen physical insight continually amazes me, and his passion for science is inspirational, as it is rivaled only by his love for sailing. Despite being the Principal Investigator on numerous projects in the lab, and having teaching and committee responsibilities besides, Georg is able to remember the detailed numbers associated with each project. He finds the time to stop by the lab daily to check on how things are going and to patiently explain a difficult concept or give advice in troubleshooting. His good-natured disposition and sense of humor have made my work in the lab not only productive, but fun. I am very grateful for his help and influence as a mentor.

Thank you to Professor Paul Berman, Assistant Professor Hui Deng, and Professor Roseanne Sension for serving on my dissertation committee. I would also like to thank Cory Lindh, Stephanie Miller, Kaitlin Moore, and Andrew Schwarzkopf for proofreading this thesis and for their thoughtful feedback.

The other members of the Raithel lab whose work overlapped with mine provided comradery and a willingness to help that made my time in the lab enjoyable and productive. In particular, I am grateful to David Anderson, Yun-Jhih Chen, Cornelius Hempel, Stephanie Miller, Kaitlin Moore, Eric Paradis, Rachel Sapiro, Andrew Schwarzkopf, Nithiwadee Thaicharoen, Mallory Traxler, Kelly Younge, and Stefan Zigo. Kelly, thank you for all of the insight and advice you have shared with me from my first day in the lab until now. Early on, the training I received from you gave me

the best possible start on this project, and I appreciate your continued friendship. To those who will carry on POL projects from here, Yun-Jhih and Kaitlin, it has been my pleasure to collaborate with each of you, and I look forward to seeing what you will accomplish! Mallory, you have made the lab a brighter place by consistently and thoughtfully remembering everyone's birthdays. Stephanie, your grimacing smiles always make me laugh. Eric, I appreciate the hours you spent tweaking up the blue laser. Andy, thanks for your assistance over the years as Raithel Lab Electronics Guru and for your heroic contributions in helping me format my references for this thesis. Dave, thanks for being my travel buddy in Brazil (the steakhouses and sea turtles remain fond memories) and also for being there for me when I had that migraine.

Enduring the ordeals of Jackson and qualifying exams in our first year formed a tight bond in our cohort, and I am especially grateful for those who have remained true friends throughout the years of graduate school. Joe, thank you for your input on countless practice talks and dozens of paper drafts, not to mention the dinners, rides to the airport, your company in the ER, and your listening ear when I ramble. Michelle, I don't know where I would be without your female understanding and moral support, often expressed over bubble tea. Thank you for being a caring friend, for washing all my dishes and taking out my trash when I sprained my ankle. Bo, thank you for your empathetic encouragement at critical moments. I've also so enjoyed our mutual appreciation of Wendy's lunches, neighborhood walks, Downton Abbey, and Michigan football games.

My undergraduate physics professors, Brian Beecken, Thomas Greenlee, Chad Hoyt, Richard Peterson, and Keith Stein, provided quality physics instruction and a belief in me that prepared and encouraged me to tackle this undertaking of graduate school. I am especially grateful for their influence as role models who both work and live well. Dr. Peterson, thank you for your willing counsel and wise words. Chad, thanks for giving me my start in AMO and supporting me by attending many of my

conference talks.

I am blessed to be surrounded by many others outside the realm of physics who have supported me through this venture, people who I won't name at length at the risk of filling up too many pages, but hopefully you know who you are.

Finally, the support and investment that I have received from my family began long before I entered graduate school, and I certainly would not be where I am without their consistent encouragement and care. I hardly know where to begin to express my gratitude, especially to my parents Susan and Craig. Thank you Mom and Dad for your unwavering love, support, and sacrifice for me. You have enabled me to accomplish what I have, and it is to you that I dedicate this work.

TABLE OF CONTENTS

LIST OF FIGURES

Figure

LIST OF TABLES

LIST OF APPENDICES

Appendix

LIST OF ABBREVIATIONS

AOMs acousto-optic modulators

EOM electro-optic modulator

ECDL external cavity diode laser

FWHM full-width at half maximum of the intensity profile

MOT magneto-optical trap

MCP microchannel plate

PM polarization-maintaining

POL ponderomotive optical lattice

QED quantum electrodynamics

ABSTRACT

Trapping Rydberg Atoms in Ponderomotive Optical Lattices

by

Sarah E. Anderson

Chair: Georg Raithel

I examine the trapping of Rydberg atoms in an optical standing wave. This trap, called an optical lattice, offers a platform for utilizing Rydberg atoms and their unique properties in applications such as atomic spectroscopy and quantum computing. Toward this end, I demonstrate the capability to trap ^{85}Rb Rydberg atoms in a one-dimensional 1064 nm wavelength optical lattice with high efficiency. I have achieved a 90% trapping efficiency by inverting the lattice immediately after Rydberg-atom excitation, using an electro-optic technique. In addition, I investigate the dependence of optical-lattice trapping potentials for Rydberg atoms on the angular portion of the atomic wavefunction. While ground-state atoms are point-like in relation to an optical-lattice field, Rydberg-atom wavefunctions extend over a substantial fraction of the lattice period, leading to an angular dependence of the lattice trapping potentials. I measure the potentials using various angular sublevels of Rydberg nD states prepared in the optical lattice with a superimposed transverse DC electric field. This unique angular dependence of Rydberg-atom optical lattices may be exploited to tailor the trapping potentials as needed for spectroscopy or quantum computing. Further, atom loss due to lattice-induced photoionization of Rydberg atoms must be

characterized for applications. I investigate the photoionization process as a function of position within the volume of a Rydberg atom. Since Rydberg-atom sizes approximately equal the lattice period, the lattice intensity varies maximally within the atomic volume. I find that photoionization rates are higher for lattice intensity maxima located near the nucleus than within the lobes of the electronic probability distribution. Photoionization therefore occurs near the Rydberg-atom nucleus. Finally, I calculate photoionization rates for Rydberg atoms in optical fields and investigate how these rates relate to the validity of the electric dipole approximation. This approximation is usually central to matter-field interactions, and Rydberg atoms in optical fields present a system for studying the approximation in a limiting case. I further apply the photoionization calculations to experimentally-relevant conditions. With these advances, this thesis lays essential groundwork for the employment of Rydberg-atom optical lattices in applications.

CHAPTER I

Introduction

1.1 Background and motivation

Rydberg atoms are atoms in highly excited states, in which a valence electron is loosely bound at a large radial separation from the positive ionic core. First observed in an astronomical context, Rydberg atoms have only been studied in a laboratory setting since the advent of the laser, which allows for straightforward excitation of ground-state atoms to Rydberg states. When in Rydberg states, atoms exhibit exaggerated properties that arise since the Rydberg electron is so far removed from the ionic core. These properties include large sizes that can be on the order of a micrometer, long lifetimes in the range of microseconds to milliseconds, and an exquisite sensitivity to external fields. Due to these unique properties and their potential applications, a growing number of researchers are utilizing Rydberg atoms in a diverse array of studies.

One of the exaggerated properties of Rydberg atoms that has attracted considerable interest for applications is the strong interactions between Rydberg atoms. Due to their large sizes, Rydberg atoms exhibit strong van der Waals or dipole-dipole interactions that are easily tuned by applying static electric fields or by choice of atomic state [1]. An application in which the interactions between Rydberg atoms are exploited, and which has been a major motivating force behind recent Rydberg-

atom research, is quantum computing [2–4]. In quantum computing schemes that involve Rydberg atoms, the quantum bit (qubit) is formed by two hyperfine ground-state levels, and two-qubit gate operations are performed by exciting the atoms to Rydberg states. While in Rydberg states, the atoms interact strongly, enabling fast gate operations. After completion of the gate operation, the atoms are returned to the ground-state levels for storage of the information, since in the ground-state levels the atoms interact only weakly with the environment and each other. Rydberg atoms are therefore ideal for quantum computing because their interactions are strong and controllable. Recent experimental progress towards the implementation of Rydberg atoms in quantum computing applications includes a demonstration of entanglement between Rydberg atoms, a phase gate, and a controlled-NOT gate [5–7].

The strong interactions between Rydberg atoms also facilitate studies of many-body physics [8]. Simply by laser-exciting a gas of atoms to Rydberg states, strongly correlated many-body states are created, in which a Rydberg excitation is shared coherently among a large number of atoms. This entangled many-body state can give rise to a spatially-ordered "crystalline" structure of Rydberg excitations in the otherwise disordered gas [9, 10]. Rydberg atoms therefore enable exotic phases of matter [11] that allow for such studies as the generation of light-matter entanglement [12], disorder in many-body systems [13], and universal quantum simulation [14].

The extreme sensitivity of Rydberg atoms to electric fields makes them advantageous for applications in field sensing. Rydberg atoms are excellent sensors for DC electric fields. The static polarizability of a Rydberg atom scales strongly with the principal quantum number n, being proportional to n^7, and reaches values of about 1 GHz/(V/cm)^2 at $n = 70$. Furthermore, Rydberg atoms are quite sensitive to microwave fields. Transitions between nearby Rydberg states have frequencies in the GHz$-$THz frequency range and dipole moments that scale with n^2, giving values of $\sim 10^{-26}$ C·m near $n = 60$. Rydberg atoms have been employed in measurements of

microwave fields as small as ~ 8 μV cm^{-1} [15] and DC fields of ~ 20 μV cm^{-1} [16].

Rydberg atoms provide excellent opportunities for tests of fundamental physics. High-precision spectroscopy of circular Rydberg states, which are states of maximal angular momentum and are described in the next section, would allow for a measurement of the Rydberg constant that does not depend heavily on quantum electrodynamics (QED) corrections. Comparing the measured Rydberg constant to previous measurements based on other methods that do rely on QED corrections gives a valuable test of the theories of QED [17]. In addition, Rydberg states play a role in anti-hydrogen trapping experiments at the CERN laboratory in Switzerland. Through a three-body recombination process in these experiments, anti-protons and positrons combine to form Rydberg states of anti-hydrogen that eventually decay to their ground-state in the trap. Comparing spectroscopic studies of anti-hydrogen to those of hydrogen provides a test of charge conjugation, parity, and time reversal invariance (CPT theory) [18, 19].

There is yet a broad scope of phenomena in physics beyond the applications already mentioned whose investigation is made possible by Rydberg atoms. Since Rydberg atoms are nearly macroscopic objects at the boundary of the quantum and classical regimes, they are used to study this cross-over region. For example, single Rydberg atoms have been entangled with microwave photons in a superconducting cavity, allowing for the study of entanglement, decoherence, and the quantum-to-classical boundary [12, 20, 21]. S. Haroche shared the 2012 Nobel Prize in Physics for this work. Rydberg atoms are also intimately tied into plasma studies. Three-body recombination in a plasma forms Rydberg atoms, and ionization of a Rydberg-atom gas presents a channel through which a plasma is formed [22]. Ionization of a spatially-ordered "crystal" of Rydberg excitations may present a pathway to achieve ordered structures within the plasma and thereby to reach deeply into the strong-coupling regime, a regime as of yet difficult to achieve [23]. As a final example of the versatil-

ity of Rydberg atoms, the scattering of a ground-state atom from a Rydberg electron can result in a novel molecular binding mechanism. The Rydberg and ground-state atom pair form a molecule, which bears the name of a "trilobite" since the electronic wavefunction in such a molecular state resembles this prehistoric creature [24]. This is the first known homonuclear molecule to have a permanent electric dipole moment, which may allow for easy manipulation and control of the molecule [25]. Rydberg atoms and their exaggerated properties thus offer a versatile platform for promising applications as well as for rich explorations of fundamental physics.

In order to take full advantage of the unique properties of Rydberg atoms for the studies described above, we must have a way to confine the Rydberg atoms. For example, in quantum computing protocols utilizing Rydberg states, a trap for the atoms would allow for multiple, sequential gate operations using the same atoms. In the applications of electric field sensing and high-precision measurements, a mechanism for trapping the Rydberg atoms would allow for maximal atom-field interaction times and thus for maximal precision and accuracy. In high-precision measurements, the atoms would be confined in a region where stray fields have been carefully minimized, reducing systematic uncertainties. This thesis focuses on the development of a trap for Rydberg atoms that allows us to confine and manipulate the atoms as needed for applications. This trap is called a ponderomotive optical lattice. In the rest of this chapter, I will first discuss some properties of Rydberg atoms in Section 1.2, ones that make Rydberg atoms so attractive for applications. In Section 1.3, I will review the types of Rydberg-atom traps that have been demonstrated to date and will introduce the ponderomotive optical lattice, which is the type of Rydberg trap developed in my work. The layout of the thesis is given in Section 1.4.

1.2 Properties of Rydberg atoms

It is the unique properties of Rydberg atoms that afford the abundant and varied opportunities for study mentioned already in the Introduction. In this section, these properties of Rydberg atoms are derived and summarized.

1.2.1 Scaling laws

Since Rydberg atoms, with their large values of the principal quantum number n, approach the classical limit, the classical Bohr model of the atom explains many of the interesting properties of Rydberg atoms and allows us to derive scaling laws for these properties. In the Bohr picture of the atom, an electron with mass $m_{\rm e}$ and charge $-e$ revolves in a classical circular orbit around the nuclear core of charge Ze. This orbit is described using Newton's second law,

$$\frac{m_{\rm e}v^2}{r} = \frac{Ze^2}{4\pi\epsilon_0 r^2}, \tag{1.1}$$

where r is the radius of the electron's orbit and v is its velocity. In this section, I will consider Rydberg states of the hydrogen atom, for which $Z = +1$. With quantization of angular momentum, $m_{\rm e}vr = n\hbar$, the radius of a Rydberg atom follows from Equation 1.1,

$$r = \frac{n^2\hbar^2 4\pi\epsilon_0}{e^2 m_{\rm e}}. \tag{1.2}$$

The orbital radius of the Rydberg electron therefore scales as n^2, illustrating how Rydberg atoms can attain large, almost macroscopic sizes.

To find the energy of the Rydberg electron, which I denote by $W_{\rm b}$, I sum its kinetic and potential energy. Using Equation 1.2 for r, I find that

$$W_{\rm b} = \frac{1}{2}m_{\rm e}v^2 - \frac{e^2}{4\pi\epsilon_0 r} = -\frac{e^4 m_{\rm e}}{2n^2\hbar^2(4\pi\epsilon_0)^2}. \tag{1.3}$$

The energy is negative, since the electron is bound to the atom, and scales as n^{-2}. With the Rydberg constant defined as $Ry \equiv (e^4 m_\mathrm{e})/[2\hbar^2(4\pi\epsilon_0)^2]$, the expression for the binding energy of the Rydberg electron becomes $W_\mathrm{b} = -Ry/n^2$. In atomic units, the binding energy is expressed $W_\mathrm{b} = -1/(2n^2)$ (for a note about atomic units, see Appendix A). For large n, the binding energy of the Rydberg electron becomes very small, which is essential for understanding the mechanism for Rydberg-atom trapping that this work is based on and that is discussed in Section 1.3.2. These first two scaling laws for the orbital radius and binding energy of the Rydberg electron therefore illustrate the picture that a Rydberg atom is characterized by a loosely bound electron orbiting the ionic core in a large trajectory.

Several other scaling laws for Rydberg-atom properties that underpin the work in this thesis can be derived from the simple model given above. The Kepler frequency, which describes the orbital frequency of the Rydberg electron and also gives the frequency spacing between adjacent n manifolds of states, can be obtained by $\omega_K = v/r$. Using the condition of quantization of angular momentum and Equation 1.2, the Kepler frequency is

$$\omega_\mathrm{K} = \frac{m_\mathrm{e}}{n^3\hbar^3}\left(\frac{e^2}{4\pi\epsilon_0}\right)^2.$$

The Kepler frequency therefore scales as n^{-3}. This frequency will be a consideration in Section 1.3.2, where I derive trapping potentials for Rydberg atoms in the ponderomotive optical lattice, as well as in Section 6.4.2, where I consider the case of very deep trapping potentials.

A commonly cited, exaggerated property of Rydberg atoms is their long lifetimes, which enable, for example, long atom-field interaction times in high-precision spectroscopic measurements. For low angular momentum (low-ℓ) Rydberg states, which are the states under consideration in this thesis, the scaling of the lifetimes can be considered classically using the orbital period of the Rydberg electron, $T = (2\pi)/\omega_\mathrm{K}$. This

method assumes that the Rydberg electron is most likely to decay to a low-lying orbit when the electron is undergoing maximal acceleration at the inner turning point of its orbit, near the nucleus (for discussions of such an argument, see Section 5.3). With the scaling of the Kepler frequency found above, the lifetime T for these low-ℓ states therefore scales as n^3. A proper derivation of the scaling laws for Rydberg lifetimes requires a quantum mechanical treatment, using the Coulombic wavefunctions and the Einstein A coefficient that describes spontaneous emission [26]. After a proper quantum mechanical treatment, the lifetime of the low-ℓ states is still found to scale as n^3, while the high-ℓ states decay more slowly, with lifetimes that tend to scale as n^5.

Since the Rydberg electron is loosely bound and far removed from the ionic core, it is extremely sensitive to external fields. For example, the electron is easily ionized by DC electric fields. The ionization electric field is derived from the Coulomb-Stark potential for the Rydberg electron, which is given in atomic units and for the electric field E along the z direction as

$$V_{\mathrm{CS}} = -\frac{1}{|z|} + Ez.$$

There is a saddle point in the potential at $V_{\mathrm{CS}} = -2\sqrt{E}$. An electron with energy above this potential will ionize. Setting this saddle point energy equal to the binding energy, $W_{\mathrm{b}} = -1/(2n^2)$, one finds that the atoms will ionize in electric field values of $E = 1/(16n^4)$. The ionization of Rydberg atoms by DC fields will be central to the detection of Rydberg atoms in this thesis, as will be discussed in Section 2.2.2.

Some of the scaling laws for Rydberg-atom properties that play important roles in this thesis are summarized in Table 1.1. I provide some additional laws to those derived in this section.

Table 1.1: Rydberg-atom scaling laws. The variable d is atom-atom distance.

Orbital radius	n^2
Radiative lifetime (low-ℓ)	n^3
Kepler frequency	n^{-3}
Ionization electric field	n^{-4}
DC polarizability	n^7
Transition dipole moment	n^2
Van der Waals interactions	n^{11}/d^6
Electric dipole interactions	n^4/d^3

1.2.2 Quantum defects

The work in this thesis is performed with the alkali metal rubidium (Rb). Rydberg states of the alkali metals, such as Rb, are very similar to Rydberg states of hydrogen, since the alkali-metal Rydberg electron orbits an ionic core of charge +1. Differences between the alkali and hydrogenic cases arise from the finite size of the ionic core for the alkali metals, which for Rb consists of the nucleus and 36 electrons. For low-ℓ Rydberg states of the alkali metals, the Rydberg electron can both penetrate and polarize the ionic core. The wavefunctions and energies of the alkali metals are modified by the interaction with the core in comparison to the case of hydrogen. The wavefunctions acquire a phase factor that can give rise to effects such as a Cooper minimum in the photoionization cross sections of the alkali Rydberg states, which for Rb is from Rydberg S states into P states in the continuum (see Sections 3.4.3 and 6.4, as well as Reference [26]). The energies of the alkali Rydberg states are depressed in comparison to those of hydrogen. These modifications of the energies and wavefunctions by the interaction with the core are taken into account through the use of an empirically determined correction factor to the principal quantum number, called a quantum defect. Alkali Rydberg states are then described by the same equations as hydrogen, but with the principal quantum number replaced by an effective principal quantum number $n^* = n - \delta_\ell$, where δ_ℓ is the quantum defect. For example, the energies of the alkali Rydberg states are then given by $W_\mathrm{b} = -1/(2n^{*2})$ and the

ionization electric fields by $E = 1/(16n^{*4})$. For Rb, the δ_ℓ values are 3.13 for S states, 2.65 for P states, 1.35 for D states, and 0.02 for F states [27].

For high-ℓ states, the Rydberg electron does not penetrate the core, and the quantum defects arise from effects due to polarization of the core. The quantum defects for the high-ℓ states are given by $\delta_\ell = \frac{3}{4}\frac{\alpha_\mathrm{D}}{\ell^5}$ [28], where α_D is the dipolar polarizability of the ionic core and is equal to 9.2 atomic units for Rb [29]. The quantum defects for the high-ℓ states are generally very small and are often negligible in experiments. These high-ℓ states with near-zero quantum defects are consequently referred to as the "hydrogenic" states, since they are essentially like the states of hydrogen. Special cases of high-ℓ states that will be of interest in later chapters of this thesis are those of maximal angular momentum, with quantum numbers $|m| = \ell = n - 1$. These states are referred to as "circular" Rydberg states, because their wavefunctions take the form of a thin torus encircling the ionic core. Circular Rydberg states come very close to a Bohr-model-like atom. Such states will be important in Section 7.3.

1.3 Rydberg-atom trapping

As mentioned in the Introduction, a trapping mechanism for Rydberg atoms would allow us to make use of Rydberg-atom properties in such applications as quantum computing [30], high-precision spectroscopy [31], field sensing [15], and many-body physics [11]. An example of the need for a Rydberg-atom trap is found in quantum computing schemes involving neutral atoms excited to Rydberg states. In experiments that have demonstrated two-qubit quantum gates based on Rydberg excitations of two atoms in neighboring ground-state optical dipole traps (see Section 2.1.2), the trapping light was turned off while the gate operations were performed since the trapping light was repulsive for the Rydberg states [6, 7, 32]. However, turning off the ground-state trapping light is not scalable for larger arrays of atom traps,

which are envisioned to be created by diffractive optics. It is impractical to turn off the trapping light for an entire array of atoms in order to perform a gate operation between two atoms within the larger array. Instead, it is desirable to develop a trap for Rydberg atoms that is compatible with traps for ground-state atoms. Furthermore, a trap that provides identical potentials for both the ground and Rydberg states in quantum computing schemes would reduce motional decoherence [30, 33], which is due to entanglement of the atom's internal state with its external degrees of freedom and is induced by a change in vibrational state of the atom in the trap.

1.3.1 Previous work on Rydberg-atom traps

Rydberg-atom traps that have been proposed or realized mainly involve static electric or magnetic fields. Rydberg-atom trapping was first proposed by W. Wing [34] and T. Breeden and H. Metcalf [35] in the early 1980s, who suggested using static electric fields and the Stark effect to confine the atoms. F. Merkt and co-workers realized a trap for Rydberg atoms based on these proposals in 2008, trapping low-field-seeking Rydberg states in a static three-dimensional electric field minimum [36]. The first trap for Rydberg atoms was demonstrated in the Raithel research group in 2005 using an Ioffe-Pritchard style trap with magnetic fields of strength 3 T at the trap minimum [37]. Rather recently, circular Rydberg states were also confined in a magnetic trap (with fields $\sim$ 10 G) in the Raithel lab, making use of the large magnetic moments of these states [38]. P. Schmelcher and I. Levanovsky have studied quadrupole magnetic field traps for Rydberg atoms in theoretical detail [39]. These electro- or magneto-static Rydberg-atom traps have some significant associated drawbacks, however. Trap-induced shifts to the atomic energy levels can reach several GHz, which is detrimental for applications in quantum computing or high-precision spectroscopy. Furthermore, these traps are not universal traps for all Rydberg states.

An alternative type of trap for Rydberg atoms involves optical fields, a trapping

mechanism first proposed by the Raithel group [40]. An optical trap for Rydberg atoms offers the benefit of small trap-induced level shifts in comparison to the static-field traps. These shifts are on the order of MHz in my work, although the shifts could be reduced further by lowering trap depth and atom temperature. Minimal trap-induced shifts are important to applications in high-precision measurements, in which certain correction factors to measured transition frequencies scale with absolute trap depth. Optical traps further afford flexibility in selecting and modifying trap parameters. For example, the wavelength of the trapping light can be tuned to minimize trap-induced shifts on transitions of interest (i.e. achieve a trap with "magic" wavelength [33]), which is crucial to quantum computing for minimizing motional decoherence as mentioned earlier. Optical traps are also universal traps for all Rydberg states. While optical traps have been widely known and utilized for ground-state atoms in a breadth of applications, they have never before been used for Rydberg atoms. Here, I extend the benefits of optical traps to Rydberg states.

In this thesis, I study the trapping of Rydberg atoms in the standing waves of interfering laser beams, a trap called an optical lattice. Reference [41] provided the first evidence of Rydberg-trapping in an optical lattice; this was initial work performed in the Raithel research group. In these previous studies, the Rydberg-atom trapping efficiency was limited to about 5%. In my work, I develop and characterize the first efficient optical Rydberg-atom trap. Thus, my work provides a new tool for exploiting the unique properties of Rydberg atoms and lays essential groundwork for the employment of optical Rydberg-atom traps in the applications discussed here and in Section 1.1.

1.3.2 Rydberg atoms in ponderomotive potentials

Optical lattices for Rydberg atoms are similar to conventional optical lattices for ground-state atoms. Both consist of a periodic array of wavelength-size potential wells

made by the standing waves of interfering laser beams. The trapping mechanism for Rydberg atoms in optical lattices, however, is distinct from that for ground-state atoms. An optical lattice for ground-state atoms acts on a field-induced dipole created by coupling nearby bound states (see Section 2.1.2). Transitions between Rydberg states, however, are not in the optical regime, and Rydberg atoms do not couple significantly to other levels in optical fields. Instead, the trapping mechanism for Rydberg atoms in an optical lattice utilizes the oscillating electric field in the optical standing waves to create a ponderomotive potential that acts on the quasi-free Rydberg electron.

The ponderomotive potential can be understood by considering the motion of a free electron in a rapidly oscillating electric field [42, 43]. In the oscillating field, the free electron undergoes a quiver motion as its charge is driven by the field. The energy of the electron in the field is raised by an amount equal to its time-averaged kinetic energy; this is known as the ponderomotive potential. In a laser field of the form $\mathbf{E} = \hat{\mathbf{x}} E_0 \cos(\omega t)$, with electric-field amplitude E_0 and angular frequency ω, the motion of the electron follows from Newton's second law, $\ddot{x} = -\frac{e}{m_\mathrm{e}} E_0 \cos(\omega t)$, and therefore, $\dot{x} = -\frac{e}{m_\mathrm{e}\omega} E_0 \sin(\omega t)$. The time-averaged kinetic energy of the electron in the field is

$$\langle KE \rangle_\mathrm{T} = \frac{\omega}{2\pi} \int_0^{2\pi/\omega} \frac{1}{2} m_\mathrm{e} \dot{x}^2 \, dt = \frac{\omega}{2\pi} \frac{e^2 E_0^2}{2 m_\mathrm{e} \omega^2} \int_0^{2\pi/\omega} \sin^2(\omega t) \, dt,$$

and the expression for the ponderomotive potential for the free electron is consequently

$$V_\mathrm{p} = \frac{e^2 E_0^2}{4 m_\mathrm{e} \omega^2}. \tag{1.4}$$

Aside from considering the time-averaged kinetic energy of the free electron in an oscillating field, another way to derive the ponderomotive potential for a free electron

is from the minimal coupling Hamiltonian, in which the interaction of the electron with the field is taken into account by replacing $\mathbf{p}$ with $\mathbf{p} + |e|\mathbf{A}$ [44, 45]. Here, $\mathbf{A}$ is the vector potential for the field, which is related to a source-free radiation field by $\mathbf{A}(\mathbf{r}, t) = -\frac{\partial \mathbf{E}(\mathbf{r},t)}{\partial t}$ [46]. For a free electron, the Hamiltonian is simply given by its kinetic energy, $H = \frac{\mathbf{p}^2}{2m_\mathrm{e}}$. With $\mathbf{p}$ replaced with $\mathbf{p} + |e|\mathbf{A}$, the minimal coupling Hamiltonian is

$$H = \frac{[\mathbf{p} + |e|\mathbf{A}(\mathbf{r}, t)]^2}{2m_\mathrm{e}}.$$

The vector potential for a plane-wave electromagnetic field propagating in the z direction and polarized in the x direction is given by $\mathbf{A}(z, t) = \hat{\mathbf{x}}\frac{E_0}{2i\omega}[e^{i(kz-\omega t)} + e^{-i(kz-\omega t)}]$, where k is the wavenumber. When this expression for the vector potential is inserted into the minimal coupling Hamiltonian, the ponderomotive potential arises from the portion that is proportional to $\mathbf{A}^2$. This portion describes two-photon processes and is given by

$$\frac{e^2 E_0^2}{8m_\mathrm{e}\omega^2}[e^{2i(kz-\omega t)} + e^{-2i(kz-\omega t)} + 2].$$

The first and second terms above are energy non-conserving terms that describe two-photon absorption and two-photon emission, respectively. These energy non-conserving terms are negligible in my work. The third term above is an energy-conserving term that corresponds to absorption and emission of a photon and gives rise to the ponderomotive potential of Equation 1.4.

In an optical lattice, the electric field is periodic in space, and the ponderomotive potential is therefore also periodic in space. For a one-dimensional optical lattice formed by two counter-propagating laser beams, the electric field is of the form $\mathbf{E}(z, t) = \hat{\mathbf{x}}2E_0 \cos(kz)\cos(\omega t)$, for laser beam propagation in the z direction, linear polarization in the x direction, and single-beam electric field amplitude E_0. The

corresponding ponderomotive lattice potential is given by

$$V_{\mathrm{p}}(z) = \frac{e^2 E_0^2}{2 m_{\mathrm{e}} \omega^2}[1 + \cos(2kz)]. \tag{1.5}$$

The resultant gradient force, $\mathbf{F}_{\mathrm{p}} = -\nabla V_{\mathrm{p}}$, in the lattice pushes the free electrons towards regions of minimum intensity. Ponderomotive effects of optical lattices on electrons have been demonstrated in Kapitza-Dirac scattering of free electrons [47] and above-threshold ionization [42]. Other phenomena where ponderomotive effects on charged particles play a role include Paul traps for ions [48] and the generation of high harmonics and x-rays in strong fields [49, 50].

In the case of a Rydberg atom, the Rydberg electron is so loosely bound that it can be considered quasi-free. In an optical lattice, the quasi-free Rydberg electron experiences a periodic ponderomotive potential much like that which the free electron experiences. A simple picture that captures the essential physics is that the ponderomotive lattice potential traps the quasi-free Rydberg electron at lattice intensity minima, and the entire atom is then trapped since the Rydberg atom's ionic core is weakly bound to the Rydberg electron. Due to the central role of the ponderomotive potential in the trapping of Rydberg atoms in optical fields, an optical lattice for Rydberg atoms is called a ponderomotive optical lattice (POL) throughout this thesis.

To derive the trapping potential for the entire Rydberg atom in a ponderomotive optical lattice, the motion of the Rydberg atom in the optical field is described using three coordinates (indicated in Figure 1.1) that reflect three different, well-separated timescales of motion [40]. As will be described in the following, the distinct timescales of motion allow for application of the Born-Oppenheimer approximation, which takes into account the fast timescales of motion in the problem by adding a static potential to the Hamiltonian that governs the slower degrees of freedom [44].

As illustrated in Figure 1.1, the fastest timescale of motion for the Rydberg atom

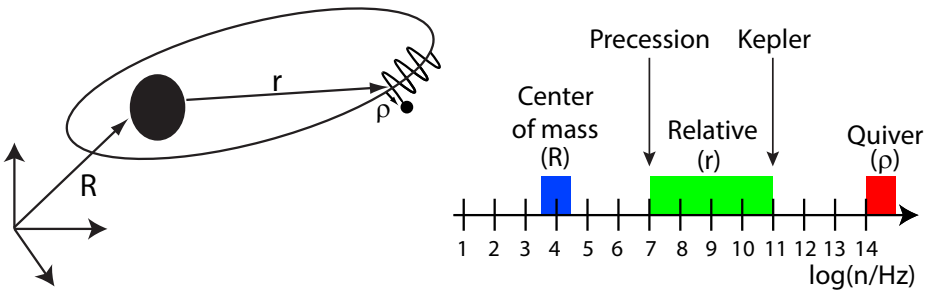

Figure 1.1: A Rydberg atom in an optical lattice is described using three coordinates, reflecting three timescales of motion. The quiver motion of the electron (ρ) evolves on the fastest timescale, followed by the relative motion of the electron (r) around the core. The center-of-mass motion of the atom in the optical potential (R) evolves on the slowest timescale. The three timescales of motion are separated by several orders of magnitude.

in the optical field is the quiver motion of the electron, described by the ρ coordinate. The quiver motion evolves at the frequency of the field, which is 2.8×10^{14} Hz for a 1064 nm laser field (which is the case in my work). The next slowest timescale of motion is the relative motion of the electron around the core of the atom, indicated by the r coordinate in Figure 1.1. The relative motion of the electron evolves on various timescales. The fastest relative motion is the Kepler motion of the electron around the core, which is at the Kepler frequency or 10^{11} Hz for $n = 40$. Slower frequencies of relative motion arise from precession of the electron orbit due to residual fields, as the classical Kepler orbit of the electron precesses in electric or magnetic fields. The frequency of the precession is at the Stark frequency, $\frac{3}{2}nE$ in atomic units, in electric fields, or at the Larmor frequency, $B/2$ in atomic units, in magnetic fields [51, 52]. Estimates of the fields in our setup yield precession frequencies of about 10^7 Hz [40]. After the relative motion, the slowest timescale of motion is the center-of-mass motion of the Rydberg atom in the optical potential. For our lattices, this timescale is on the order of 10^4 Hz, which is several orders of magnitude smaller than the slowest timescale for the relative motion of the electron.

Since the three timescales of motion described in Figure 1.1 are separated by

several orders of magnitude, the Born-Oppenheimer approximation may be applied twice to eliminate the quiver and relative motion of the electron and to find a potential for the center-of-mass of the atom. First, since the fastest timescale of relative motion is several orders of magnitude slower than the quiver motion of the electron, the Born-Oppenheimer approximation is applied to adiabatically eliminate the quiver motion of the electron. The quiver motion is then taken into account by adding the static ponderomotive potential V_{p} of Equation 1.5 to the Hamiltonian of the Rydberg atom. Second, since the center-of-mass motion is slower than the relative motion by several orders of magnitude, another application of the Born-Oppenheimer approximation eliminates the relative motion of the electron. The adiabatic potential for the center-of-mass of the Rydberg atom in the optical potential is then

$$V_{\mathrm{ad}}\left(\mathbf{R}\right) = \int d^3r \, V_{\mathrm{p}}\left(\mathbf{r}+\mathbf{R}\right) \left|\psi\left(\mathbf{r}\right)\right|^2. \tag{1.6}$$

Here, the uppercase $\mathbf{R}$ is the center-of-mass coordinate of the Rydberg atom, and the lowercase $\mathbf{r}$ is the relative coordinate of the Rydberg electron, as described in Figure 1.1. The V_{p} is the free-electron ponderomotive lattice potential from Equation 1.5, and ψ is the Rydberg wavefunction. The V_{ad} describe the trapping potentials for the Rydberg atoms in the ponderomotive optical lattice, and therefore Equation 1.6 is of central importance to this thesis. The trapping potentials for the Rydberg atoms in the optical lattice are given by a spatial average of the free-electron ponderomotive potential weighted by the Rydberg wavefunction. Calculations of adiabatic potentials, V_{ad}, are performed in Section 6.4.

The adiabatic potentials in the lattice are accompanied by lattice-induced state-mixing. The Rydberg wavefunction ψ in Equation 1.6 is generally a superposition of lattice-free atomic states, due to the state-mixing. For relatively low-intensity lattices ($\sim 10^6$ W/cm^2, corresponding to modulation potential depths of ~ 10 MHz for counter-propagating 1064 nm laser beams), the lattice induces some m-mixing, under

the absence of cylindrical symmetry, for states with $\ell > 0$; the lattices are shallow enough to avoid ℓ-mixing. For high-intensity lattices ($\sim 10^8$ W/cm^2, corresponding to modulation potential depths of ~ 1 GHz for counter-propagating 1064 nm laser beams), the lattice induces strong ℓ-mixing.

Lattice-induced state-mixing highlights a novel feature of the ponderomotive optical lattice for Rydberg atoms, which is the large number of nearly degenerate states (the degeneracy scales as n^2 for hydrogen). The lattice can therefore couple large numbers of states, and Rydberg wavefunctions in the lattice can be coherent superpositions of tens to hundreds of states. This coupling of many degenerate states gives rise to a complex structure of adiabatic potentials in the lattice [53]. Examples of these complex adiabatic potentials are shown and discussed in Section 6.4.2.

Another novel feature exhibited by the ponderomotive optical lattice arises from the size difference between Rydberg atoms and ground-state atoms in the lattice. Ground-state atoms can be considered as point-like in relation to the lattice potential well (sizes of $\sim 10^{-10}$ m and $\sim 10^{-7}$ m, respectively), whereas Rydberg atoms can have sizes on the same order as the lattice wells. The large size of the Rydberg atom means that the shape of its electronic probability distribution has a significant effect on the averaging in Equation 1.6. Rydberg atoms consequently experience unique state-dependent trapping potentials in the lattice. The state-dependence of the trapping potentials is illustrated in Figure 1.2 for two Rydberg S states of different principal quantum number. Generally, Rydberg atoms with larger spatial extents along the axis of the lattice experience shallower potentials in the lattice, since they average over more of the free-electron ponderomotive potential. Also generally, the Rydberg-atom center-of-mass is attracted to intensity minima in the lattice. There are special cases when the center-of-mass of the Rydberg atom is attracted to intensity maxima in the lattice, however; the trapping potentials are then "flipped" from the usual case (see illustration in Figure 5.5). This occurs when the size of the Rydberg atom

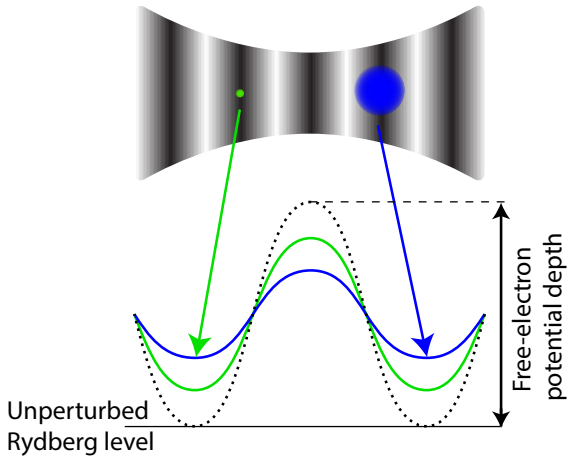

Figure 1.2: State-dependent trapping potentials for Rydberg atoms in a ponderomotive optical lattice (black indicates low intensity, white high intensity). Rydberg states with larger spatial extents in the direction of the lattice axis (blue) generally experience shallower trapping potentials.

approximately equals the lattice period. Such states are measured and discussed in Section 4.3.

The exact shape of the adiabatic trapping potentials in the lattice depends on all quantum numbers (n, ℓ, j, m_j), since these quantum numbers describe Rydberg wavefunctions with varying shapes that average over the free-electron ponderomotive potential differently. The state-dependence of the adiabatic potentials has been experimentally verified previously in the Raithel research group using spherically symmetric Rydberg nS states [41]. In Chapter IV, I extend the characterization to states with various angular distributions of the electronic probability distribution.

To summarize and emphasize the differences in ponderomotive optical lattices for Rydberg atoms compared to conventional optical lattices for ground-state atoms, the trapping mechanism for a Rydberg atom is fundamentally different in origin. Rydberg atoms are trapped by the ponderomotive potential acting on the quasi-free Rydberg electron. Further, since the ponderomotive potential is proportional to the square of the electric field, the potential results only from intensity gradients and not polarization gradients (as is the case, for example, for Sisyphus cooling of

ground-state atoms in optical lattices [54]). Due to the large size of Rydberg atoms in comparison to the optical lattice wells, Rydberg atoms experience state-dependent lattice trapping potentials. Due to the large number of degenerate Rydberg states, lattice-induced state-mixing can result in a rich structure of adiabatic potentials in the lattice.

As a final note about optical traps for Rydberg atoms, another type of optical Rydberg-atom trap has been proposed by M. Jones, T. Pohl, and co-workers [55]. This proposed type of optical trap is for alkaline-earth Rydberg atoms, which have two valence electrons and which would be confined in the optical fields using the polarizability of the non-Rydberg valence electron. This trapping mechanism is therefore also fundamentally different from that considered in this thesis.

1.4 Thesis framework

The objective of my work described in this thesis is to establish a ponderomotive optical lattice as an effective Rydberg-atom trap and to characterize the trap, thus paving the way for employment of the Rydberg-atom optical lattice system in applications. The framework of the thesis is as follows. I begin in Chapter II by explaining the experimental setup and procedure used throughout the thesis to prepare and detect Rydberg atoms in optical lattices. In Chapter III, I describe experiments that provide the first demonstration of highly efficient optical Rydberg-atom trapping. While the presence of trapped Rydberg atoms in the optical lattice had been detected earlier in our lab [41], the trapping efficiency in that work was limited to a few percent. This limitation was due to the Rydberg-atom preparation scheme, in which the atoms were excited to maxima in the lattice Rydberg-atom trapping potential. To overcome this obstacle and achieve efficient Rydberg-atom trapping, I implement a technique to rapidly invert the Rydberg-atom potential immediately following Rydberg-atom excitation, placing the potential minima at the location of

the excited atoms. This inversion technique results in a 90% trapping efficiency.

In Chapter IV, I measure the dependence of the ponderomotive optical lattice potentials for Rydberg atoms (the V_{ad} in Equation 1.6) on the angular portion of the Rydberg wavefunction. In previous work, the state-dependence of the potential was measured for Rydberg nS states with isotropic electronic wavefunctions [41]. I extend the characterization to Rydberg states with angular variation in their wavefunctions. States with wavefunctions that are elongated in the direction of the lattice axis are expected to have shallower potentials in the lattice than those elongated transverse to the lattice axis, since those elongated in the direction of the lattice axis can average over more of the free-electron ponderomotive potential in Equation 1.6. I measure lattice potential modulation depths for various Rydberg nD states and find them to vary substantially, in agreement with calculations. This result demonstrates how the Rydberg-atom trapping potentials may be tailored as needed for an application by choice of Rydberg state.

In Chapter V, I investigate the process by which Rydberg atoms may be photoionized by the lattice light. The motivation for this work is the agreement of measured photoionization rates for Rydberg atoms in optical fields with calculated rates based on the electric dipole approximation. This approximation is typically made when the wavelength of the light is much larger than the size of the atom; however, Rydberg-atom sizes may exceed the wavelength of the light. The apparent inconsistency can be resolved by arguing that the photoionization process for a Rydberg atom occurs near the nucleus, within a volume that is still small with respect to the wavelength of the light. While this argument has undergirded Rydberg-atom experiments for three decades, in this thesis I provide the first spatially-resolved study of the photoionization process within the volume of a Rydberg atom. I use the optical lattice as a maximally inhomogeneous field probe within the atom. The measured photoionization rates depend on the intensity near the center of the atom and not within the

lobes of the electronic probability distribution. A complete understanding of the photoionization process is important to applications of Rydberg atoms in optical traps, as it may either represent a loss mechanism from the trap or be exploited as a detection method.

In Chapter VI, I elaborate on the theoretical description of the photoionization of Rydberg atoms by optical fields and the role of the electric dipole approximation in these calculations. I derive and analyze expressions for the matrix elements and photoionization cross sections for Rydberg atoms in optical fields, without and with the dipole approximation. The results illustrate that Rydberg-atom photoionization rates are in good agreement with the dipole approximation because the matrix elements accumulate within a small volume near the nucleus. I also find conditions under which the dipole approximation breaks down. Further, I apply the results to consider photoionization effects in Rydberg-atom experiments in optical lattices of both low and high intensity.

Finally, in Chapter VII, I review the main accomplishments of this thesis and describe future directions for Rydberg-atom optical lattice experiments.

CHAPTER II

Experimental Apparatus and Techniques

The work in this thesis examines the trapping of cold Rydberg atoms in optical lattices. In this chapter, I describe the experimental process used throughout the thesis to prepare and detect samples of Rydberg atoms in an optical lattice. I first review the basics of ground-state atom trapping in magneto-optical traps (MOTs) and optical dipole traps, as these are two fundamental tools in this work which provide the launching point for the rest of the experiment. I then outline the procedure used to excite and detect Rydberg atoms as well as to align the optical lattice.

2.1 Laser cooling and trapping of ground-state atoms

The advent of laser cooling and trapping has revolutionized the study of ground-state atoms. The unique methods employed in the cooling and trapping of atoms have not only provided a new process for investigating atoms but also an unprecedented means for controlling them. The innovations involved in the development of laser cooling and trapping of atoms led the Nobel Prize in Physics to be awarded to S. Chu, C. Cohen-Tannoudji, and W. Phillips in 1997. In these innovative methods, laser light is used to exert forces on atoms, forces which can bring the atoms from speeds near that of sound to speeds near that of a mosquito. The forces that the laser light exerts on the atoms can be categorized into two types: a dissipative scattering force and a

conservative dipole force. The first laser-based trap for atoms that is discussed below, the magneto-optical trap, utilizes the scattering force; the second, the optical dipole trap, utilizes the dipole force.

2.1.1 Magneto-optical traps

Atoms within a gas at room temperature move with speeds of ≈ 300 m/s. These atoms may be slowed significantly by scattering a large number of photons, each of which have an associated momentum $p = \hbar k$. If an atomic beam is counter-propagating with a laser beam that has a frequency near an atomic resonance, atoms that absorb a photon will receive a momentum kick in the opposite direction of the atomic motion. Since photons are spontaneously re-emitted by the atoms in random directions, the momentum imparted to the atoms by the spontaneously emitted photons averages to zero over many scattering events. Therefore, by scattering many photons, the atoms experience an average force that slows them down [56]. The laser beam is then said to be "cooling" the atoms.

Using three pairs of counter-propagating laser beams, atoms may be cooled in three dimensions. In this configuration, the laser beams have a frequency (denoted by angular frequency ω) that is lower than the frequency of the atomic resonance (angular frequency ω_0). Atoms traveling toward a laser beam will be blue-shifted into resonance with that beam due to the Doppler shift, while atoms that are traveling away from a beam will be red-shifted further out of resonance with it. The atoms then preferentially scatter photons from the beam that they are traveling toward and are consequently slowed in their direction of motion. The force on the atoms is proportional to the velocity of the atoms, and the atoms move as if they are suspended in a viscous fluid. This configuration is therefore coined an "optical molasses" [57].

While the optical molasses slows the atoms in all directions of motion, it does not provide a position-dependent restoring force that confines the atoms. This is achieved

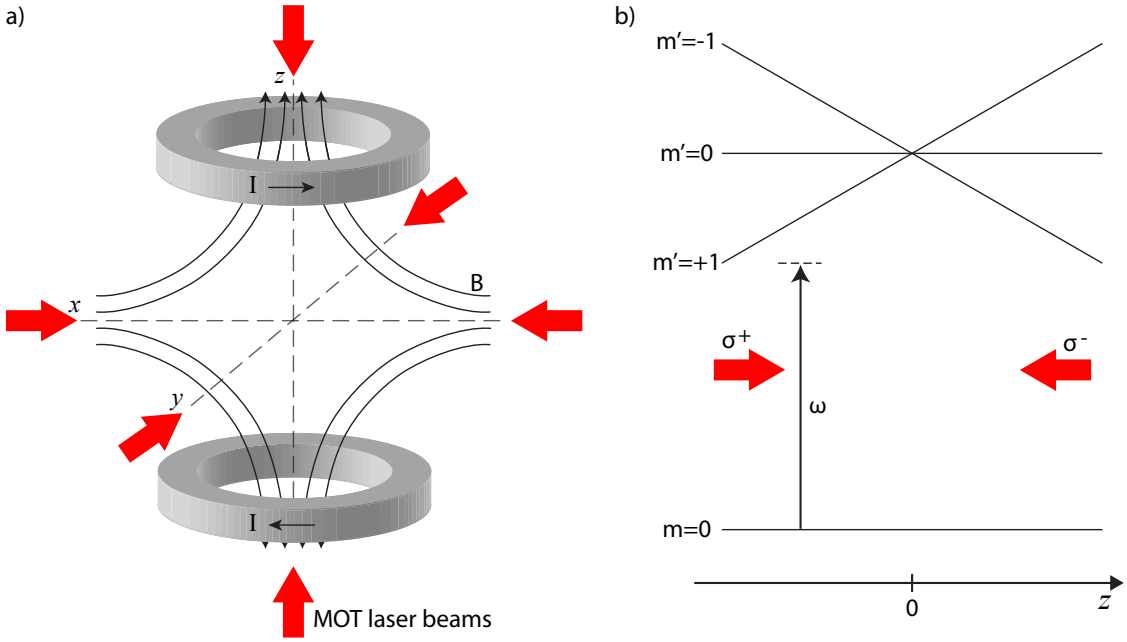

Figure 2.1: a) Magnetic field (B) and laser beam configuration for a magneto-optical trap. b) Level diagram illustrating the operating principle of a magneto-optical trap. The atomic energy levels are shifted by the magnetic field. The laser polarizations shown are relative to the z-axis. The polarizations are chosen such that an atom displaced from trap center preferentially scatters photons from the laser beam that pushes the atoms back towards trap center.

through the addition of an inhomogeneous magnetic field and circular polarization of the laser beams. The magnetic field is a quadrupole field of the form ($\frac{\alpha}{2}x$, $\frac{\alpha}{2}y$, $-\alpha z$), created by two current-carrying coils arranged in an anti-Helmholtz configuration [currents flowing in opposite directions, see Figure 2.1(a)]. Typically, $\alpha \approx 20$ G/cm. The atomic energy levels are shifted by the magnetic field using the Zeeman effect and vary with position, creating a spatially-dependent resonance condition. As illustrated in Figure 2.1(b), for atoms displaced from the field zero in the $+z$-direction, the laser frequency ω is closer to resonance with the $\Delta m = -1$ transition. The atoms therefore preferentially scatter photons from the σ^--polarized beam, since by selection rules $\Delta m = -1$ for σ^- polarized light. The atoms are then driven back to the field zero. The same holds if the atoms drift to $-z$. The atoms then preferentially scatter photons from the σ^+ beam. Thus, the atoms always experience a restoring force towards the field zero. Due to the combined action of the magnetic field and the optical fields, this atom trap is called a magneto-optical trap (MOT) [58]. Most MOTs are operated with alkali-metal elements, due their high vapor pressure, simple level structure that offers a nearly-closed cycling transition (see below), and atomic resonances with frequencies that are readily available in low-cost laser diodes.

In the experiments presented in this thesis, I begin by cooling and trapping rubidium 85 in a MOT. The MOT light has a wavelength of about 780 nm and is about 10 MHz red-detuned from the $5S_{1/2}, F = 3 \rightarrow 5P_{3/2}, F' = 4$ transition (see Figure 2.2). This transition is referred to as the cycling transition. Since the splitting between $5P_{3/2}, F' = 4$ and $5P_{3/2}, F' = 3$ is only ≈ 120 MHz, about one out of every 1,600 scattering events results in population that decays from $5P_{3/2}, F' = 3$ into $5S_{1/2}, F = 2$. This level is 3 GHz detuned from the cycling transition and is a so-called "dark state" since it is inaccessible to the cycling transition laser frequency. Atoms in this state are no longer being cooled or trapped by the MOT. To reintroduce the atoms into the cycling transition and to keep the MOT from becoming depleted,

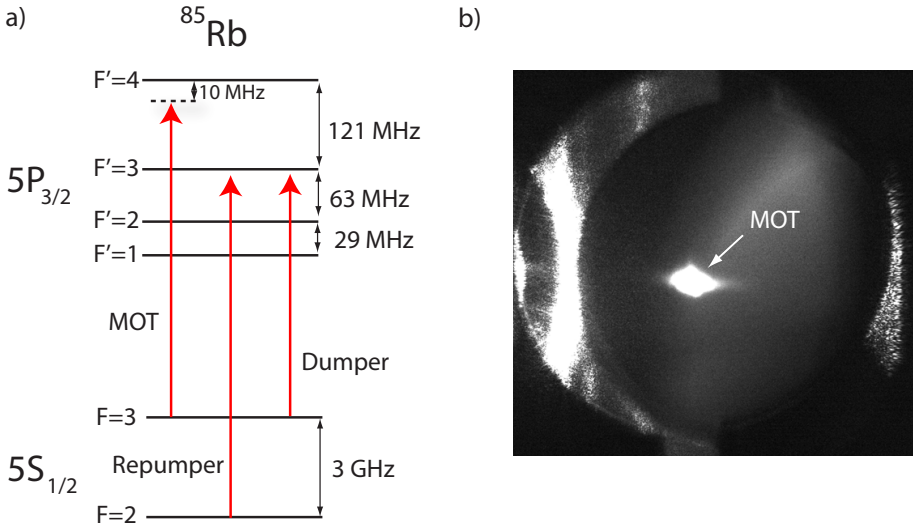

Figure 2.2: a) Hyperfine structure of the $5S_{1/2}$ and $5P_{3/2}$ levels of ^{85}Rb. Experimentally-relevant transitions are indicated by red arrows. b) A photograph of the magneto-optical trap in the experiments of this thesis.

we add another laser beam that is resonant with the $5S_{1/2}, F = 2 \rightarrow 5P_{3/2}, F' = 3$ transition, called the Repumper. The MOT will essentially not work without this Repumper beam.

An image of a typical MOT used in the experiments of this thesis is shown in Figure 2.2(b). The cloud of atoms in the MOT is visible since the atoms are scattering photons from the trapping light. In our experiments, atomic densities in the MOT are on the order of 10^9 atoms/cm^3. MOT sizes are about 1 mm in diameter and contain about 10^6 atoms. The temperature of the atoms is about 150 μK, which is the Doppler cooling limit for ^{85}Rb (a limit on the temperature that arises from a random walk induced by spontaneous emission). This temperature corresponds to atomic velocities of ≈ 10 cm/s.

2.1.2 Optical dipole traps and lattices

Aside from the MOT, another type of widely employed laser trap for ground-state atoms is an optical dipole trap. In this type of trap, atoms are confined in a focused

laser beam using the AC Stark effect, which is a shift in the atomic energy levels induced by an oscillating electric field (for example, a laser field). If the laser field is assumed to have an angular frequency ω and to be linearly polarized in the z-direction, the electric field is expressed in the electric dipole approximation as $\mathbf{E} = \hat{\mathbf{z}} E_0 \cos\omega t$. The Hamiltonian for an N-electron atom in the field is

$$H = \sum_{i=1}^{N} \frac{\mathbf{p}_i^2}{2m_\mathrm{e}} + V + eE_0 \sum_{i=1}^{N} z_i \cos\omega t.$$

To obtain the eigenenergies and eigenstates of the atom in the field, one must apply perturbation theory. The result for first order vanishes, since the time average of $\cos(\omega t)$ over one period vanishes. In second order, the resulting shifts to the energy levels in the atom are given by [45]

$$\Delta W_n^{(2)} = -\frac{e^2 E_0^2}{4} \left[\sum_{W_m + \hbar\omega \neq W_n} \frac{|\langle\psi_n|z|\psi_m\rangle|^2}{W_m - W_n + \hbar\omega} + \sum_{W_m - \hbar\omega \neq W_n} \frac{|\langle\psi_n|z|\psi_m\rangle|^2}{W_m - W_n - \hbar\omega} \right]. \quad (2.1)$$

Here, ψ_m and ψ_n are the unperturbed eigenfunctions, and W_m and W_n are the unperturbed eigenenergies [$(W_m - W_n)/\hbar = \omega_0$, the angular frequency of an atomic resonance]. When using Equation 2.1 to determine shifts to an atomic energy level induced by an optical field, the couplings of the level to all other levels are summed. For the ground state or for low-lying excited states, the strongest couplings are to nearby bound states. The $5S$ ground state of Rb, for example, only couples significantly to the first excited states, $5P_{1/2}$ and $5P_{3/2}$, in near infrared fields (such as those used in this thesis). The origin of the energy level shifts for ground or low-lying excited states is therefore distinct from that for Rydberg states, since Rydberg levels do not couple significantly to other bound levels for laser wavelengths in the near infrared.

The energy shifts of Equation 2.1 are dependent on the frequency ω of the field and

can be expressed in terms of a frequency-dependent polarizability. The frequency-dependent polarizability $\alpha(\omega)$ describes the tendency of the atom's electronic probability distribution to be distorted by the field and is given by

$$\alpha(\omega) = e^2 \left[\sum_{W_m + \hbar\omega \neq W_n} \frac{|\langle \psi_n | z | \psi_m \rangle|^2}{W_m - W_n + \hbar\omega} + \sum_{W_m - \hbar\omega \neq W_n} \frac{|\langle \psi_n | z | \psi_m \rangle|^2}{W_m - W_n - \hbar\omega} \right]. \qquad (2.2)$$

Using the frequency-dependent polarizability defined above, the AC Stark shift to the atomic energy levels is $\Delta W = -\frac{1}{4}\alpha(\omega)E_0^2$. This shift of the atomic energy levels in a laser field is commonly called a light shift. For the "red-detuned" case when $\omega < \omega_0$, $\alpha(\omega)$ is positive. For the "blue-detuned" case when $\omega > \omega_0$, $\alpha(\omega)$ is negative. The shift of the energy levels in the field (i.e. whether they are raised or depressed in energy) is therefore determined by the frequency of the field with respect to the atomic resonance structure. For a plot of the polarizability of the Rb ground state as a function of ω, see Reference [59].

Variations in the intensity profile of a laser field results in gradients in the AC Stark shifts of the atomic energy levels. These gradients result in a force on the atoms called the optical dipole force, which can be used to confine atoms in traps known as optical dipole traps [57]. The atoms are attracted to the intensity maximum of the beam profile if the frequency of the laser field is red-detuned with respect to the atomic resonance, or to the intensity minimum if the frequency of the field is blue-detuned. Optical dipole traps usually use large laser intensities, I, as well as large detunings, $\delta = \omega - \omega_0$. This parameter space is desirable since the scattering rate scales as I/δ^2, while the optical dipole potential scales as I/δ [60]. Large frequencies and detunings therefore allow for workable trap depths while minimizing heating of the atoms due to scattering of photons from the trapping light.

Typical red-detuned dipole traps for ground-state atoms are formed by focusing

a moderately high-power laser beam with Gaussian intensity profile into the atomic cloud of a MOT. Typical powers of the dipole-trap beam are ~ 1 W with beam foci in the range of tens of μm. The force from the optical dipole potential is conservative. Therefore, in order for any atoms initially in the MOT to be trapped in the optical dipole potential well, they must experience another force that dissipates their kinetic energy as they fall into the well. This dissipative force can result from scattering of MOT light, for example. An alternative method for loading atoms into a dipole trap involves carefully placing the atoms at the bottom of the dipole potential well, for example by adiabatically increasing the intensity of the dipole-trapping beam. In the trapping-beam intensity profile, the atoms are more tightly confined in the radial direction than along the axis of the beam, since the gradient in the intensity is weaker in the axial direction. This leads the atom cloud in the optical dipole trap to be "cigar-shaped." Typical atomic densities in red-detuned optical dipole traps are on the order of 10^{10} atoms/cm^3.

In order to realize a blue-detuned optical dipole trap, the laser beam profile must consist of a three-dimensional intensity minimum. This can be achieved by a number of methods, examples of which include focusing a Laguerre-Gaussian beam, focusing four parallel Gaussian beams arranged in a square pattern, or interfering two Gaussian beams of different focal spot sizes [30]. A benefit of blue-detuned dipole traps is that there is less heating of the atoms due to scattering of photons in the trapping light since the atoms are trapped at intensity minima; however, loading the atoms into the trap is less straightforward and typically results in lower atomic densities in the trap [61].

In an optical lattice, the intensity profile is formed by two (or more) pairs of counter-propagating laser beams that are often red-detuned and of Gaussian profile. The electric field of the counter-propagating laser beams has the form $\mathbf{E}(z,t) = \hat{\mathbf{x}}E_0[\cos(\omega t + kz) + \cos(\omega t - kz)]$, where E_0 is the single-beam electric field amplitude.

The resulting interference intensity pattern is

$$I(z) = \frac{1}{2} c\epsilon_0 \langle |\mathbf{E}(z,t)|^2 \rangle_T = c\epsilon_0 E_0^2 \cos^2(kz).$$

The intensity pattern has a periodicity of $\lambda/2$, which is typically on the size scale of a few hundred nm. Intensity gradients are therefore quite large in an optical lattice, as the intensity changes from a maximum to basically zero within a few hundred nm. This results in strong confining forces for atoms in an optical lattice.

The optical lattice utilized in this thesis is formed by two counter-propagating laser beams of wavelength 1064 nm. This wavelength is red-detuned with respect to the $5S \rightarrow 5P_{\mathrm{j}}$ transitions of Rb, and therefore the ground-state atoms are attracted to intensity maxima in the lattice. More experimental details about the optical lattice and its alignment are given below in Section 2.3.

2.2 Experimental sequence

Here, I give a brief overview of the experimental sequence used throughout this thesis, and further experimental details are given in the sections that follow. In the experiments, ^{85}Rb atoms are first cooled and trapped in a MOT inside a vacuum chamber with a pressure of about 10^{-9} Torr. The chamber is a cryogenic chamber, and the experiments are performed at 77 K. The atoms in the MOT are loaded into the optical lattice (of laser wavelength 1064 nm) by overlapping the lattice with the MOT. The sequence of events that constitute an experimental cycle are illustrated in Figure 2.3(a) and are repeated at a 200 Hz repetition rate. First in the cycle, the MOT and Repumper light is switched off. An optional sample clean-up pulse, which we refer to as the "Dumper" and which is discussed in more detail in Section 2.3.2, is applied to eliminate untrapped ground-state atoms. The remaining atoms in the lattice are then excited to Rydberg states via two-photon excitation from the $5S$

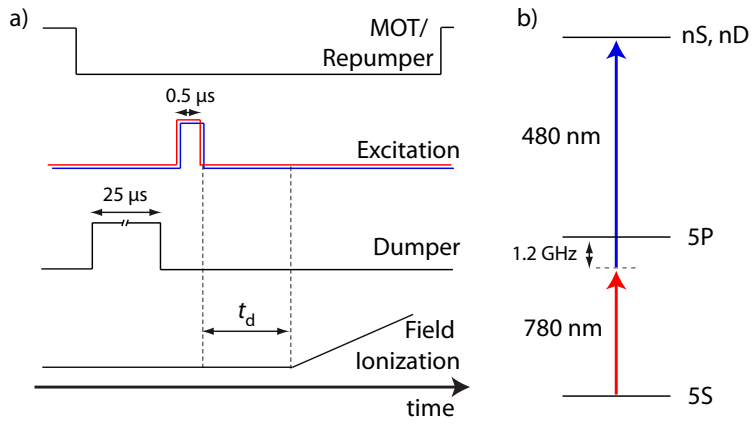

Figure 2.3: a) Timing diagram of the events involved in one experimental cycle. After excitation to Rydberg states, the electric field ionization ramp used for Rydberg detection is applied at a variable time delay, t_d. b) Scheme for excitation from the ground state to Rydberg states.

ground state to nS or nD Rydberg states, as described in Section 2.2.1. The Rydberg atoms are detected after a delay time t_d by ionizing them with a pulsed electric field and subsequently detecting the ionized electrons, a method discussed in Section 2.2.2.

2.2.1 Rydberg excitation

Ground-state atoms are transferred to Rydberg states via two-photon excitation $5S_{1/2} \rightarrow 5P_{3/2} \rightarrow$ Rydberg, as illustrated in Figure 2.3(b). The laser light for the $5S-5P$ transition has a wavelength of 780 nm and is ≈ 1.2 GHz detuned from the $5P_{3/2}$ intermediate state. The laser light for the $5P-$Rydberg transition has a wavelength of ≈ 480 nm and is tuned to achieve two-photon resonance with a $5S \rightarrow$ Rydberg nS or nD transition (which are the two choices allowed by selection rules). By performing the two-photon transition off-resonance with the $5P$ intermediate state, we achieve a more coherent transition (since spontaneous emission from $5P$ is avoided) and narrower Rydberg excitation lines.

The arrangement of the excitation laser beams in the experimental setup is illustrated in Figure 2.4. The $5S-5P$ beam is co-propagating with the lattice beams; it is therefore focused by the same lens that focuses the ingoing lattice beam (for details

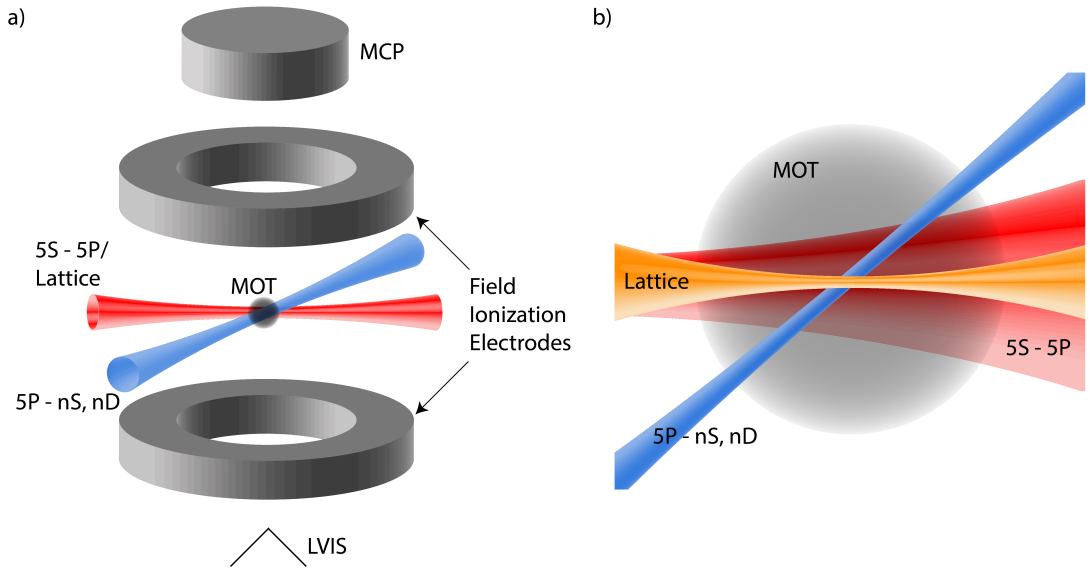

Figure 2.4: a) Qualitative illustration of the laser beam and detection apparatus geometry utilized in the experimental setup. The $5S - 5P$ excitation beam and the lattice beam are co-propagating. After Rydberg atoms are excited, they are detected using electric field ionization and a microchannel plate (MCP). b) Close-up view of the overlap of the excitation and lattice laser beams at the MOT.

about the lattice setup, see Section 2.3). Due to chromatic aberrations, the focus of the $5S - 5P$ beam lies about 2 mm away from the lattice focus. The FWHM of the $5S - 5P$ beam at the location of the atoms is 150 μm. The $5S -$ Rydberg excitation beam forms an angle of about 45° with the $5S - 5P$ and lattice beams and is focused to a FWHM of $\approx$ 15 μm. This focal size of the $5S -$ Rydberg beam is chosen to approximately match the lattice focus.

The excitation light is pulsed during the experiment, with typical pulse durations of $\tau_{\text{ex}} = 0.5$ μs. The powers of the excitation pulses are set such that the number of Rydberg atoms excited per cycle is about one, so that Rydberg-atom interactions and collisions do not play an important role in the experimental results. In a typical experiment, I use 30 μW and 30 mW of $5S - 5P$ and $5P -$ Rydberg laser power, respectively. Using the beam powers, beam profiles, intermediate state detuning, and $5P -$ Rydberg transition matrix elements, two-photon Rabi frequencies are estimated to be up to $2\pi \times 500$ kHz. With the lattice off, the observed FWHM of the Rydberg

excitation lines are between 2-3 MHz, which is just slightly above the width of the power spectrum of a square pulse with 0.5 μs duration. Hence, for my excitation pulse duration, transition broadening due to saturation plays no significant role. The slight broadening of the lattice-free Rydberg excitation lines is attributed to electric field inhomogeneities and the MOT magnetic field[1].

As for the hardware used for excitation light production and control, the source of the $5S - 5P$ laser light is a homebuilt external cavity diode laser (ECDL). The wavelength of the ECDL ($\approx$ 780 nm) is stabilized by feedback on the diode current and the diffraction grating in order to lock to a saturated absorption spectroscopy resonance (for an explanation of ECDLs see [62], for saturated absorption spectroscopy see [60]). Stabilization of the wavelength off-resonance with the $5P_{3/2}$ intermediate state is achieved by locking the ECDL to the $5S_{1/2}, F = 2 \rightarrow 5P_{3/2}, F' = 3$ transition of ^{87}Rb, which is $\approx$ 1.2 GHz red-detuned from the $5S_{1/2}, F = 3 \rightarrow 5P_{3/2}, F' = 4$ transition of ^{85}Rb.

The source of the laser light for the $5P -$ Rydberg transition is a Topica SHG laser system, which outputs $\approx$ 200 mW of 480 nm light. In this laser system, the output beam of a 960 nm diode laser is first amplified and then frequency-doubled to 480 nm. The frequency doubling is achieved by second harmonic generation using a nonlinear crystal (a process first demonstrated by P. Franken and co-workers at the University of Michigan [63]), which is located inside a cavity arranged in a bow-tie configuration. The wavelength of the $5P -$ Rydberg laser is stabilized by providing feedback on the 960 nm diode laser current to lock to a transmission peak from a pressure-tuned Fabry-Pérot cavity. The Fabry-Pérot cavity was designed and built by the Raithel lab [64]. It consists of two mirrors in a chamber with an attached bellows. A stepper motor connected to a translation stage compresses or expands the bellows, changing the pressure and consequently also the index of refraction in the cavity.

[1]The MOT magnetic field is not switchable in the experimental setup because of eddy currents in the system that persist for $\approx$ 50 ms.

The change in index of refraction shifts the frequency of the transmission peak, thus tuning the frequency of the laser. The typical drift rate of the transmission peaks from the Fabry-Pérot cavity is $\sim$ 350 kHz per minute. Therefore, when performing experiments with the $5P-$Rydberg laser frequency set to a particular value, data can be taken for about five minutes before the laser frequency needs to be checked. The full scan range of the Fabry-Pérot is $\sim$ 1 GHz, which is about equal to the spacing between adjacent Rydberg states.

The excitation light pulses are created by passing the laser beams through acousto-optic modulators (AOMs) and pulsing the rf power applied to the AOMs. The first-order light from the AOMs is coupled into the optical fiber that transmits the light to the experimental chamber. Pulsing the rf power essentially turns the first-order light on and off, thus creating light pulses at the fiber output.

2.2.2 Rydberg detection

Since Rydberg electrons are so loosely bound to the atomic core, they are ionized by a modest DC electric field. Rydberg atoms are therefore readily detected by pulsing an electric field and detecting the ionized electrons. In the experiments presented in this thesis, I use state-selective electric field ionization as the Rydberg-atom detection method. In this method, an electric field is increased as a function of time from zero to values above the Rydberg-atom ionization limit. The electric field values at which the ionized electrons are detected determine the spectrum of states present.

To understand the state-selective electric field ionization method, one must consider the Stark shift of the atomic energy levels in a DC electric field. These shifts are illustrated for Rb in Figure 2.5. As the electric field is increased, adjacent states that are initially non-degenerate eventually (anti-)cross, a point referred to as the Ingles-Teller limit ($\approx$ 6 V/cm in Figure 2.5). For higher electric field values (and also for non-hydrogenic atoms), low-ℓ states of different n undergo avoided crossings,

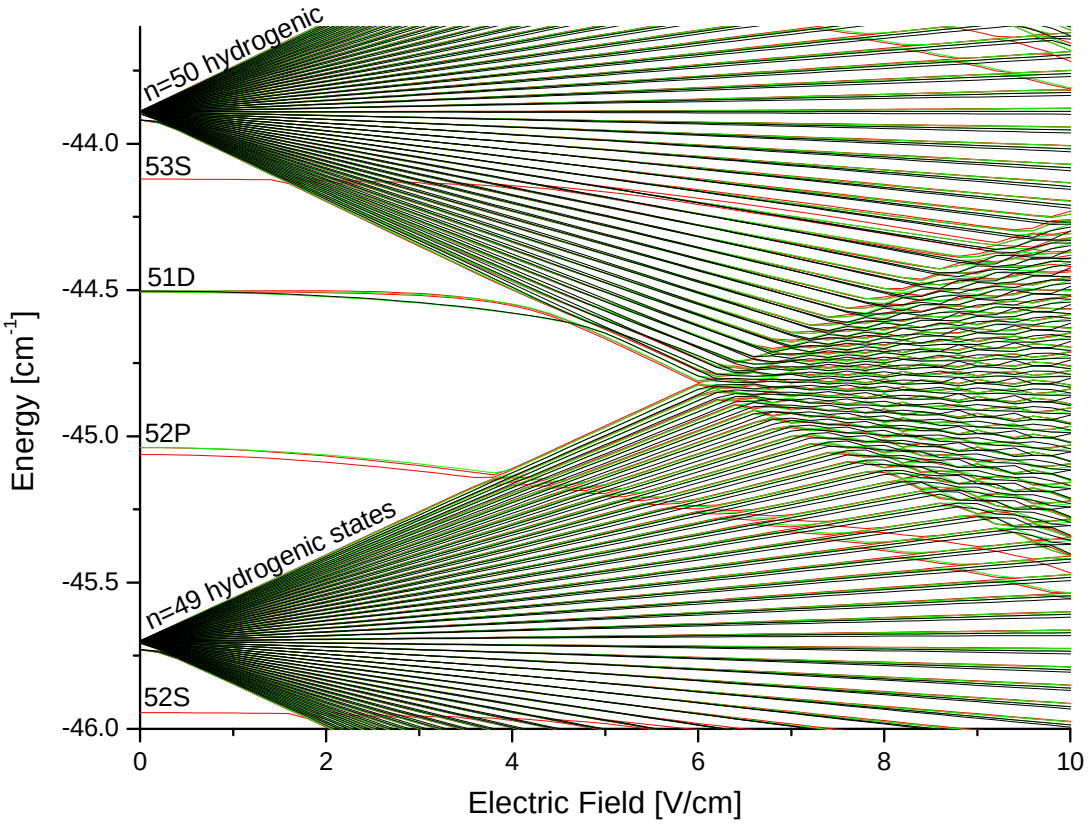

Figure 2.5: Calculated Stark map of Rb energy levels as a function of DC electric field. Red: $m_j = 1/2$. Green: $m_j = 3/2$. Black: $m_j = 5/2$.

due to the large, non-zero quantum defects (see Gallagher, Reference [26]). In Rb, the quantum defects are large for S, P, and D states, since the radial wavefunctions penetrate into the finite-sized ionic core (see Section 1.2.2). The ionization process for these states therefore depends on how quickly the electric field increases with time from zero field to the ionization field (i.e. the slew rate, $S = dE/dt$). If the slew rate is sufficiently slow and the avoided crossings sufficiently large, the states will traverse the Stark map from zero field to the ionization field adiabatically. An adiabatic ionization process preserves the zero-field ordering of the energy levels and allows for unambiguous determination of the initial, zero-field n states from the electric field at which they ionize. The ionization electric field for low-ℓ states is $E = 1/16n^{*4}$ in atomic units, as determined in Section 1.2.

For high-ℓ states, the avoided level crossings are smaller, due to the near-zero quantum defects. For the same electric field slew rate as in the low-ℓ case, the high-ℓ states will traverse the Stark map diabatically and ionize at higher electric fields. The ionization electric fields for high-ℓ states are between $E = 1/9n^{*4}$ and $E = 1/4n^{*4}$ [26]. A diabatic ionization process does not allow for a straightforward determination of initial n states from the electric field values at which the states ionize, since the zero-field ordering of the states may not be preserved.

In this thesis, I am only concerned with the low-ℓ Rydberg states nS or nD, which fortunately undergo adiabatic ionization. In the experimental setup, the ionization electric field is created by ramping the electrode on the LVIS side of the chamber [see Figure 2.4(a)] from 0 to -350 V (corresponding to peak electric fields of ~ 130 V/cm) with a rise-time of ≈ 10 μs. After the Rydberg atoms are ionized, the freed electrons are pushed by the electric field to a microchannel plate (MCP) assembly for detection. The MCP is composed of an array of lead glass capillaries with diameter ≈ 10 μm and spacing of ≈ 15 μm. The capillaries are oriented at an angle of $\approx 8^\circ$ with the normal to the face of the MCP [65]. A freed electron strikes the wall of one of the capillaries

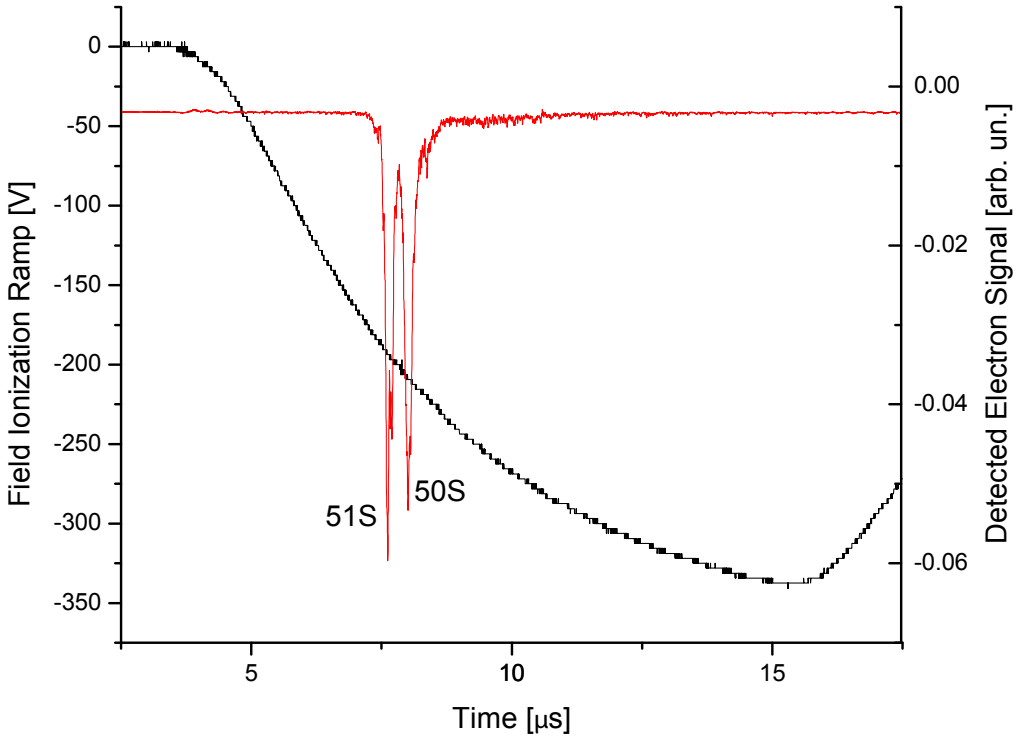

Figure 2.6: Experimental state-selective field ionization trace. The voltage applied to the field ionization electrode is indicated in black, and the corresponding detected electron signal is indicated in red. The $50S$ and $51S$ states are ionized at slightly different electric field values. The $51S$ state, being more loosely bound to the atom, is ionized by a smaller field.

and creates a shower of secondary electrons which are further accelerated by the voltages applied across the MCP. In my work, I use two MCPs in series, which yield a charge gain of about 10^6. Behind the MCP, a phosphor screen converts the shower of electron impacts to light, which may be used to obtain spatial information about the distribution of electrons hitting the face of the MCP [10]. The electrical signal, which yields temporal information about the detected electrons, is capacitively coupled out of the phosphor screen and directed to a counter. The counter communicates with the computer for recording the electron detections. The temporal information about the ionized electrons is correlated with the electric field values at which they are detected and is thereby used to determine the spectrum of Rydberg states present. The MCP has a $\approx 30\%$ detection efficiency.

Figure 2.6 illustrates the electric field ionization ramp (black) utilized in the experiments of this thesis and the detected electron signal corresponding to the states $50S$ and $51S$ (red). Since the $51S$ state is more loosely bound to the atom than the $50S$ state, it ionizes at a slightly lower electric field value. The signal from the two states is resolved, as between the $50S$ and $51S$ peaks, the signal almost dips to the background value. While there is a slight overlap of the $50S$ and $51S$ signals, I estimate this crosstalk to be less than 5%. The ability to resolve these two states is an important prerequisite for the experiments presented in Chapter III.

2.3 The optical lattice

2.3.1 Alignment of the lattice

The laser used for the optical lattice is a 1064 nm ytterbium fiber laser, with an output power ≤ 10 W. The one-dimensional optical lattice is established by focusing the 1064 nm beam into the MOT, retroreflecting it with a corner cube retroreflector, and refocusing it. The corner cube retroreflector is composed of three intersecting

planar mirrors that are mutually orthogonal. Since the corner cube always reflects the beam back parallel to its incoming path, the corner cube plays a crucial role in the stability of the lattice alignment. We have confirmed that the retroreflector preserves the polarization of the lattice light. The ingoing lattice beam is focused to a FWHM of 13 μm, and in typical experiments, the power in the ingoing beam is ≈ 1 W. The return beam has a FWHM of ≈ 25 μm (see Section 3.3 and Reference [66]), which is larger than the ingoing beam focus due to cumulative aberrations caused by the optical components in the retroreflection beam path. Also, the optical components in the beam path reduce the power of the return lattice beam at the location of the atoms to 0.56 times that of the ingoing beam. The lattice is therefore not a perfect standing wave, due to the mismatch in intensities of the ingoing and return lattice beams. However, the contrast in the lattice is still about a factor of 5. Peak intensities in the lattice are on the order of 10^6 W/cm^2. The lattice is linearly polarized and is always on for measurements involving the optical lattice.

In the first step of aligning the lattice, the return beam is blocked, and the ingoing beam establishes a running-wave dipole trap for ground-state atoms in the MOT. The focus of the ingoing beam is positioned to maximize dipole-trap-induced light shifts of the optical ground-to-Rydberg transition frequency. An example of an optical excitation spectrum of the $50S$ Rydberg level in the dipole trap is shown in Figure 2.7(a) (black). The spectrum is obtained by scanning the frequency of the $5P-$ Rydberg excitation laser and plotting the number of detected Rydberg atoms as a function of frequency. The peak in the spectrum at 0 MHz is due to atoms that are excited in the MOT outside of the dipole trap [i.e. in the regions where the excitation beams overlap outside of the 1064 nm beam, see Figure 2.4(b)]. This peak therefore corresponds to the unperturbed ground-to-Rydberg transition frequency, as indicated by the solid arrows in Figure 2.7(a),(b). The blue-shifted feature in the excitation spectrum of Figure 2.7(a) is from atoms located in the dipole trap that

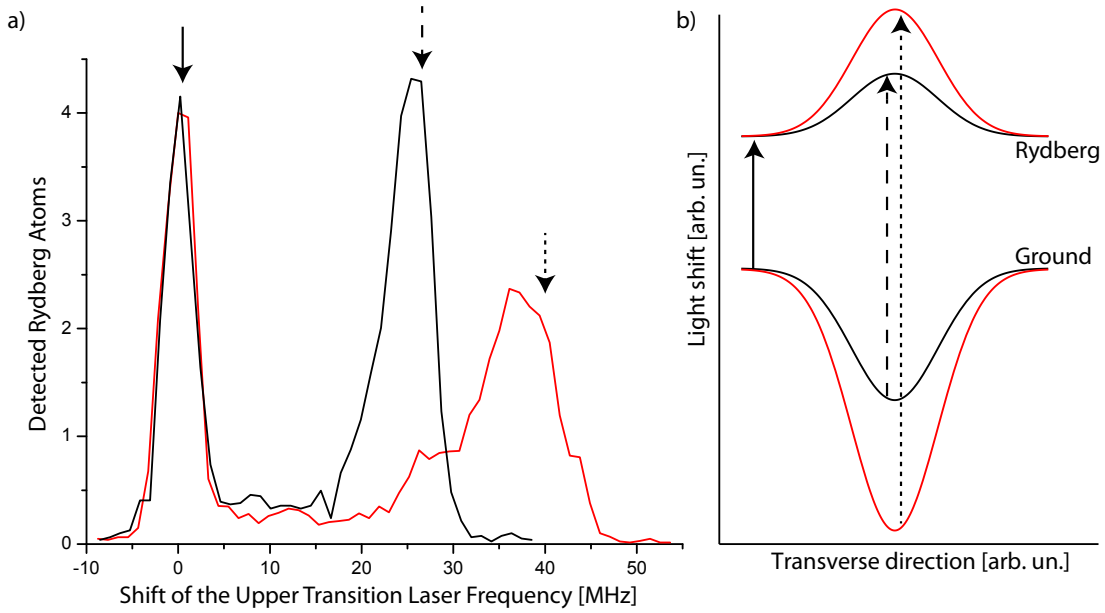

Figure 2.7: a) Optical excitation spectra for $50S$ in the running-wave dipole trap (black) and standing-wave optical lattice (red), obtained by scanning the frequency of the upper transition excitation laser and plotting the number of detected Rydberg atoms. On the x-axis, 0 MHz corresponds to the unshifted transition frequency $5S_{1/2} \rightarrow 50S_{1/2}$. The arrows correspond to the ground-to-Rydberg transition frequency at the locations indicated in (b). b) Qualitative illustration of the light shift of the ground and Rydberg potentials in the dipole trap (black) and the lattice (red), for a cut transverse to the lattice axis. The solid arrow corresponds to the unperturbed ground-to-Rydberg transition frequency. The dashed and dotted arrows correspond to the transition frequencies for atoms located near the bottoms of the dipole-trap and optical-lattice potential wells, respectively.

experience dipole-trap-induced light shifts [dashed arrows in Figure 2.7(a),(b)]. To optimize the dipole trap alignment, both the position of the ingoing beam focus and the overlap of the $5P-$ Rydberg excitation beam with the 1064 nm focal spot are optimized for maximal shift and sharpest cutoff on the blue-frequency side of the excitation spectrum in Figure 2.7(a). The maximal shift and sharp cutoff means that the focus of the dipole trap beam is overlapped with the center of the MOT and that I am exciting atoms located near the bottom of the ground-state potential wells.

To align the return beam of the lattice, the return-beam focus is positioned to optimize the back-coupling through the optical fiber (that transmits the 1064 nm light to the experimental chamber; see Figure 3.2). Since I couple the 1064 nm light out and back into the same fiber (which is a single mode fiber), I ensure that the incident and return foci overlap. An optical excitation spectrum for the standing-wave optical lattice is shown in Figure 2.7(a) (red). The shift of the blue-frequency cutoff from the unperturbed transition frequency in the lattice spectrum is about two times that for the dipole trap, due to the increased light intensity in the lattice [see light shifts and dotted arrow in Figure 2.7(b)]. In a lattice with perfect visibility, the lattice-induced shift would be four times the dipole-trap-induced shift. The reduction in the experimentally observed lattice-induced shift is due to the imperfect visibility in the lattice, which results from the reduction in power and enlargement in focus of the return beam discussed above. In the lattice spectrum of Figure 2.7(a), the sharp cutoff on the blue-frequency side of the spectrum indicates that the ground-state atoms in the lattice are localized near the bottoms of the lattice potential wells. They are therefore efficiently cooled by the MOT light, which is effectively increased in red-detuning as the atoms in the lattice experience lattice-induced light shifts [67, 68].

Optical excitation spectra for $50S$ in the lattice as a function of lattice laser power is shown in Figure 2.8 (indicated powers are for the ingoing lattice beam). For powers $\lesssim 1$ W, the blue-shifted feature due to atoms in the lattice is well-localized on the

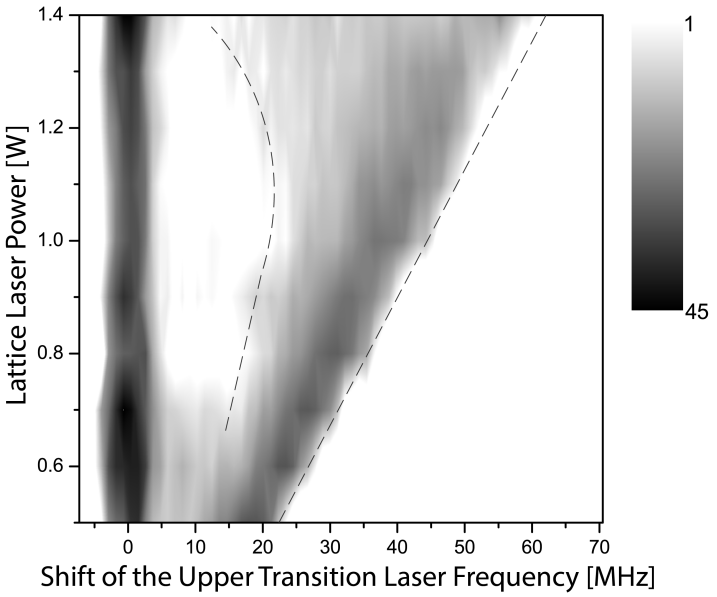

Figure 2.8: Optical excitation spectra for $50S$ in the lattice as a function of lattice power (indicated values are for the ingoing beam), plotted on a logarithmic scale to emphasize detail in low count regions. The spectra demonstrate that for powers higher than about 1 W the ground-state atoms are cooled less efficiently to the bottoms of the lattice potential wells.

high-frequency side, and the frequency shift scales linearly with lattice power. For powers $\gtrsim 1$ W, the blue-shifted feature spreads out, indicating that the atoms are not as well localized near the bottoms of the ground-state lattice wells. This indicates a deterioration in the laser cooling of the atoms in the deeper lattice wells, as the detuning of the MOT light approaches 60 MHz at the highest powers. The MOT light is then too far detuned to efficiently cool the atoms in the lattice. Due to this deterioration of the laser cooling at high lattice powers, I limit the lattice ingoing beam power to ≈ 1 W for the experiments presented in this thesis. Since the temperature of the ground-state atoms in the lattice largely determines the temperature of the atoms after they are excited to Rydberg states, it is beneficial to cool the ground-state atoms as efficiently as possible to enable high Rydberg-atom trapping efficiencies in the lattice (see Section 3.4).

The maximal lattice-induced shifts in optical excitation spectra, as shown in Fig-

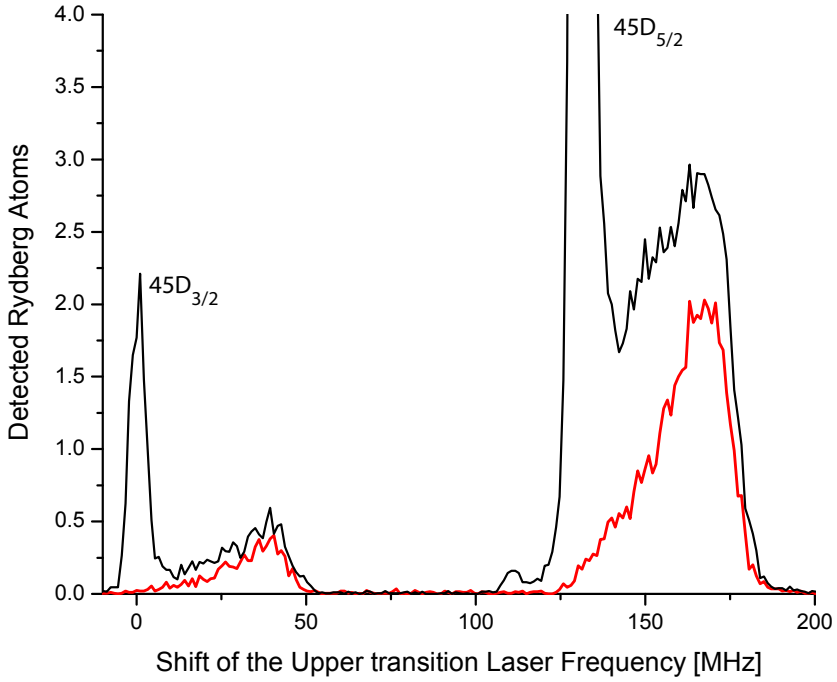

Figure 2.9: Effect of the Dumper pulse. Optical excitation spectra for $45D$ in the lattice, with (red) and without (black) the Dumper.

ure 2.7, yield information on the lattice potential modulation depths for both the ground state and the Rydberg state; this is discussed in detail in Section 4.2.2. Lattice-induced shifts in optical excitation spectra are therefore used daily for verifying alignment of the optical lattice. The Rydberg potential modulation depth varies for different Rydberg states, both in magnitude and sign. As a reference point, the lattice modulation depth for $50S$ and 1 W of ingoing lattice beam power is ≈ 10 MHz. The modulation depth of the ground-state lattice potential for 1 W of ingoing lattice beam power is ≈ 20 MHz.

2.3.2 Signal improvement using optical pumping techniques

As illustrated in the excitation spectra of Figures 2.7 and 2.8, a significant number of atoms are excited outside of the lattice (evidenced in the peak at 0 MHz). This signal is undesirable for my experiments, as it may overwhelm signal from the atoms in the lattice. To reduce or eliminate the signal from atoms outside of the lattice,

I apply a sample clean-up pulse, referred to as the "Dumper" pulse, between the turnoff of the MOT/Repumper light and the application of the excitation pulses [see Figure 2.3(a)]. The Dumper pulse has a duration of 25 μs and is resonant with the $5S_{1/2}$, F=3 $\rightarrow$ $5P_{3/2}$, F'=3 transition (see Figure 2.2). Due to light shifts for atoms in the lattice, the Dumper is closer to resonance with the atoms outside of the lattice. The Dumper therefore optically pumps the atoms outside of the lattice into the F=2 ground state much more efficiently than the atoms inside the lattice. Since the Repumper light is off, these atoms do not return to the cycling transition. Following the Dumper pulse, the F=3 atoms left in the lattice are accessible for optical excitation to the Rydberg state. Figure 2.9 shows optical excitation spectra for $45D$ with (red) and without (black) the Dumper pulse applied. With the Dumper, the signal at relative frequencies of 0 MHz and 130 MHz from atoms outside of the lattice disappears, leaving only the signal from the atoms in the lattice. The Dumper is therefore an effective method to obtain a clean sample of atoms in the lattice for use in experiments.

In the following chapters of this thesis, the experimental setup and procedures described in this chapter are employed to study Rydberg atoms in optical lattices. The trapping of Rydberg atoms in optical fields was first proposed in 2000 [40] and first achieved in 2010 [41]. Now, optical Rydberg-atom traps are anticipated to become a mainstream technique for quantum information processing [4, 30, 59], high-precision spectroscopy [31], or many-body physics [11]. In the next chapter, I discuss work that led to the first highly efficient optical trap for Rydberg atoms, a development that moves this system a significant step closer to being available for use in applications [66].

CHAPTER III

Lattice Inversion for Highly Efficient Rydberg-atom Trapping

Rydberg-atom trapping has emerged as a tool in such applications as quantum computing [2, 4, 32, 69] and high-precision spectroscopy [31], as described in Section 1.3. Small lattice-induced energy-level shifts distinguish optical Rydberg-atom traps from static-field traps [36, 37] and make them attractive for these applications. While optical traps for Rydberg atoms were first proposed by the Raithel group [40], several groups are now pursuing traps along these lines [30, 70], largely motivated by the possibility to create "magic wavelength" traps that minimize trap-induced shifts on transitions of interest in quantum computing or high-precision spectroscopy [33]. Despite potential applications, efficient optical traps for Rydberg atoms had not been realized until the work described in this chapter. In this work, I demonstrate an optical lattice with high Rydberg-atom trapping efficiency.

3.1 Rydberg-atom preparation in the lattice

To understand the technique for achieving high trapping efficiencies developed in this chapter, one must first consider the preparation process for the Rydberg atoms in the 1064 nm optical lattice. Ground-state ^{85}Rb atoms are initially laser-cooled

into the wells of the $5S$ lattice potential and are then laser excited to Rydberg states (see Section 2.2.1). As discussed in Section 1.3.2, the Rydberg electron experiences a ponderomotive potential in the optical lattice much like that a free electron experiences, $V_\mathrm{p} = e^2 E_0^2/(4m_\mathrm{e}\omega^2)$, where ω is the angular frequency of the field and E_0 is the amplitude of the linearly polarized field at the location of the Rydberg electron. The polarizability of the Rydberg state is therefore approximately that of a free electron. The free-electron polarizability, α_p, is found by comparing V_p to the expression for the AC Stark shift, $W = -\frac{1}{4}\alpha E_0^2$. Thus, $\alpha_\mathrm{p} = -e^2/(m_\mathrm{e}\omega^2)$. In a 1064 nm laser field, $\alpha_\mathrm{p} = -4\pi\epsilon_0 \times 545 a_0^3$ in SI units. To find the polarizability α_R of a specific Rydberg state in the optical lattice, one must multiply α_p by a state-dependent factor, ξ_R, that takes into account the averaging of the Rydberg-atom wavefunction over the free-electron ponderomotive potential (see Equation 1.6). In general, the ξ_R depend on the geometry of the lattice; here, I consider my case of two counter-propagating laser beams of the same linear polarization. For the $50S$ state in my lattice, a case under consideration in this chapter, the averaging factor is $\xi_{50S} = 0.415$. The polarizability of the $50S$ state in the optical lattice is therefore $\alpha_{50S} = -4\pi\epsilon_0 \times 0.415 \times 545 a_0^3$ in SI units. For the $50S$ state and most Rydberg states, the polarizability is negative[1], and the Rydberg atoms are attracted to regions of intensity minimum in the lattice.

In contrast to the Rydberg states, atoms in the ^{85}Rb $5S$ ground state have a positive dynamic polarizability at 1064 nm, since this wavelength is red-detuned relative to the $5S \rightarrow 5P$ transition (see Section 2.1.2). The polarizability of the $5S$ ground state is $\alpha_\mathrm{5S} = 4\pi\epsilon_0 \times 711 a_0^3$ in SI units at 1064 nm [71], and the ground-state atoms are attracted to regions of intensity maximum in the lattice.

Due to the (usually) different signs of α_R and α_5S for the 1064 nm optical lattice, the ground-state lattice potential minima, which are co-located with light inten-

[1] An exception occurs when the size of the Rydberg atom approximately equals the lattice period. In this case, ξ_R becomes negative, resulting in a positive polarizability α_R. Such a case is measured and discussed in Section 4.2.2.

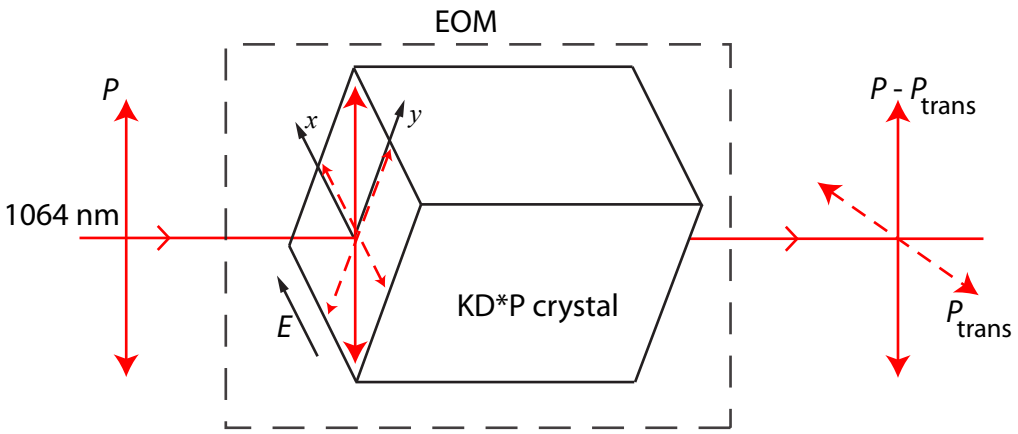

Figure 3.1: Configuration for an electro-optic modulator (EOM) used as a polarization switch. In a simplified picture, the EOM contains a KD*P crystal with index of refraction along x that changes in response to an electric field, E. The change in index of refraction introduces a phase shift between the x- and y-polarization components, thus modifying the polarization state of the light at the output. The EOM splits the linearly-polarized input beam of power P into orthogonal output components with powers $P - P_{\text{trans}}$ and P_{trans}.

sity maxima, coincide with Rydberg-state potential maxima. Laser excitation of the ground-state atoms in the lattice produces Rydberg atoms near the maxima of the Rydberg-atom lattice potential. This results in limited Rydberg-atom trapping in the lattice. Previously, we have trapped a few percent of these atoms in the lattice [41]. The few trapped atoms were fortuitously excited partway down the Rydberg lattice wells, due to the linewidth of the excitation lasers, and did not have enough energy to escape the wells. In the work presented in this chapter, I develop a method to rapidly invert the lattice potential after Rydberg-atom preparation. Since the inverted potential has minima near the locations of the initially prepared Rydberg atoms, I achieve highly efficient optical Rydberg-atom trapping.

3.2 Lattice inversion

To invert the lattice, I use an electro-optic technique. This technique is enabled by an electro-optic modulator (EOM; Conoptics, Inc., model 350-105) used as a polariza-

tion switch. Here, I present a simplified explanation of how the EOM switches the polarization. The EOM contains a crystal (KD^*P) that exhibits the linear electro-optic effect. This effect is a modification in the index of refraction of the crystal in response to an applied electric field, by an amount proportional to the field strength [72]. I use the controllable index of refraction in the EOM to modify the polarization state of the lattice light passing through the device. The configuration for an EOM as a polarization switch in our setup is illustrated in Figure 3.1. The 1064 nm beam incident on the EOM is linearly polarized and has power P. The electric field in the EOM is applied to the crystal in the x-direction in Figure 3.1, which is transverse to the 1064 nm beam propagation direction and at a 45° angle to the incident 1064 nm polarization direction. Depending on the electric field strength, the 1064 nm polarization component in the x-direction may experience a different index of refraction than that in the y-direction. This difference in index of refraction introduces a phase shift between the x and y components that consequently modifies the polarization state of the light at the EOM output. In general, the total incident power P is split into two orthogonal linear-polarization components at the EOM output, with variable powers P_{trans} and $P - P_{\text{trans}}$ as indicated in Figure 3.1. When the electric field in the EOM is set such that the index of refraction in the x- and y-directions in Figure 3.1 is equal, the light passes through with its polarization state unaltered ($P_{\text{trans}} = 0$). When the electric field is set such that the relative phase shift between x and y components is π, the input linear polarization is rotated by 90° ($P_{\text{trans}} = P$).

In the experiment, the EOM switches the polarization state of the lattice light immediately after Rydberg-atom excitation. For a complete lattice inversion, the EOM switches the polarization from one linear direction ($P_{\text{trans}} = 0$) to the orthogonal linear direction ($P_{\text{trans}} = P$). The lattice light is then transmitted to the atoms using a polarization-maintaining (PM) fiber (see diagram of the experimental setup in Figure 3.2). The two orthogonal linear lattice polarization directions are aligned

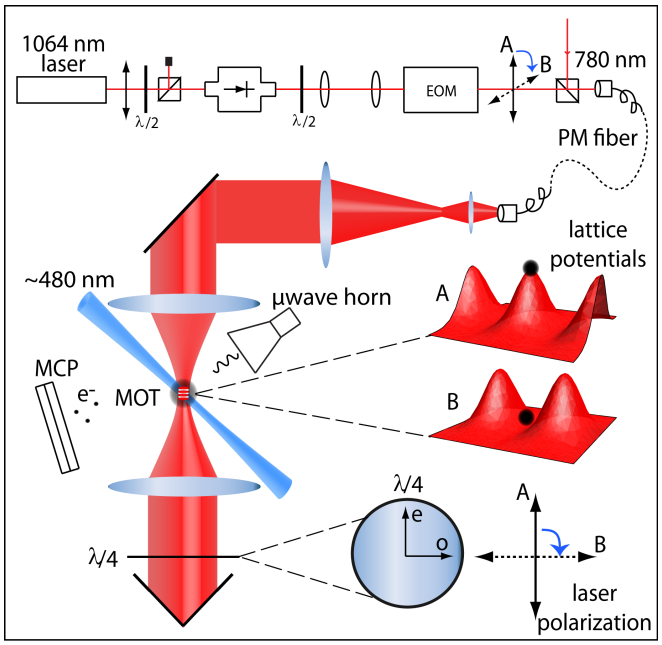

Figure 3.2: Sketch of the experimental setup. Rydberg atoms are optically excited at potential maxima of a one-dimensional Rydberg-atom optical lattice. An EOM is used to switch the lattice polarization by 90° from A to B immediately after excitation, resulting in lattice inversion and efficient Rydberg-atom trapping.

with the axes of a quarter waveplate in the return beam of the lattice that introduces a total differential phase shift of π between the polarization components. For a complete lattice inversion, a phase shift of π in the return beam alters the locations of intensity maxima and minima in the lattice by $\lambda/4$. Thus, a complete lattice inversion applied immediately after Rydberg-atom excitation results in intensity minima at the location of the excited atoms. For the lattice inversion to be most effective, the timescale over which the inversion occurs must be faster than the center-of-mass oscillation period of the atoms in the lattice. In the utilized lattice, the oscillation period is ~ 5 μs while 85% of the polarization switch occurs within 0.2 μs.

In general, I characterize the lattice inversion by the parameter $\eta = P_{\text{trans}}/P$, which ranges from zero (no inversion) to 1 (complete inversion). For η values between zero and 1, the polarization of the light at the output of the EOM is elliptical. The Rydberg-atom lattice potentials are insensitive to the polarization of the lattice

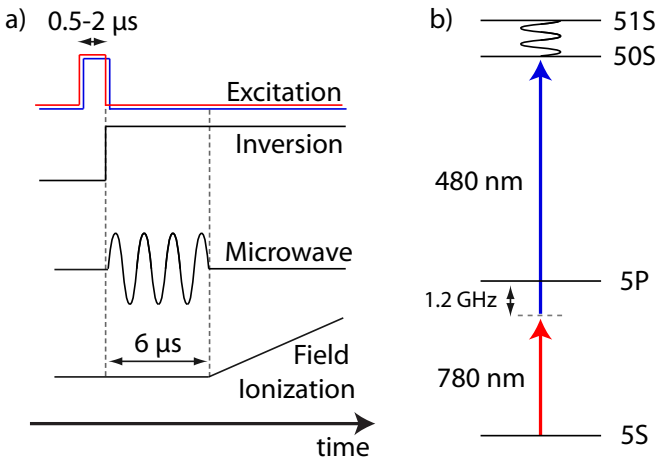

Figure 3.3: a) Experimental timing diagram for performing microwave spectroscopy on the atoms in the lattice. b) Level diagram illustrating the excitation scheme. After ground-state atoms are excited to the $50S$ Rydberg state, they are driven via a two-photon microwave transition to $51S$.

light (in contrast to ground-state atoms, which have polarization-dependent trapping potentials [54]) and depend only on the powers in the two orthogonal linear polarizations. Due to the waveplate in the return beam, one linear component acquires a phase of π that shifts the locations of intensity minima and maxima by $\lambda/4$ for that component. In the special case of circular polarization ($\eta = 0.5$), for example, the two components have equal powers, but the interference pattern for one of the components is shifted by $\lambda/4$. The corresponding lattice potentials in this case are flat. Lattice potentials for selected values of η are depicted in Figure 3.5(b).

3.3 Microwave spectroscopy

Demonstrating that the lattice inversion results in efficient Rydberg-atom trapping is not a straightforward task. Methods usually employed in demonstrating the trapping of ground-state atoms involve holding the trapped atoms while the untrapped atoms fall away under the influence of gravity. However, this method is not feasible for the $50S$ Rydberg state under consideration here, since its lifetime of ≈ 100 μs at

77 K is not long enough for the untrapped atoms to fall out of the detection region. Instead, I make use of the unique state-dependent potentials for Rydberg atoms in the lattice (see Section 1.3.2) to establish the presence of trapped atoms using microwave spectroscopy of the $50S \rightarrow 51S$ transition. S-states are well-suited for these experiments due to their insensitivity to residual electric and magnetic fields and their isotropic wavefunctions, which eliminate the orientational effects discussed in Section 4.1. These features of S-states allow for transform-limited microwave spectra. The experimental sequence for performing microwave spectroscopy is illustrated in Figure 3.3. Excitation laser pulses of duration τ_{ex} are applied, as described in Section 2.2.1, to prepare $50S$ atoms in the lattice. The frequency of the $5P \rightarrow$ Rydberg excitation laser is set to excite atoms at the deepest part of the lattice wells (see Figure 2.7). Immediately after the excitation laser pulses, the lattice potential is inverted. The Rydberg atoms then interact for 6 μs with microwave radiation that drives the $50S \rightarrow 51S$ two-photon transition (transitions proceed off-resonantly through an intermediate P state). Subsequently, the Rydberg-state distribution is measured using state-selective electric field ionization (see Section 2.2.2). The $50S$ and $51S$ states produce distinct ionization signals, shown in Figure 2.6, that are recorded separately with a gated pulse counter. The microwave power in the experiment is set such that the fraction of the population transferred to the $51S$ state on-resonance without the lattice is 50%.

The microwave spectroscopy method of investigating the lattice trapping efficiency exploits the fact that the lattice-induced shift of the microwave transition depends on the atomic position in the lattice. To illustrate, I first consider the case without a lattice inversion ($\eta = 0$). In this case, the atoms are initially located near lattice potential maxima following excitation to the $50S$ Rydberg state. The microwave spectrum for the $50S \rightarrow 51S$ transition in this case is shown in the lowermost spectrum in Figure 3.5(a). The x-axis in Figure 3.5(a) is scaled such that 0 corresponds to the

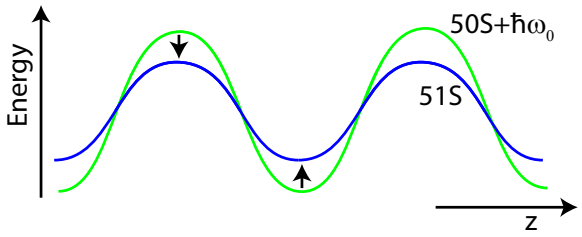

Figure 3.4: The $50S$ and $51S$ lattice potentials. The $50S$ potential is shown shifted up in energy by the unperturbed $50S \rightarrow 51S$ transition energy, $\hbar\omega_0$. The arrows indicate that atoms located near $50S$ potential maxima (minima) and driven from $50S \rightarrow 51S$ have transition frequencies that are red-shifted (blue-shifted) from the unperturbed transition frequency.

unperturbed $50S \rightarrow 51S$ transition frequency (which is $\omega_0 \approx 2\pi \times 61.92$ GHz). The microwave spectrum for $\eta = 0$ exhibits three features, labeled A, B, and C. Feature A is associated with untrapped atoms without much kinetic energy that spend the majority of the microwave-interaction time near the lattice potential maxima. This feature is red-shifted in transition frequency since the potential for the $51S$ state is slightly shallower than for $50S$, as illustrated in Figure 3.4 (see also Section 1.3.2). Atoms that are located near $50S$ potential maxima and driven from $50S \rightarrow 51S$ are red-shifted in transition frequency. Feature B is due to untrapped atoms with enough energy that their trajectories traverse several lattice wells. Since these atoms sample many regions of the lattice, the shift of this feature averages to near zero. The B-signal is still slightly red-shifted since the atoms spend more time near the potential maxima, where their kinetic energy is less. The blue-shifted feature C is largely due to atoms trapped in a single lattice well. Due to the linewidth of the excitation lasers, these atoms are excited partway down the lattice wells and lack enough energy to escape those wells. Atoms located near potential minima are blue-shifted in transition frequency since the $51S$ state is slightly shallower than $50S$, as illustrated in Figure 3.4. Without a lattice inversion, the C-signal in Figure 3.5(a) is weak, showing that only a few percent of the Rydberg atoms are trapped. The case $\eta = 0$ is analyzed in detail in References [41, 73].

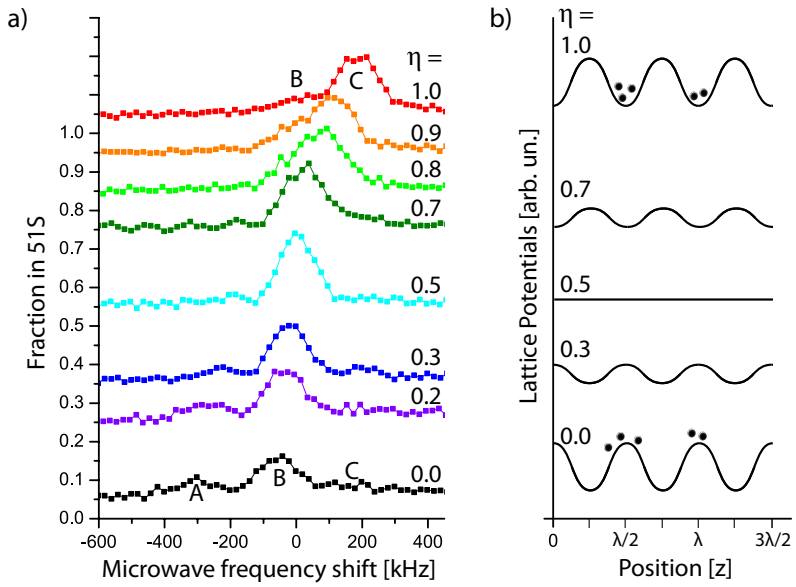

Figure 3.5: a) Experimental microwave spectra for the indicated values of $\eta = P_{\mathrm{trans}}/P$ for an ingoing lattice beam power of 0.8 W and optical pulse length $\tau_{\mathrm{ex}} = 0.5$ μs (spectra offset for clarity). b) Lattice potentials after inversion vs. position for several of the η-values used in panel (a). The fully inverted case, $\eta = 1$, leads to the strongest blue-shifted signal component, indicative of most efficient Rydberg-atom trapping.

In Figure 3.5(a), I show microwave spectra for several values of η. As η is increased from 0 to 1, the signal shifts almost entirely into the C-component, which presents a qualitative measure for the fraction of trapped atoms. Hence, the $\eta = 1$ spectrum demonstrates that the fully inverted lattice forms a highly efficient Rydberg-atom trap. The high trapping efficiency occurs because the Rydberg atoms do not move significantly during the optical excitation pulse length ($\tau_{\mathrm{ex}} = 0.5$ μs) and the 0.2 μs lattice inversion time. Following the lattice inversion, the atoms find themselves trapped at a minimum of the Rydberg-atom trapping potential, despite the fact that they were initially excited at a maximum of that potential. Integrating the areas under the B and C-signals in the curve for $\eta = 1$ in Figure 3.5(a), we obtain a first estimate of the trapping efficiency of about 80%. However, we expect this estimate to be too low because the red-detuned Fourier side peaks of the strong C-component overlap with the relatively weak B-component.

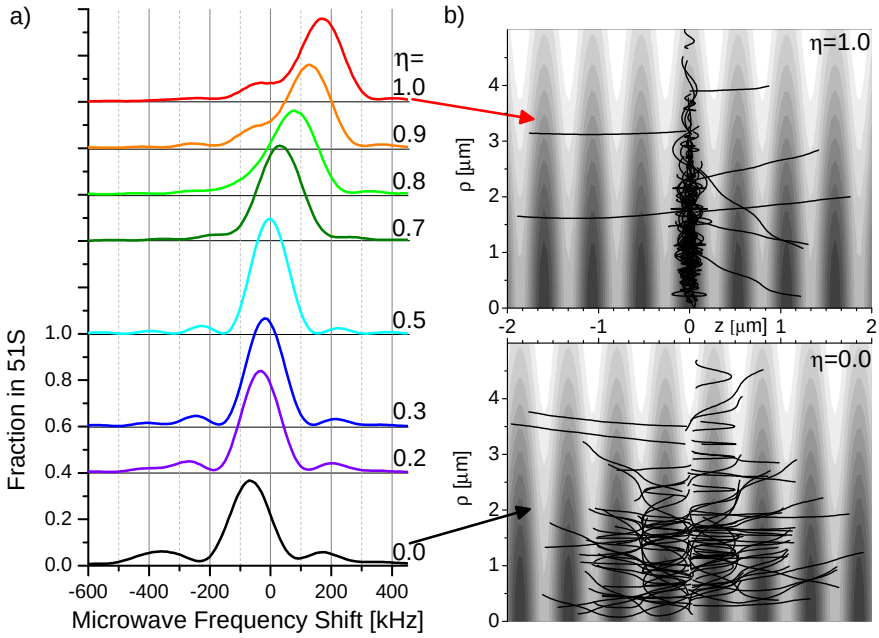

Figure 3.6: a) Simulated microwave spectra for the indicated values of $\eta = P_{\text{trans}}/P$ and the same conditions as in Figure 3.5. b) Simulated atomic trajectories for the cases of no inversion (bottom) and complete inversion (top). The Rydberg-atom trapping potential is shown in the background on a scale from 3 MHz (dark) to 15 MHz (white).

In order to obtain a more accurate estimate of the trapping efficiency, we perform simulations to model the entire microwave spectrum (the simulations are very similar to those described in Reference [41]). In the simulations, the internal dynamics are treated quantum mechanically, and the external dynamics are treated classically, which is allowable because of the depth of the Rydberg-atom lattice wells (≈ 10 MHz for $50S$, which is much larger than the recoil energy of ≈ 2 kHz). Initial positions and velocities of $5S$ atom ensembles are assumed to follow a Maxwell-Boltzmann distribution in the ground-state trapping potential (temperature $T \simeq 100$ μK, which is on the order of the laser cooling Doppler limit for Rb). After randomly selecting positions and momenta from this distribution, the probabilities that the atoms are excited to $50S$ is determined. The optical excitation $5S \rightarrow 50S$ is assumed to be resonant at the lattice intensity maxima, where the $5S$ atoms collect, and we assume low

saturation and an excitation bandwidth of 3 MHz (the measured width of lattice-free optical Rydberg resonance lines). The classical center-of-mass Rydberg-atom trajectories follow from the V_{ad} trapping potential calculated for $50S$ from Equation 1.6 and are computed using a fourth-order Runge-Kutta method. Note that while the atomic state is actually a coherent superposition of $50S$ and $51S$, the trajectories are determined from the $50S$ potential. (The difference in the $50S$ and $51S$ potentials is only 1.8%, causing negligible effects on the trajectories over the timescales of interest.) The atom-lattice interaction times are randomly chosen between 6 μs and 6 μs+τ_{ex}, consistent with the timing used in the experiment. Since the frequency of the $50S \rightarrow 51S$ transition depends on the location of the atoms as they move through the lattice potential, the detuning of the microwave transition is time-dependent. The microwave-driven quantum evolution in the internal state space $\{|50S\rangle, |51S\rangle\}$ is computed along the trajectories by integrating the time-dependent Schrödinger equation. In Figure 3.6, we show theoretical spectra obtained for our experimental conditions, as well as 100 typical Rydberg-atom trajectories for the cases $\eta = 0$ and $\eta = 1$.

Most parameters in the simulation have values known from the experiment. The Rabi frequency of the microwave transition is set to a fixed value at which the on-resonant $50S \rightarrow 51S$ transition probability is 50% when the lattice is off (which we use as a calibration point in the experiment). The measured powers of the ingoing and return lattice beams and the measured FWHM diameter of the ingoing lattice beam (13 μm) are also entered as fixed values. The only free fit parameters of the simulation are the initial atom temperature T and the FWHM diameter of the return lattice beam, w_{r}, which could not be measured.

Excellent agreement between experimental and simulated microwave spectra is found for $w_{\mathrm{r}} = 25$ μm and $T = 100$ μK (used in Figure 3.6), with respective estimated uncertainties of 2 μm and 20 μK. For these parameters, we find that 90% of the atoms are trapped in the fully inverted lattice ($\eta = 1$). We have studied how sensitive

this result is to these parameters. Over a temperature range of 40 μK to 300 μK, the trapping efficiency decreases approximately linearly from 99% to 64%, with all other parameters unchanged. Variation of w_{r} from 13 μm to 40 μm leads to a linear drop of the trapping fraction from 95% to 84%. Hence, the temperature T affects the Rydberg-atom trapping efficiency the most. The w_{r} is larger than the FWHM diameter of the ingoing beam because of cumulative aberrations caused by the optical components in the retroreflection beam path. This retroreflection beam path includes two passes through a vacuum window, a lens, and a quarter waveplate, as well as multiple reflections within the retroreflector (see Figure 3.2).

The simulated atomic trajectories of Figure 3.6(b) confirm our interpretations of the features A−C in the microwave spectra. For $\eta = 0$, the atomic trajectories span over several wells, with only a few trapped trajectories. The simulation therefore shows limited Rydberg-atom trapping for no lattice inversion. For $\eta = 1$, the trajectories are confined to a lattice well, with only a few escaped trajectories. The simulation therefore shows high Rydberg-atom trapping efficiency for a complete lattice inversion.

3.4 Characterizing the trap

Now that I have established that the ponderomotive optical lattice traps Rydberg atoms with 90% efficiency, I characterize the lattice's trapping capabilities. Specifically, I investigate the dependence of the trapping efficiency on excitation pulse duration and lattice power, the photoionization of Rydberg atoms by lattice light, and the trap lifetime.

3.4.1 Dependence of trapping efficiency on excitation pulse duration

Experimental microwave spectra for selected values of excitation pulse length, τ_{ex}, and $\eta = 1$ are shown in Figure 3.7(a). As τ_{ex} is increased, the C-signal in the

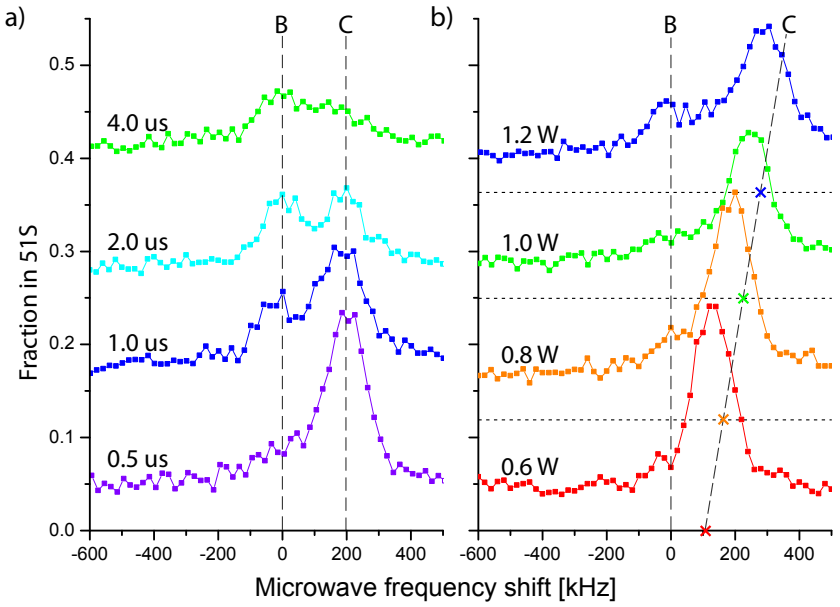

Figure 3.7: Effect of varying excitation pulse length τ_{ex} and lattice power on trapping efficiency for $\eta = 1$ (complete lattice inversion). a) Varying τ_{ex} at a fixed lattice power, ingoing lattice beam power of 0.8 W. b) Varying the lattice power at a fixed $\tau_{ex} = 0.5$ μs.

microwave spectra diminishes while the B-signal grows. Lower values of τ_{ex} therefore result in higher trapping efficiencies. This is because Rydberg atoms are excited at random times during the excitation pulse; however, the lattice is not inverted until the completion of the excitation pulse. For shorter τ_{ex}, the Rydberg atoms have, on average, less time to slide down the lattice potential wells before the lattice is inverted. The atoms then gain less kinetic energy, resulting in better trapping.

3.4.2 Dependence of trapping efficiency on lattice power

In Figure 3.7(b), I show microwave spectra for several values of the lattice power (values given are for the ingoing lattice beam). The detuning of the C-peaks scales linearly with trap laser power, as expected. For the three lowest powers of Figure 3.7(b), the spectral signal is almost entirely in the C-component, indicating efficient Rydberg-atom trapping. For the highest power of 1.2 W, the emerging B-signal indicates a loss in trapping efficiency. Simulations analogous to the ones in Figure 3.6 show that this

loss is in part due to a temperature increase of the optically trapped ground-state atoms to about 160 μK. The temperature increase is attributed to a deterioration of laser cooling, as the red-detuning of the MOT cooling light approaches ten linewidths in the ground-state potential wells. This is supported by Figure 2.8 that displays optical excitation spectra in the lattice as a function of lattice power. The spectra show that the ground-state atoms are less well-localized near the bottoms of the lattice wells for an ingoing lattice beam power $\gtrsim 1$ W, indicating a deterioration in laser cooling for deep lattice wells. Also, as the lattice power is increased in Figure 3.7, the excited atoms (partially) slide down steeper lattice potential wells before lattice inversion. Therefore, the kinetic energy that the atoms gain between optical excitation and lattice inversion increases with lattice power. The simulations show that this effect is noticeable even at $\tau_{\mathrm{ex}} = 0.5$ μs. As a result of both effects, the kinetic energy of the Rydberg atoms is higher in deeper lattices, leading to reduced Rydberg-atom trapping efficiency. However, this is not a fundamental limitation on the trapping efficiency. High trapping efficiencies in deep lattices can be achieved by adiabatically increasing the lattice intensity.

3.4.3 Photoionization effects

Since the Rydberg atoms are trapped by a relatively intense light field, it is important to consider if there are any additional effects of the field on the atoms. For example, the Rydberg atoms may be ionized by the lattice light. To study lattice-induced photoionization, which could be a concern in applications, I have measured the Rydberg atom number as a function of delay time between excitation and detection. For $50S$ Rydberg atoms, measurements with and without the optical lattice show exponential decays with nearly identical lifetimes of ≈ 100 μs, seen in Figure 3.8. Hence, there is no photoionization of $50S$ atoms in the lattice, and the decay is entirely due to radiative decay and decay induced by black-body radiation. The

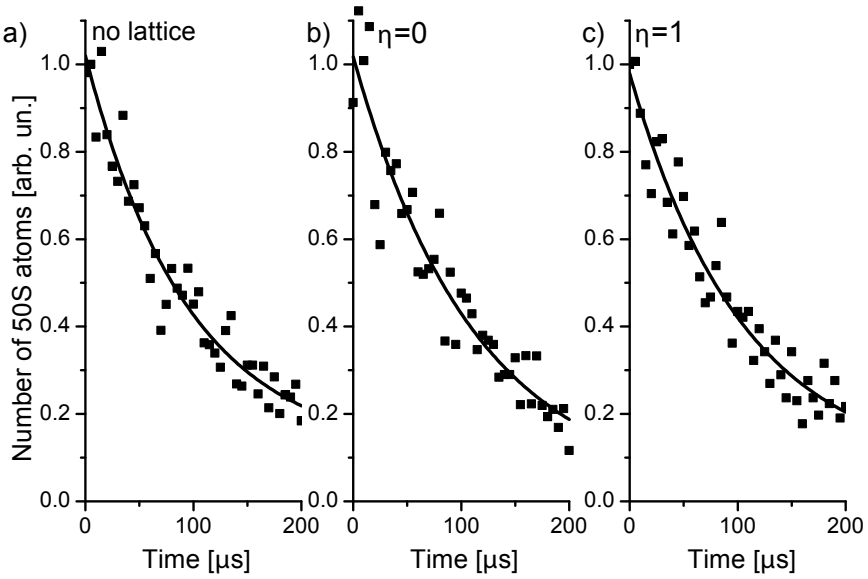

Figure 3.8: $50S$ atom number vs. time after excitation without (a) and with lattice for $\eta = 0$ (b) and $\eta = 1$ (c). All decay rates (a-c) are nearly identical, yielding lifetimes of about 100 μs. Photoionization effects are therefore too small to be measurable.

measured decay times are in line with anticipated values [74]. The absence of measurable photoionization rates reflects the low photoionization cross sections of S Rydberg levels of Rb. The low photoionization cross sections are due to a minimum in the oscillator strength for transitions from S states of Rb into P states in the continuum just above the ionization limit. This minimum, called a Cooper minimum, results from the phases of the S and P wavefunctions being different by $\pi/2$ (due to the quantum defects for the two states differing by ≈ 0.5, see Reference [26] for a more thorough discussion). Reference [59] shows a photoionization cross section of about 45 barns for the $50S$ state[2], while we have calculated 65 barns (see Section 6.4). Under our experimental conditions, these cross sections translate into photoionization rates < 100 s^{-1}, which are too small to be detectable.

For comparison, I have studied the decay of $50D_{5/2}$ Rydberg atoms, for which both Reference [59] and our calculations show a photoionization cross section of about 1.3×10^4 barns. Here, there is clear evidence of photoionization, as Figure 3.9(a),(b)

[2] 1 barn $= 10^{-28}$ m^2.

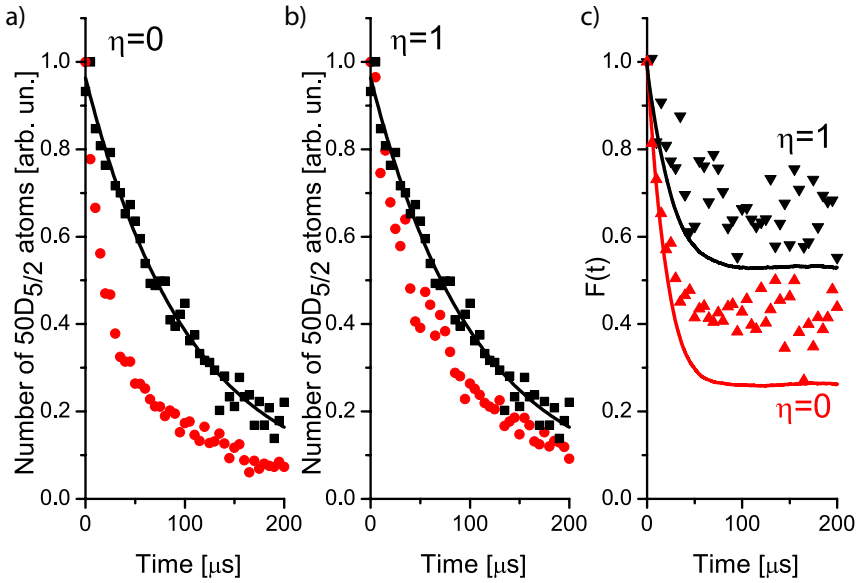

Figure 3.9: a), b) Measurements of lattice-induced photoionization of $50D_{5/2}$ Rydberg atoms in the optical lattice (ingoing beam power of 0.8 W). Atom number vs. time after excitation without (black squares) and with lattice (red circles) for $\eta = 0$ (a) and $\eta = 1$ (b). The data without lattice are fit with an exponential function (lifetime 100 ± 15 μs). c) Symbols: ratios $F(t)$, which equal the number of $50D_{5/2}$ atoms with the lattice divided by the number without the lattice as a function of time, obtained from the experimental data in panels (a) and (b). Lines: simulation results.

demonstrate that $50D_{5/2}$ atoms in the lattice (red circles) decay considerably faster than atoms without lattice (black squares). Also, photoionization occurs faster without lattice inversion ($\eta = 0$) than with inversion ($\eta = 1$). This is because the lattice inversion places the atoms at a lattice intensity minimum immediately after excitation, where the photoionization rate is lower. More detailed investigations of photoionization of Rydberg atoms in the lattice can be found in Chapters V and VI.

3.4.4 Trap lifetime

To estimate the typical trapping time of Rydberg atoms in the lattice, I use photoionization as a tool to probe how long the atoms stay in the lattice. I measure the ratio $F(t)$ of the Rydberg-atom number with the lattice on divided by the number with the lattice off for the $50D_{5/2}$ state. The following considerations illustrate how

the ratio $F(t)$ allows for an estimation of the atom dwell time in the lattice. While the atoms are in the lattice, they decay at a faster rate than the atoms without the lattice, due to the added effect of photoionization; the ratio $F(t)$ will decrease in this case. When the atoms have left the lattice, they decay at the same rate as the atoms without the lattice, and the ratio $F(t)$ will be a constant value. Thus, the time at which $F(t)$ reaches a steady-state value indicates the time when all the atoms have left the lattice or have been ionized.

Experimentally, I determine $F(t)$ by dividing the decay data from Figure 3.9(a),(b) in the lattice (red circles) by that without the lattice (black squares). The results for $F(t)$ are shown in Figure 3.9(c). $F(t)$ has an initial value of 1.0, since at $t = 0$ there has been no time for photoionization to happen. The number of atoms with the lattice is the same as the number of atoms without the lattice. $F(t)$ then drops to asymptotic values that are reached when all Rydberg atoms in the lattice either have photoionized or have moved out of the lattice and are decaying at the same rate as the atoms without the lattice. Hence, the $F(t)$ data shows the time over which the lattice has an effect on the decay of the state. I define the average dwell time to be the time at which $F(t)$ drops by half of the total drop. Inspecting the $F(t)$ curves of Figure 3.9(c), I estimate average dwell times of about 15 μs for $\eta = 0$ and somewhat larger values for $\eta = 1$. In the inverted case $\eta = 1$, the dwell time is expected to be longer because the photoionization rate is lower and because the atoms leave the lattice more slowly, as there is a smaller transverse gradient force pushing them out of the lattice.

Using the known trapping potentials, photoionization cross sections, and lattice-free decay rates, we have simulated the lattice-induced dynamics of $50S$ and $50D_{5/2}$ Rydberg atoms over 200 μs, taking photoionization and radiative decay processes into account. We find that the $50S$ and $50D_{5/2}$ atoms exhibit similar dwell times of several tens of μs in the lattice. As seen in the experiment, the $50D_{5/2}$ atoms undergo some

photoionization-induced decay while they move out of the lattice. Photoionization is insignificant for the $50S$ atoms. Simulated curves for $F(t)$, included in Figure 3.9(c), qualitatively agree with the experimental results. We attribute the deviations at late times to an unaccounted-for reduction in photoionization cross section, which occurs when atoms transition from $50D_{5/2}$ into neighboring P- or F-states (mainly due to black-body radiation [26]). As will be seen in Figure 6.3, D states have the largest photoionization cross sections for Rb. Therefore, a transition into any neighboring state will reduce the photoionization cross section for the atoms in the experiment and thereby also reduce the overall photoionization yield integrated over time.

3.5 Conclusion

I have shown that a lattice inversion technique enables Rydberg-atom trapping in a red-detuned optical lattice with 90% efficiency. The trapping efficiency is expected to approach 100% after reduction of the initial atom temperature. Currently, the atoms in the lattice still lack confinement in the radial direction. With the addition of radial confinement, which would provide three-dimensional trapping, we can expect a trapping time identical to the Rydberg-atom decay time (≈ 100 μs for $50S$). Such a trapping time would be long enough for a sequence of gate operations in quantum information applications or for high-precision spectroscopy applications. Three-dimensional optical lattice traps for Rydberg atoms are discussed in Section 7.1.

After demonstrating the trapping of Rydberg atoms in the ponderomotive optical lattice, another important step in the development of this Rydberg-atom trap is a characterization of its unique state-dependent trapping potentials. While the dependence of the potentials on the principal quantum number was demonstrated using spherically symmetric S-states in 2010 [41] and was utilized in this chapter to probe the trapping efficiency of the lattice, the dependence on angular degrees of freedom

had not yet been investigated. In the next chapter, I characterize the ponderomotive optical lattice trapping potentials for various angular Rydberg states. The ability to tune the potentials using angular degrees of freedom will be important for applications of Rydberg-atom optical lattices in both quantum computing and high-precision spectroscopy, where it is desirable to minimize trap-induced shifts on transitions of interest.

CHAPTER IV

Angular Dependence of Rydberg-atom Trapping Potentials in an Optical Lattice

In optical lattices of all kinds, the dependence of the optical potentials on the magnetic quantum number, m, is of fundamental importance. For ground-state atoms, this dependence has been well known since the late 1980s [75, 76] and has been widely exploited in laser cooling experiments, for example in achieving sub-Doppler temperatures through the mechanism of Sisyphus cooling [54]. In optical lattices for Rydberg atoms, an analogous dependence of the trapping potentials on the m quantum number has not been previously observed. The m-dependence of the lattice potentials affects both the trapping behavior as well as lattice-induced shifts of electromagnetic transitions of the atoms in the lattice. The tunability of the Rydberg-atom trapping potentials using the angular degrees of freedom will be important for applications of Rydberg-atom optical lattices. For instance, in quantum computing applications of such lattices [4], it is desirable to tailor the lattice in such a way that lattice-induced shifts of ground- to Rydberg-state transitions are minimized. In high-precision spectroscopy applications [31], it will also be beneficial to minimize the lattice-induced shifts of microwave transitions between selected Rydberg levels. The angular degrees of freedom will provide a way to tailor the lattice potentials to minimize these lattice-induced shifts in quantum computing and high-precision spectroscopy applications.

In this chapter, I investigate the angular dependence of the ponderomotive optical lattice potentials for Rydberg atoms.

4.1 Angular dependence of lattice potentials for ground and Rydberg states

The lattice potentials for atoms in low-lying or in Rydberg states are generally expected to depend on (j, m_j); however, the reasons for that dependence are quite different in the two cases. For atoms in low-lying states, the lattice potential arises from an AC electric dipole moment between bound atomic states (see Section 2.1.2), and the (j, m_j)-dependence reflects the differences of Clebsch-Gordan coefficients in the atom-field interaction [77]. This leads to intensity- and polarization-dependent trapping potentials.

In contrast, for Rydberg atoms in ponderomotive optical lattices, the trapping results from the free-electron polarizability, as discussed in Section 1.3.2. The adiabatic potentials for Rydberg atoms in a ponderomotive optical lattice (V_ad, see Equation 1.6) are a spatial average of the free-electron ponderomotive energy weighted by the Rydberg electron's probability distribution [40]. Since the Rydberg-atom wavefunction covers a substantial fraction of the lattice period, the detailed shape of the wavefunction will determine the averaging in Equation 1.6. The V_ad therefore depend on all quantum numbers (n, l, j, m_j). In previous work performed in the Raithel research group, the dependence of the adiabatic trapping potentials of the ponderomotive optical lattice on the principal quantum number, n, has been experimentally demonstrated using various Rydberg nS states (which do not exhibit angular substructure) [41].

The angular portion of the Rydberg wavefunction can have a dramatic effect on the averaging in Equation 1.6, resulting in a (j, m_j)-dependence of the adiabatic po-

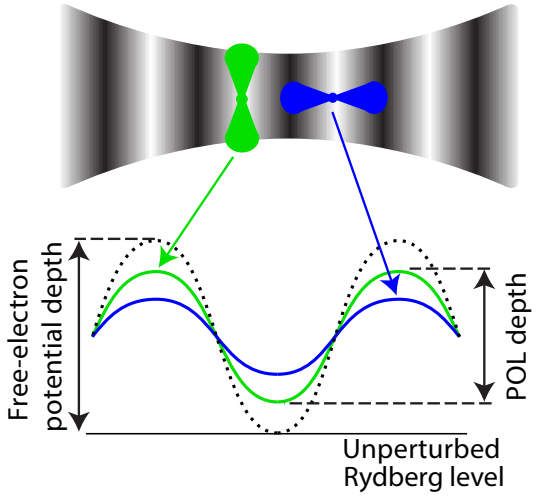

Figure 4.1: Angular dependence of the ponderomotive optical lattice potentials for Rydberg atoms. A Rydberg state with wavefunction extended mostly transverse to the lattice axis (green) averages over less of the free-electron potential and consequently experiences a more deeply modulated potential in the lattice than a wavefunction elongated in the direction of the lattice axis (blue).

tentials. As illustrated in Figure 4.1, states having wavefunctions extended mostly transverse to the lattice axis (green case in Figure 4.1) experience more deeply modulated lattice potentials than those elongated in the direction of the lattice axis (blue case). The adiabatic potentials obtained from Equation 1.6 depend on light intensity but not on polarization. In the work presented in this chapter, I demonstrate the dependence of the lattice trapping potentials on the angular portion of the Rydberg wavefunction by measuring the ponderomotive optical lattice depth (indicated in Figure 4.1, given by lattice modulation depth) for several (j, m_j) sublevels of Rydberg nD states.

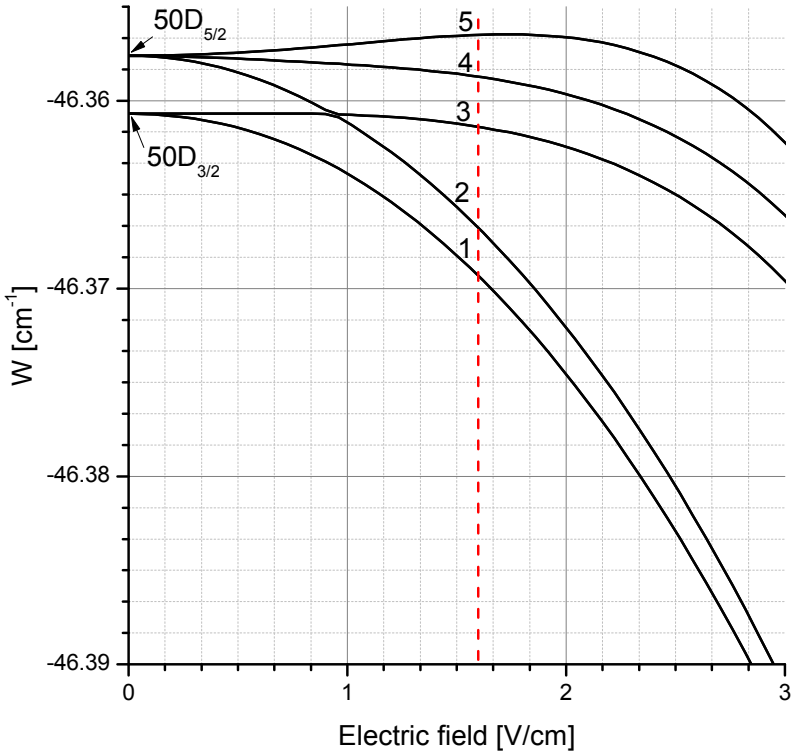

Figure 4.2: Calculated $50D$ level in a DC electric field. The degeneracies of the $|m_j|$ sublevels are lifted through the Stark effect. The red dashed line corresponds to the electric field value used in the experiments. The levels are labeled in order of increasing energy.

4.2 Experimental setup

4.2.1 DC electric field

Since the various $(j,\ m_j)$ sublevels of Rydberg nD states have different angular wavefunctions and consequently also different lattice modulation depths, I must measure each m_j sublevel individually. For nD levels in zero fields, there is the fine structure splitting of $nD_{3/2}$ and $nD_{5/2}$, and all the m_j sublevels for the same j are degenerate. In order to investigate the lattice potentials for the $(j,\ m_j)$ sublevels individually, it is necessary to lift degeneracies to allow for selective excitation of the sublevels. I therefore apply a DC electric field, which shifts the sublevels of the nD states according to the magnitude of m_j. Figure 4.2 shows an example of the calcu-

lated Stark splitting of the $50D$ Rydberg level in a DC electric field. The levels $50D_{3/2}$ and $50D_{5/2}$ split into a total of five Stark substates in the DC field, since there are three values of $|m_j|$ for $50D_{5/2}$ and two values for $50D_{3/2}$. The five Stark substates are labeled in order of increasing energy in the field. In the limit of small DC field, the five components connect with the following levels: (1) $50D_{3/2}$ $|m_j|$=3/2, (2) $50D_{5/2}$ $|m_j|$=5/2, (3) $50D_{3/2}$ $|m_j|$=1/2, (4) $50D_{5/2}$ $|m_j|$=3/2, and (5) $50D_{5/2}$ $|m_j|$=1/2. The fact that the $\pm m_j$ levels remain degenerate in the DC field has no effect on our measurements, since the shape of the wavefunction is the same for both levels; both levels therefore average over the free-electron ponderomotive potential equally and experience the same modulation depth in the lattice. The red dashed line in Figure 4.2 indicates the electric field value where the experiments are performed for $50D$. For technical reasons[1], the DC field in the experiment is oriented transverse to the axis of the lattice. With the DC field applied, the Stark effect is the dominant perturbation, with a quantization axis transverse to the lattice beams.

Figure 4.3 shows an experimental spectrum of the $50D$ Rydberg level in both the lattice and a transverse DC electric field of 1.6 V/cm, obtained by scanning the frequency of the upper transition excitation laser. As expected, the $50D_{3/2}$ and $50D_{5/2}$ levels split into a total of five components, labeled again in Figure 4.3 in order of increasing energy. The large peaks for each component are signal from atoms outside of the lattice (red solid arrows indicate two examples in Figure 4.3), while the blue-shifted triangular structures reflect the shifts of the optical transition frequency due to the lattice trapping potentials. Since the atoms are laser-cooled near the bottoms of the $5S$ lattice wells, the lattice-induced structures in the spectrum exhibit a sharp cutoff on the high frequency side (for example, see dashed arrows in Figure 4.3). For more on the shape of optical excitation spectra in the lattice, see Section 2.3.

[1]See geometry of electrodes in Figure 2.4(a).

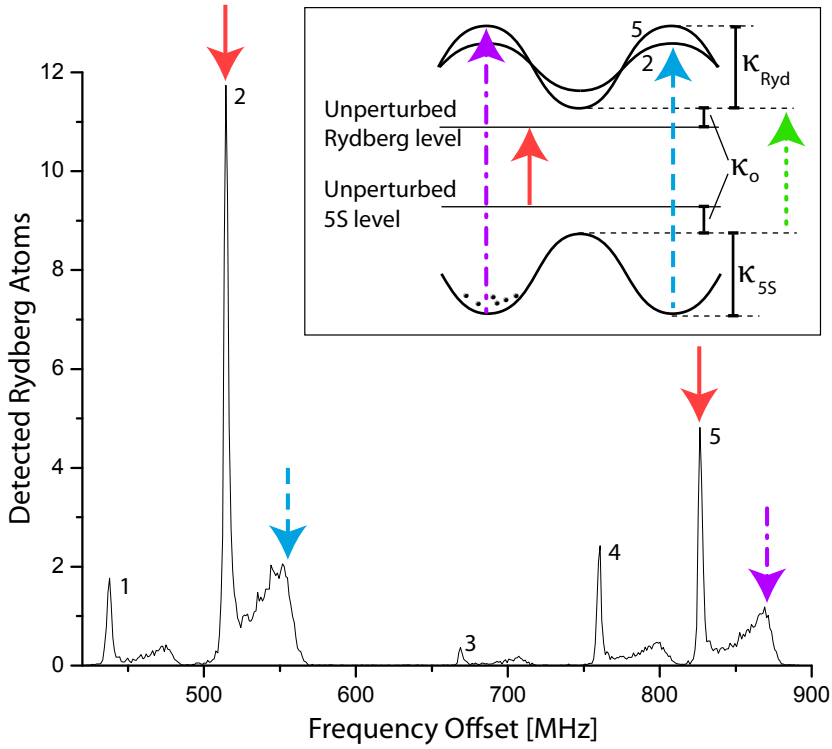

Figure 4.3: Experimental optical excitation spectrum of the $50D$ Rydberg level in the lattice and a transverse DC electric field. The Stark components, labeled 1-5, exhibit structures on the high-frequency side that reflect lattice-induced shifts of the optical transitions. Inset: Ground and Rydberg levels in the lattice. The arrows indicate how the maxima in the experimental spectrum correlate with the shapes of the lattice potentials.

4.2.2 Lattice-induced shifts and measurement procedure

The blue-shifted structures in the spectrum shown in Figure 4.3 yield information on the depth of the Rydberg lattice for the different Stark levels, which we expect to vary in depth. The maximum lattice-induced shift consists of the ground-state modulation depth (κ_{5S} in the inset of Figure 4.3), the Rydberg-state modulation depth (κ_{Ryd}), and an offset (κ_{o}). Here, I am interested in how κ_{Ryd} depends on the angular structure of the five Stark levels. The inset of Figure 4.3 shows that κ_{Ryd} can be obtained by subtracting κ_{5S} and κ_{o} from the measured maximum lattice-induced shift. The procedure for determining the ground-state lattice depth, κ_{5S}, is explained in Appendix B. The offset κ_{o} can arise from an imbalance of the intensities of the

lattice beams, leading to a reduced lattice intensity modulation depth. The reduced intensity modulation depth affects both the ground and Rydberg levels. There is also a contribution to κ_o from the intrinsic averaging of the Rydberg-atom wavefunction over the free-electron ponderomotive potential in Equation 1.6. Due to the averaging, the modulation of the Rydberg level does not reach zero even in a perfectly intensity-modulated lattice. For an independent measurement of κ_o, I invert the lattice potential immediately *before* Rydberg-atom excitation using the electro-optic technique described in Section 3.2 and Reference [66]. Following the lattice inversion, the ground-state atoms are located near maxima in the ground-state potential. Before they move away, they are excited to minima of the Rydberg-state potential (green dotted arrow in the inset of Figure 4.3 and corresponding curve in Figure 4.4). Measurement of the lattice-induced shift in the inverted lattice case yields κ_o.

In the experimental spectra, signal from atoms outside of the lattice (solid red arrows in Figure 4.3) tends to overwhelm the desired signal from the atoms inside the lattice. To address this issue, I apply the Dumper pulse (see Section 2.3.2) between the turnoff of the MOT laser beams and the application of the excitation pulses. Following the Dumper pulse, only the F=3 atoms left in the lattice are accessible for optical excitation to the Rydberg state, resulting in a cleaner spectrum of the lattice-induced shifts.

In Figure 4.4, I show typical optical excitation spectra of level 2 from Figure 4.3 for the two cases of an inverted and a non-inverted lattice, which illustrate how to obtain a measurement of κ_o and subsequently extract κ_{Ryd}. While the frequency of the upper transition excitation laser is stepped in the experiment (see Section 2.2.1) to take the spectrum shown in Figure 4.4, I engage the Dumper pulse for frequencies higher than about 5 MHz. This leaves the unshifted signal (the large peak at 0 MHz) as a frequency reference. Figure 4.4 clearly shows that the peak in the inverted-lattice spectrum (indicated by the green dotted arrow) is shifted from that in the case of the

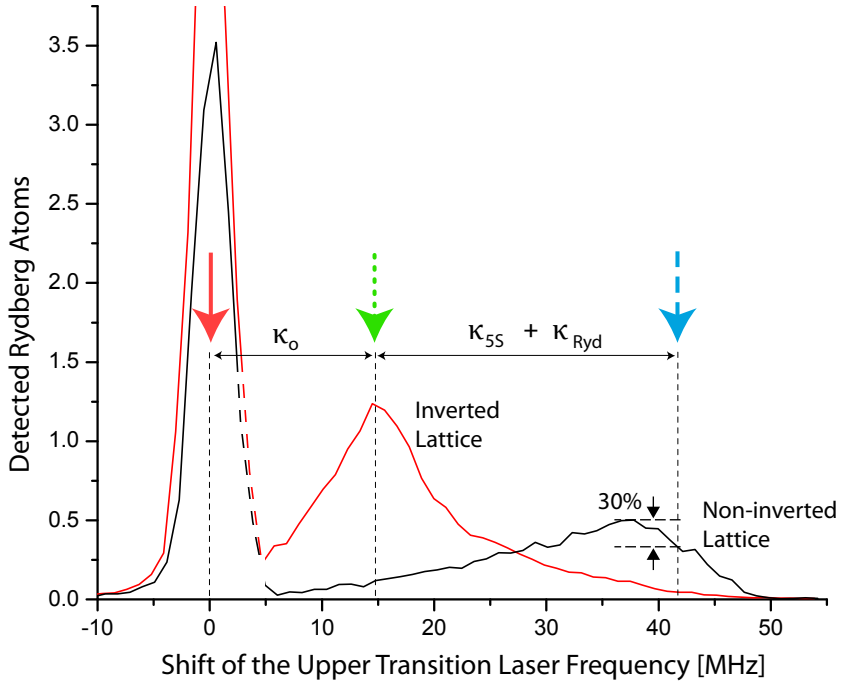

Figure 4.4: Experimental optical excitation spectra for level 2 of Figure 4.3 in a transverse DC field and a non-inverted lattice and inverted lattice. Spectral features, indicated by arrows, enable a measurement of the Rydberg-state lattice depth (κ_{Ryd}).

non-inverted lattice (indicated by the blue dashed arrow). As indicated in the figure, I use these peak positions to determine the shifts κ_{o} and $\kappa_{\mathrm{o}} + \kappa_{5\mathrm{S}} + \kappa_{\mathrm{Ryd}}$.

To extract κ_{Ryd} from the spectra, one must consider exactly how the experimentally observed peaks in the lattice-induced features are related to the various values of κ. For the inverted lattice, the ground-state atoms are located near a saddle point of the light shift potentials, which is illustrated in Figure 4.5(a) and results from the mismatched spot sizes of the two lattice beams (see Sections 2.3 and 3.3). The atoms sitting at this saddle point see a decreasing potential in the longitudinal z-direction, along the lattice axis, and an increasing potential in the radial direction. The corresponding peak in the excitation spectrum (green dotted arrow in Figure 4.4) is broadened both to the low- and high-frequency sides, due to atoms that are displaced from the saddle point radially and longitudinally relative to the lattice axis, respectively. Due to the balanced broadening, the peak center gives an accurate reading for

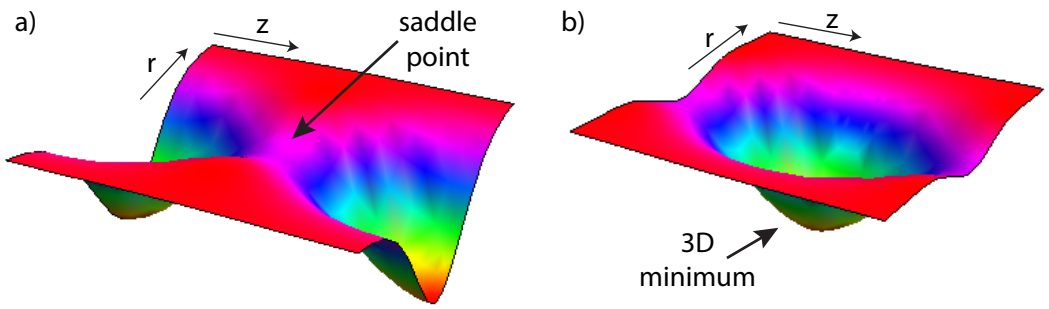

Figure 4.5: Calculated potentials for ground-state atoms in the lattice with and without a lattice inversion. a) Saddle point in the potential following the lattice inversion. b) Three-dimensional potential minimum with no lattice inversion.

the offset κ_{o}.

In contrast, for the non-inverted lattice the ground-state atoms are located near a three-dimensional intensity maximum, not a saddle point. This three-dimensional intensity maximum is also a three-dimensional potential minimum for the ground-state atoms and is illustrated in Figure 4.5(b). Any thermal spread of the atoms away from the intensity maximum causes a shift of the Rydberg-atom excitation frequency to lower frequencies. Hence, in the non-inverted lattice the excitation spectrum is only broadened to the low frequency side, and the peak in the spectrum is shifted toward lower frequency. To obtain a quantitative estimate for how far the peak is shifted toward lower frequency, we have simulated the excitation spectrum for temperatures ranging from $100 - 300$ μK for light-shift potentials that correspond to our experiment. The simulated spectra show that the frequency corresponding to a one-third drop in signal from the peak (blue dashed arrow in Figure 4.4) approximates the value of $\kappa_{\mathrm{o}} + \kappa_{5\mathrm{S}} + \kappa_{\mathrm{Ryd}}$ to within ± 1 MHz. We therefore use this one-third drop in signal as our measurement point in the experiment. The procedure is indicated in Figure 4.4. With this measurement for $\kappa_{\mathrm{o}} + \kappa_{5\mathrm{S}} + \kappa_{\mathrm{Ryd}}$, the reading for κ_{o}, and the value of $\kappa_{5\mathrm{S}}$, I obtain the Rydberg lattice depth κ_{Ryd}.

To investigate the angular dependence of the ponderomotive optical lattice potentials, I repeat the procedure explained in Figure 4.4 for several other nD Stark levels

with $50 \leq n \leq 65$. In all cases, the DC electric field value is chosen so that the level structure is consistent with that shown in Figure 4.2 (at the red dashed line). The measurement results for κ_{Ryd} are listed in Table 4.1.

Table 4.1: POL depth measurement results.

Level	Measured κ_{Ryd} (MHz)	Label
$65D$ level 2	-4.1±3	A
$55D$ level 2	1.4±3	B
$50D$ level 2	4.5±3	C
$65D$ level 5	1.1±3	D
$55D$ level 5	10.0±3	E
$50D$ level 5	9.5±3	F

4.3 Ponderomotive optical lattice potential depths and uncertainties

The measured values of κ_{Ryd} shown in Table 4.1 clearly vary from state to state, demonstrating the angular dependence of the Rydberg lattice depth. I also compare the measured results with calculated κ_{Ryd} values for the cases studied in the experiment. In the calculation, the depth of the Rydberg adiabatic potentials is obtained by numerical diagonalization of the Rydberg atoms' internal-state Hamiltonian at the light-field maxima and minima. The lattice depth for a given Rydberg level is determined by the difference between that level's energy at these two locations. Note that the computation requires large Rydberg-state basis sets, since the system does not have any continuous symmetry in crossed DC electric and optical lattice force fields. In Figure 4.6(a), the experimental measurements of κ_{Ryd} are plotted against the calculated values. The data follow the expected trend, as the linear fit to the data has a slope of one and passes through the origin within the bounds of the fitting uncertainty. In Figure 4.6(b), the experimental measurements of κ_{Ryd} (black squares) are plotted along with the calculated values (red circles). There is good agreement

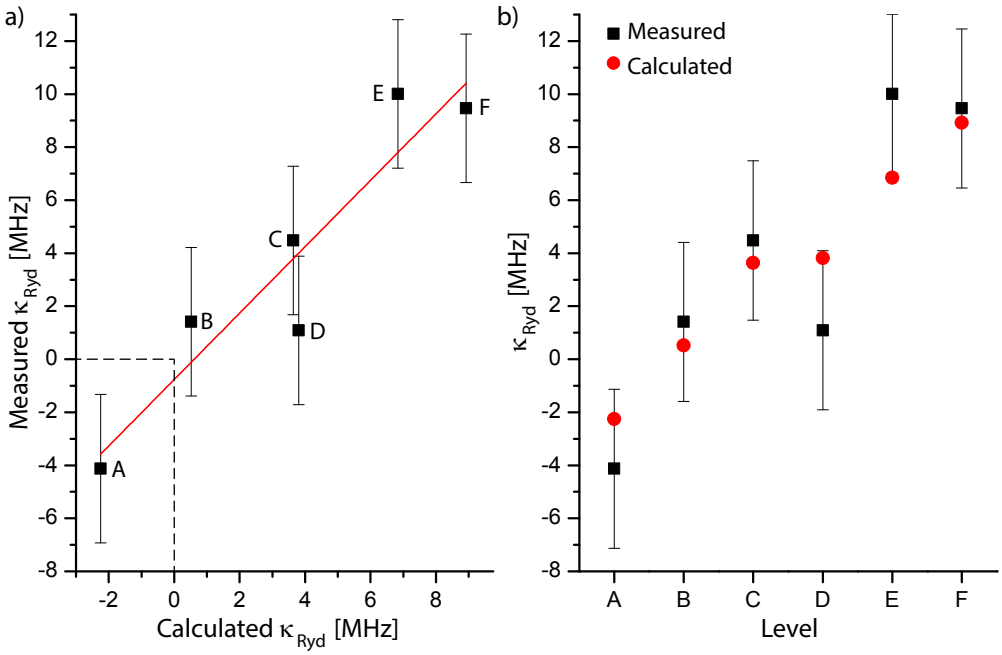

Figure 4.6: a) Symbols: Measured vs. calculated POL potential depths for the levels listed in Table 4.1. The error bars reflect systematic and measurement uncertainties. Line: A linear fit to the data points. b) Symbols: Measured (black squares) and calculated (red circles) POL potential depths for the same levels as in (a).

between the measured and calculated depths.

The error bars in Figure 4.6 reflect the measurement and systematic uncertainties associated with the data. The measurement uncertainty is ± 1 MHz and mostly arises from the uncertainty in measuring the lattice-induced shift in the non-inverted lattice, as described above. Systematic error sources include daily variations in optical lattice alignment. Comparing day-to-day results, I estimate an alignment-induced uncertainty of ≈ 2 MHz. Since the excitation laser is locked to a Fabry-Pérot cavity (see Section 2.2.1), a source of systematic error is also thermal drift of the Fabry-Pérot. Monitoring the count rate as a function of time with the laser initially set to the peak of a Rydberg excitation line of known width, I found a thermal drift uncertainty of ≈ 1 MHz. Nonlinearity in the Fabry-Pérot mechanical tracking (the experimental method used to scan the laser across the spectrum) also adds to the systematic error. By scanning the laser repeatedly over a fixed frequency range, I

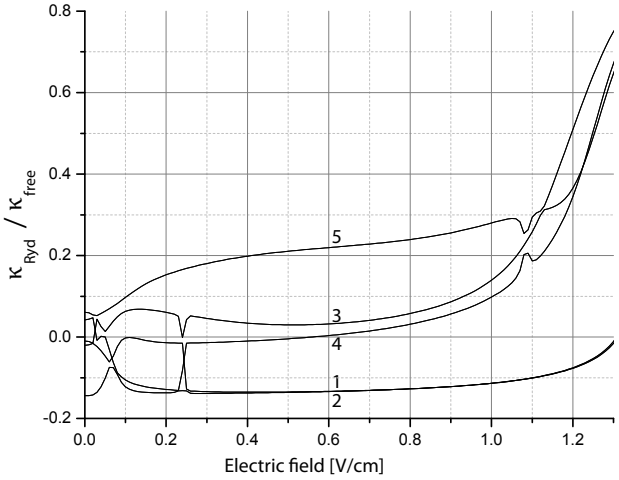

Figure 4.7: Calculated depth of the $65D$ POL potentials, $\kappa_{\rm Ryd}$, in units of the free-electron POL depth, $\kappa_{\rm free}$, for various Stark levels as a function of DC field. In the calculations, $\kappa_{\rm free} = 20$ MHz, in keeping with experimental conditions. The level labeling follows the scheme used in Figure 4.3. Negative POL depths correspond to cases in which the Rydberg-atom center-of-mass is attracted to intensity maxima in the lattice.

found a mechanical tracking uncertainty of $\lesssim 2$ MHz.

In order to obtain further insight into the angular dependence of the ponderomotive optical lattice potentials and to interpret the measured negative value of $\kappa_{\rm Ryd}$, we calculated $\kappa_{\rm Ryd}$ for $(j, m_{\rm j})$ levels of nD states as a function of DC field. The result for $65D$ is shown in Figure 4.7 (curve labels $1-5$ correspond to the ones used in Figure 4.3). For DC field values $\lesssim 0.05$ V/cm in Figure 4.7, the fine structure is dominant and the DC field provides a small perturbation. For DC field values $\gtrsim 0.1$ V/cm in Figure 4.7, the DC field effects dominate the fine structure; however, the DC field is still weak enough to largely avoid mixing of the D states with neighboring P and F states. Between the fine-structure- and the electric-field-dominant regimes, the angular wavefunctions rearrange, causing a reshuffling of the curves around 0.07 V/cm in Figure 4.7. The structures in the curves near 0.25 V/cm and 1.1 V/cm are due to crossings of Stark states in the electric-field-dominant regime. In the experiment, the depths of the $65D$ levels are measured in an electric field of about 0.65 V/cm.

For the states with negative $\kappa_{\rm Ryd}$ in Figures 4.6 and 4.7, the extent of the Rydberg-

atom wavefunction along the lattice axis approximately equals the lattice period. While the center-of-mass of the atom is located at an intensity maximum, the lobes of the electronic probability distribution are located at adjacent intensity minima, where they experience a minimal ponderomotive energy. The Rydberg center-of-mass is attracted to the lattice intensity maximum located between the wavefunction lobes. This is a unique case, as for most levels the Rydberg center-of-mass is attracted to intensity minima in the lattice. In this special case, the minima of the adiabatic Rydberg-atom trapping potential are co-located with the minima of the ground-state potential. I refer to this case throughout this thesis as a "flipped" potential (see illustration in Figure 5.5). Flipped potentials are desirable for certain applications because they allow for straightforward preparation of trapped Rydberg atoms from red-detuned optical traps for ground-state atoms.

4.4 Conclusion

I have provided an experimental demonstration of the angular dependence of the ponderomotive optical lattice potentials for Rydberg atoms. Lattice depths for (j, m_{j}) sublevels of $nD_{5/2}$ states were measured and found to vary substantially in magnitude. I have also demonstrated that certain aspect ratios of atom size to lattice period result in Rydberg lattice potential depths that are sign-matched with the ground-state potential depths. Thus, the potentials of the ponderomotive optical lattice may be tailored to a wide extent, in both magnitude and sign, to meet the specific requirements of an application. In future work, one may prepare highly elongated Stark states in the optical lattice using larger DC fields. Such states have essentially one-dimensional atomic wavefunctions oriented in the direction of the transverse DC field, leading to very deep trapping potentials. Since they also have large permanent electric dipole moments, such a system could provide a platform to study strong interactions and many-body effects in systems of optically trapped Rydberg atoms.

While the ponderomotive optical lattice for Rydberg atoms presents the attractive feature that the trapping potentials may be tuned by choice of Rydberg state, photoionization of the Rydberg atoms by the intense trapping light may be a limiting factor for applications. It is therefore necessary to have a thorough understanding of the photoionization process and its associated rates. In the next chapter, I provide an experimental study of the photoionization process as a function of position within the volume of a Rydberg atom. While the tendency of a Rydberg atom to photoionize close to the nucleus has been an assumption underlying Rydberg-atom experiments for decades, I provide the first experimental investigation of this tendency. Since the wavelength of the photoionizing light field in the experiments is on the same order as the size of the Rydberg atom (an apparent violation of the electric dipole approximation, which is typically made when $\lambda >> r$), these experiments also represent a study of fundamental light-matter interactions in a limiting case.

CHAPTER V

Photoionization of Rydberg Atoms in Optical Lattices

When electromagnetic radiation induces atomic transitions, the size of the atom is usually much smaller than the wavelength of the radiation, allowing the spatial variation of the radiation field's phase to be neglected in the description of transition rates. This approximation, known as the electric dipole approximation, is made by setting e^{ikx} to 1 in the transition-rate calculations (which are described in detail in Chapter VI). The electric dipole approximation is central to perturbative atomic photoionization studies at low intensity [45]. To understand the approximation's boundaries, it is important to explore cases in which one might expect it to break down. In the extreme case of soft x-rays interacting with ground-state atoms (wavelength $\sim 10^{-8}$ m and atom size $\sim 10^{-10}$ m), experiments have demonstrated non-dipole photoemission patterns [78].

A complementary extreme case occurs in the interaction of Rydberg atoms with light fields (atom size $\sim$ wavelength $\sim 10^{-6}$ m). Despite the apparent violation of the dipole approximation in this case, photoionization rates agree with calculated rates based on the approximation. For example, measured photoionization rates for various $nD_{5/2}$ states of Cs Rydberg atoms in an approximately homogeneous 1064 nm field are in agreement with calculations that make the approximation [79]. To reconcile

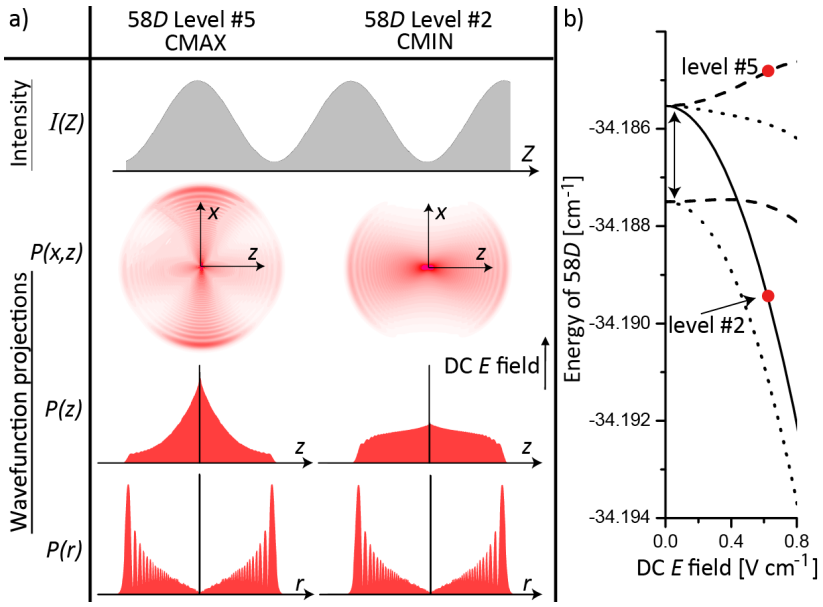

Figure 5.1: $58D$ states in an optical lattice and DC electric field. a) The lattice intensity, $I(Z)$, and projections of the electron probability density in the (xz)-plane, the z-coordinate, and the radial r-coordinate. Lowercase letters are relative coordinates of the Rydberg electron; uppercase letters are center-of-mass coordinates. Atoms prepared with initial condition CMAX (CMIN) have center-of-mass positions located near intensity maxima (minima). b) Stark energy level diagram. The fine structure splitting at zero electric field (double-headed arrow) is 60 MHz. Electric fields and energies for the projections are indicated by circles. Solid line: $|m_j| = 5/2$. Dotted lines: $|m_j| = 3/2$. Dashed lines: $|m_j| = 1/2$.

this apparent inconsistency, one may argue that the photoionization process occurs close to the nucleus in the atom [80–82]. This argument has been utilized in Rydberg-atom wavepacket experiments to probe the probability of the wavepacket return to the nucleus [83, 84]. However, the argument has never been directly verified with a photoionization probe that has sub-atomic spatial resolution. Yet, a complete understanding of the photoionization process is a prerequisite to the studies involving Rydberg atoms in optical fields mentioned in Section 1.3.

In this chapter, I investigate the photoionization process as a function of position within the volume of a Rydberg atom. I employ ^{85}Rb Rydberg nD levels in the one-dimensional optical lattice of wavelength 1064 nm. Laser beam intensities are on the order of 10^6 W/cm^2, which is low enough that higher-order effects such as

above-threshold ionization do not occur, and photoionization rates scale proportionally to intensity. The extent of the Rydberg electronic wavefunction approximately equals the lattice period, which results in maximal intensity contrast of the light field within the volume of the atom. Figure 5.1(a) illustrates the relation between the wavefunctions and the optical lattice for two of the states that I examine. The lattice intensity maxima are placed either near the atom's center or within the main lobes of the electronic probability distribution. The measured photoionization rates under these contrasting conditions indicate whether it is the light-field intensity near the center of the atom or within the lobes of the electronic probability distribution that matters in the photoionization process. While intuition might suggest that photoionization occurs where the probability of finding the electron is greatest, I demonstrate in this chapter that the process in fact happens near the nucleus. The lattice therefore acts as a microscope with sub-atomic resolution in these experiments, allowing me to study where the photoionization process occurs inside the atom.

5.1 Experimental setup

In the experiment, ground-state atoms in the optical lattice are transferred to Rydberg states with principal quantum numbers $45 \leq n \leq 65$ (the levels used are given in Table 5.1 along with the level's identifiers). The Rydberg atoms are prepared in the lattice with initial center-of-mass positions either near intensity maxima, which I refer to as initial condition CMAX, or near intensity minima, referred to as initial condition CMIN. For condition CMAX, the electronic probability distributions are predominately peaked near intensity minima, whereas for condition CMIN, they predominately peak near intensity maxima. A comparison of photoionization for these two conditions reveals whether it is the light-field intensity near the atom's nucleus or within the lobes of the electronic probability distribution that determines the photoionization rates.

Table 5.1: Measured levels and corresponding identifiers.

Level	#	Label
$45D_{5/2}$ $\lvert m_j\rvert$=1/2	5	A
$50D_{5/2}$ $\lvert m_j\rvert$=1/2	5	B
$58D_{5/2}$ $\lvert m_j\rvert$=1/2	5	C
$65D_{5/2}$ $\lvert m_j\rvert$=1/2	5	D
$50D_{5/2}$ $\lvert m_j\rvert$=5/2	2	E
$58D_{5/2}$ $\lvert m_j\rvert$=5/2	2	F
$65D_{5/2}$ $\lvert m_j\rvert$=5/2	2	G

To prepare the initial Rydberg-atom center-of-mass positions near either intensity maxima or minima in the lattice, I use an electro-optic modulator to apply a controllable phase shift to the lattice's return beam immediately following Rydberg excitation (as described in Section 3.2 and Reference [66]). Ground-state atoms in the lattice are collected at intensity maxima, since the lattice light is red-detuned relative to the $5S \rightarrow 5P$ transition of Rb. Therefore, with no phase shift applied after excitation to Rydberg states, the Rydberg-atom center-of-mass positions are initially located near intensity maxima (CMAX). With a π phase shift applied to the return beam, the Rydberg-atom center-of-mass positions are prepared near intensity minima in the lattice (CMIN).

To establish well-defined electronic probability distributions in the optical lattice with which to probe the photoionization behavior, I apply a DC electric field (see Figure 5.1), oriented transverse to the lattice axis. The Stark effect lifts the degeneracy of the $|m_j|$-sublevels of the Rydberg nD states. As shown in Figure 5.1(b), the frequency of the excitation lasers is chosen to excite the Rydberg levels #2 or #5 within the Stark nD manifolds. I choose these levels because their electronic probability distributions with respect to the lattice are quite different, to test whether such differences influence the photoionization behavior. In Figure 5.1(a), I display projections of the electron density, $P(x, z)$ and $P(z)$, as well as the radial probability distribution, $P(r)$, where x, z, and r are relative coordinates of the Rydberg electron.

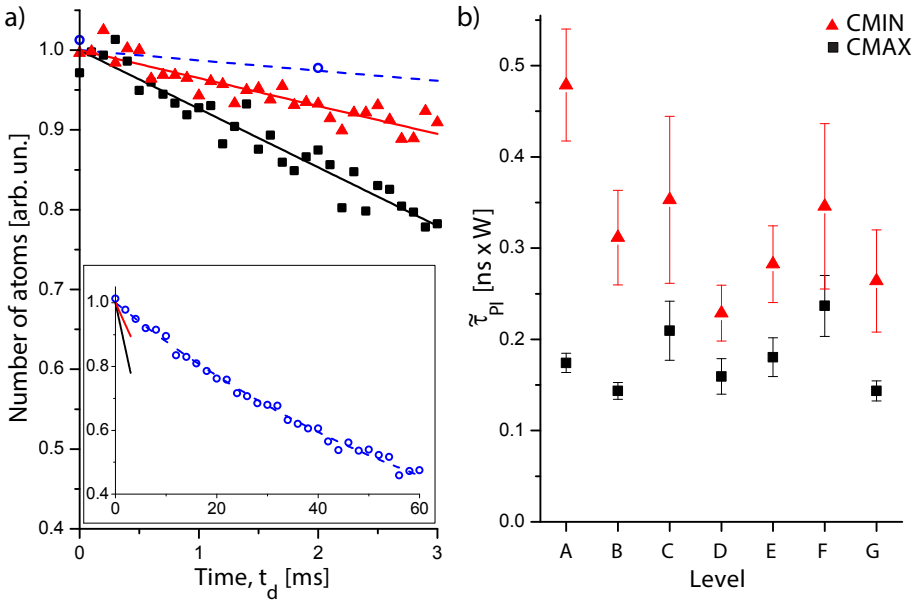

Figure 5.2: Photoionization of Rydberg atoms in an optical lattice. a) Example of measured atom number vs. time for $45D$ level #5. Decay rates are determined from fits. Solid symbols and linear fits: Lattice present; atom center-of-mass positions with initial conditions CMAX (squares) and CMIN (triangles). Hollow circles and dashed exponential fit: Without lattice. b) Normalized photoionization lifetimes for CMAX (squares) and CMIN (triangles). Level labels explained in Table 5.1. The lifetimes are an average of 1000 (levels A, B, E), 1250 (D, F), and 1750 (C, G) measurements. Error bars represent the standard error of the mean, s.e.m.

In the experiment, I aim to demonstrate whether the photoionization rate is dependent on the overlap $\int P(z)I(z+Z)dz$ of the electron with the lattice intensity I, or whether it only depends on the intensity at the center-of-mass location Z and the probability of finding the electron close to the nucleus [that is, within a small central region of $P(r)$].

5.2 Photoionization measurement procedure

I determine the photoionization rate (γ_{PI}) of a Rydberg level from measurements of its decay rate within the lattice (which yields the sum of radiative, blackbody, and photoionization decay rates, $\gamma_{\mathrm{rad}}+\gamma_{\mathrm{bb}}+\gamma_{\mathrm{PI}}$) and without the lattice (which yields $\gamma_{\mathrm{rad}}+\gamma_{\mathrm{bb}}$). By subtracting the lattice-free decay rate from that within the lattice, I

Table 5.2: Photoionization lifetime measurement conditions and results. The first five columns indicate the the level, the power of the ingoing lattice beam (P_{lat}), the DC electric field value, the modulation depth of the lattice trapping potential V_{ad}, and whether the potential is flipped or non-flipped [see Figure 5.5(a)]. The τ_{PI} and τ_{o} columns give the measured photoionization and lattice-free lifetimes, respectively. Errors, s.e.m.

Level label	P_{lat} (W)	E field (V/cm)	Depth (MHz)	Flipped or non-flipped	τ_{PI} (μs) CMAX	τ_{PI} (μs) CMIN	τ_{o} (μs)
A	0.88	2.3	11.8	NF	16.5±1.0	45.3±5.8	76.9±1.2
B	0.88	1.4	9.4	NF	18.8±1.2	40.8±6.8	127.2±3.8
C	0.88	0.65	5.7	NF	43.3±6.7	73.0±19	213.3±3.9
D	1.10	0.40	4.6	NF	37.5±4.2	53.6±6.6	251.1±5.5
E	0.88	1.4	3.8	NF	23.6±2.8	37.0±5.5	111.8±1.7
F	0.88	0.65	-1.1	FL	49.0±6.9	71.4±19	185.8±6.1
G	1.10	0.40	-3.1	FL	33.6±2.3	61.9±12	228±6.9

obtain a measurement of γ_{PI}. I measure a level's decay rate by recording the number of Rydberg atoms as a function of t_{d}, the delay time between the end of the excitation pulse and detection. The number of Rydberg atoms excited per cycle is only 1-2, ensuring that interactions and collisions between Rydberg atoms have no role.

To determine the lattice-free decay rate of a level, the number of atoms is measured for $0 \leq t_{\mathrm{d}} \leq 60$ μs ($n = 45$) and $0 \leq t_{\mathrm{d}} \leq 150$ μs ($n = 50$, 58, and 65). The data are fit to an exponential; the fit yields the lattice-free decay rate $(\gamma_{\mathrm{rad}} + \gamma_{\mathrm{bb}}) := 1/\tau_{\mathrm{o}}$. An example of lattice-free decay data is shown in Figure 5.2(a) (hollow circles). The measured values of τ_{o}, found in Table 5.2, are consistent with our calculations for a 77 K environment (my setup) and with values found elsewhere [59, 74].

To determine decay rates within the lattice, the number of atoms is measured for $0 \leq t_{\mathrm{d}} \leq 3$ μs. I limit t_{d} to ≤ 3 μs so that the atoms spend a large fraction of the atom-field interaction time near the intensity maxima or minima where they are initially prepared (the oscillation period of the atoms in the lattice is ~ 5 μs). I fit the measured number of atoms as a function of t_{d} to a line. The slope of the line divided by its y-intercept approximates the decay rate $\gamma_{\mathrm{rad}}+\gamma_{\mathrm{bb}}+\gamma_{\mathrm{PI}}$, averaged over the 3 μs. An example of decay data within the lattice is shown in Figure 5.2(a) for

both initial conditions CMAX (squares) and CMIN (triangles).

The final measurement results of the photoionization lifetime $\tau_{\mathrm{PI}} = 1/\gamma_{\mathrm{PI}}$ for all levels are found in Figure 5.2(b) and Table 5.2. The results shown in Figure 5.2(b) are normalized by the overall (n^{*3}/I_1)-scaling [85] of τ_{PI} with ingoing beam intensity I_1 and effective principal quantum number n^* ($n^* = n - \delta$ where $\delta = 1.35$ for nD states of Rb, see Section 1.2.2 and Reference [27]). The normalized lifetimes are denoted by $\widetilde{\tau}_{\mathrm{PI}}$. For each level, $\widetilde{\tau}_{\mathrm{PI}}$ is shorter for atom center-of-mass positions with initial condition CMAX than for initial condition CMIN, regardless of the Rydberg electron's probability distribution. This is true even for cases in which the main lobes of the electronic wavefunction and the atomic nucleus are separated by about half the lattice period (1064 nm/4), a situation that maximizes the intensity contrast within the atom. This situation occurs when the atomic radius, $r \approx 2n^2$, approximately equals 1064 nm/4, corresponding to $n \sim 50$ (where most of the data is taken). Thus, a qualitative analysis of the data already demonstrates that the photoionization process depends more on the light-field intensity near the nucleus of the atom than on that within the main lobes of the electronic probability distribution.

The error bars for each $\widetilde{\tau}_{\mathrm{PI}}$ in Figure 5.2(b) reflect statistical uncertainties and follow from standard error propagation and fit-parameter uncertainties returned by the fitting program (OriginPro 8). Systematic errors in the $\widetilde{\tau}_{\mathrm{PI}}$ arise mainly from lattice intensity variations, originating from the lattice laser itself or from deviations in alignment of the Rydberg excitation lasers with the lattice focal spot. Based on measurement procedures used for verifying the lattice depth (described in Section 2.3), I determine that the relative range of the lattice intensity variation is $\leq 8\%$. The effect of a reduction in lattice intensity is to move the measurements of $\widetilde{\tau}_{\mathrm{PI}}$ for both initial conditions CMAX and CMIN to higher values.

5.3 Model of photoionization

To analyze the data quantitatively, we compute atomic trajectories from the lattice trapping potentials and simultaneously simulate the photoionization-induced decay with position-dependent γ_{PI}. The photoionization-induced decay is simulated in two ways, chosen to reveal where the photoionization process occurs in the atom. In the first way, we employ γ_{PI} calculated in the electric dipole approximation, $\gamma_{\mathrm{PI}} = \frac{I(Z)}{\hbar\omega}\sigma_{\mathrm{PI}}$, where $I(Z)$ is the lattice light intensity at the atomic nucleus and σ_{PI} is the photoionization cross section [45]

$$\sigma_{\mathrm{PI}} = \frac{\pi e^2 \omega}{\epsilon_{\mathrm{o}} c} |M_{\mathrm{r}}|^2 \left(\frac{a_{\mathrm{o}}^2}{27.2 \text{ eV}} \right). \tag{5.1}$$

M_{r} represents the matrix elements describing the coupling of the initial Stark level to the continuum. In Equation 5.1, the matrix elements $M_{\mathrm{r}} = \langle f|x|i\rangle$ are in atomic units, with the free wavefunctions normalized in unit energy, and are evaluated for $|i\rangle$ being the #2 or #5 Stark states. We sum σ_{PI} over all allowed continuum states $|f\rangle = |\epsilon', l', m_{\mathrm{j}}', j'\rangle$. In the second way, we calculate γ_{PI} using a comparison model in which $\gamma_{\mathrm{PI}} \propto \int P(z) I(z+Z) dz$. This comparison model is what would be expected if the photoionization process were most likely to happen where the electron is most likely to be found. The decay rate in the comparison model is normalized such that the two models have the same photoionization rate when averaged over one lattice period. The decay rate in the comparison model is dominated by the light intensity in the regions where the electron probability distribution is greatest, while in the model based on Equation 5.1, it is determined by the intensity at the nucleus.

In Figure 5.3, the ratios of τ_{PI} for initial condition CMIN to those for CMAX are shown for the measurement results as well as the simulation results based on the two models of photoionization. In the simulations, we use an initial atomic temperature of 150 μK (Doppler cooling limit for Rb) and the beam powers and focal diameters

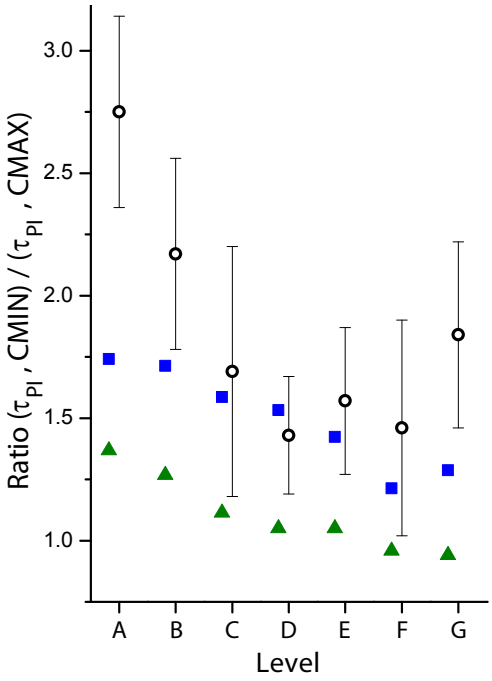

Figure 5.3: Ratios of photoionization lifetimes for initial condition CMIN to those with initial condition CMAX. Circles: Experimental. Error bars, s.e.m. Squares: Calculated, using Equation 5.1. Triangles: Calculated, using comparison model.

employed in the experiment. There are no other free parameters in the simulations. For a lattice with perfect contrast and for atoms frozen in place at either intensity maxima or minima, the ratio of τ_{PI} for initial condition CMIN to that for CMAX would be infinity. Based on the actual contrast between intensity maxima and minima in our lattice (see Section 2.3), the maximum possible ratio that one could observe for atoms frozen in place would be about 5. Any motion of the atoms in the lattice or variations in their initial positions away from the intensity maxima or minima will further reduce the experimentally observed ratio.

Comparing the simulation results for the two models of photoionization to the measurement results in Figure 5.3, good agreement is observed between the measured ratios (circles) and the model based on Equation 5.1 (squares), which clearly gives the better account of the data than the comparison model (triangles). Quantitatively, the average deviation of the measured ratios from the calculated ratios using

Equation 5.1 is 0.11, while the average deviation from the comparison model is 0.26. We note that the disparities between the simulation results based on Equation 5.1 and the experimental data for levels A, B, and G can be resolved by assuming a lower atom temperature (which generally increases the contrast between τ_{PI} for CMIN and CMAX). There is evidence elsewhere that optical dipole traps can lead to sub-Doppler atomic temperatures [67, 68]. Systematic errors resulting from lattice intensity variations have essentially no effect on the ratios. With the overall good agreement between the measurement results and the model based on Equation 5.1, we confirm that the photoionization process occurs close to the nucleus in the atom.

Classically, the photoionization process occurs close to the nucleus because the Rydberg electron is able to exchange energy with the light field efficiently when it is undergoing maximal Coulomb acceleration at the inner turning point of its classical orbit. In contrast, when the Rydberg electron is far away from the nucleus, it behaves like a free electron, oscillating in a quiver motion at the frequency of the laser light while not exchanging energy with the light field. However, close to the nucleus, the Rydberg electron is strongly accelerated by the Coulomb field, and the electron is able to exchange energy with the light field by an amount proportional to its Coulomb acceleration squared [86].

From a quantum mechanical point of view, the photoionization process occurs close to the nucleus since the matrix element accumulates its value within a small volume near the nucleus. In Figure 5.4(a), we show how the calculated matrix element builds up as a function of cutoff radius for the dipole-allowed transition from $|n = 60, \ell = 2, m = 0\rangle$ to the continuum state $|\epsilon', \ell' = 3, m' = 0\rangle$ as well as for the strongest dipole-violating transition from $|n = 60, \ell = 2, m = 0\rangle$ to $|\epsilon', \ell' = 4, m' = 1\rangle$. In the calculation, we use the formulation for the matrix elements $M_{\mathrm{p}} = -\frac{1}{\omega}\langle \epsilon', \ell', m' | e^{ikx} \frac{\partial}{\partial z} | n, \ell, m \rangle$, which does not include the electric dipole approximation, the light propagation is along x, and the light polarization along z.

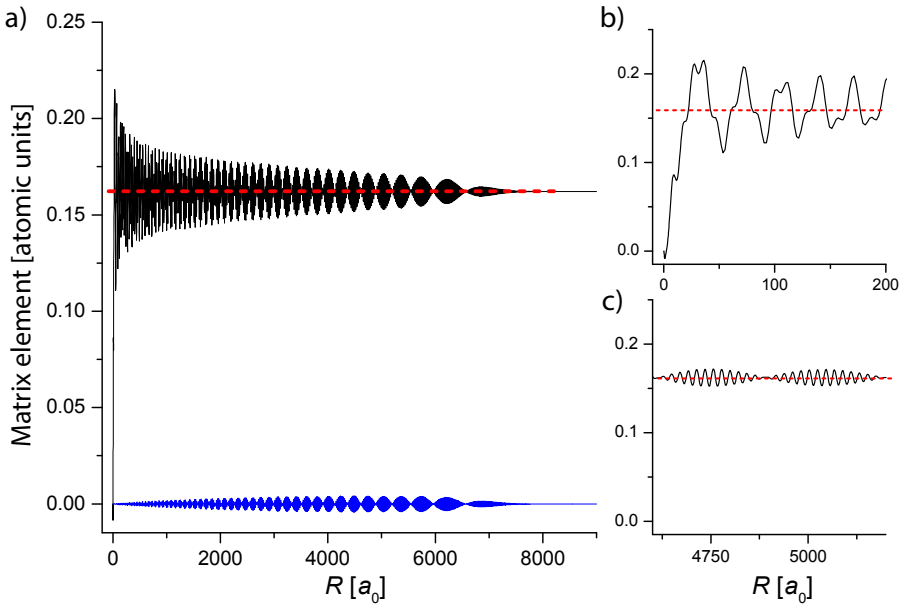

Figure 5.4: Accumulation of the photoionization matrix element. a) The value of the matrix element as a function of cutoff radius R in the radial integration for transitions from $|n = 60, \ell = 2, m = 0\rangle$ to $|\epsilon', \ell' = 3, m' = 0\rangle$ (dipole-allowed, top) and to $|\epsilon', \ell' = 4, m' = 1\rangle$ (dipole-violating, bottom). The field has a wavelength of 1064 nm ($\omega = 0.0428$ atomic units). The matrix element for the dipole-violating transition is essentially zero. b), c) The matrix element for the dipole-allowed transition accumulates to its asymptotic value (red dashed line) within a radius of $\sim 50\ a_{\mathrm{o}}$ (b). The oscillations further out do not result in any additional accumulation (c).

For the dipole-allowed transition in Figure 5.4, the matrix element accumulates its value within a radius of about 50 a_o from the nucleus, as highlighted in Figure 5.4(b), and then oscillates about its asymptotic value, a finding in accordance with calculations performed elsewhere [81]. There are two oscillation periods for radii larger than 50 a_o, highlighted in Figure 5.4(c). The longer period is the deBroglie wavelength of the bound-state wavefunction (within its classically allowed regime), while the shorter period is that of the continuum state. The matrix element does not accumulate further for $r \gtrsim 50\ a_o$ due to the large difference in the wavelengths of the bound and free states in this regime, leading to near-perfect cancellation in that integration domain. The radiative interaction is effectively confined to the region $r \lesssim 50\ a_o$, where the deBroglie wavelengths are quite similar. Since the region with $r \lesssim 50\ a_o$ is much smaller than the wavelength of the light, the dipole approximation is retroactively validated (in Equation 5.1). It is therefore the light-field intensity at the nucleus of the atom that must be used in the calculation of the photoionization rates.

The matrix element for the dipole-violating transition of Figure 5.4(a) does not accumulate to any appreciable value in the domain $r \lesssim 50\ a_o$ and undergoes some oscillation about its near-zero asymptotic value in the domain $r \gtrsim 50\ a_o$. The photoionization probability for the dipole-violating case in Figure 5.4(a) is only about 10^{-6} times the dipole-allowed photoionization probability. Hence, the dipole approximation is very well satisfied. A more detailed calculation of photoionization matrix elements and a study of the role of the electric dipole approximation is found in Chapter VI.

5.4 Atomic trajectories in the lattice

I now adopt the fact that photoionization occurs near the nucleus and consider the Rydberg-atom trajectories in the lattice to explain several other trends in the data of Figure 5.2(b) and Figure 5.3. During the 3 μs atom-field interaction time,

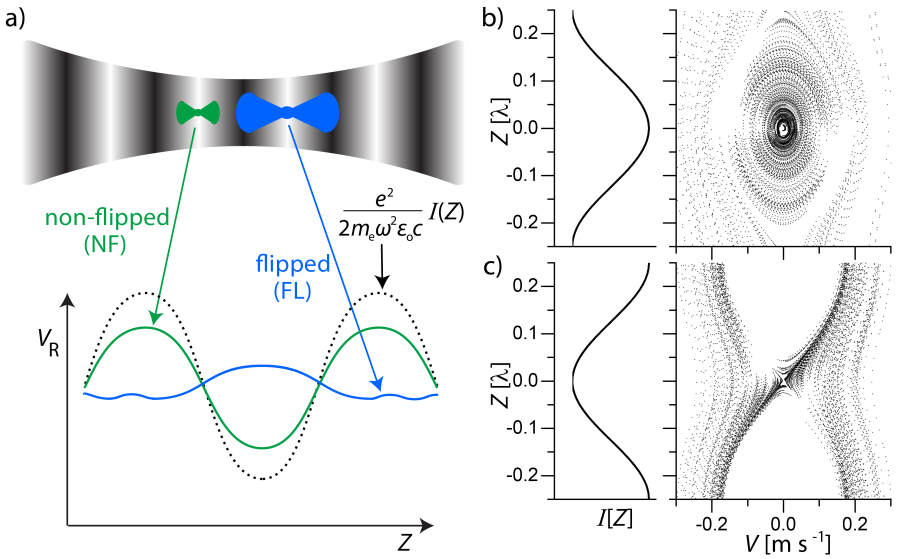

Figure 5.5: Rydberg-atom trapping potentials and trajectories in an optical lattice. a) Qualitative illustration of typical trapping potentials V_{ad} (bottom) for the Rydberg wavefunctions (top) in the optical lattice (top, white indicates high intensity and black low intensity; bottom, intensity $I(Z)$ is proportional to dotted line). Usually, potential maxima are co-located with intensity maxima (green). For wavefunctions with spatial extents in the Z direction slightly larger than the lattice period, potential maxima are "flipped" (blue). b), c) Simulated phase space diagrams (position Z vs. velocity V) for the lattice-induced motion of level G atoms (which have flipped trapping potentials), with initial conditions CMAX (b) and CMIN (c), and corresponding $I(Z)$.

the atoms move away from their initial positions on trajectories governed by the lattice adiabatic potentials $V_{\rm ad}(Z) = \frac{e^2}{2m_{\rm e}\omega^2\epsilon_{\rm o}c}\int dz\, P(z)I(z+Z)$ (see Section 1.3.2 and Reference [73]). Since the electron density $P(z)$ acts as a weighting factor, wavefunctions with larger spatial extents in the z direction usually result in more averaging and hence in shallower adiabatic potentials $V_{\rm ad}(Z)$ in the lattice. For the same n, level #2 atoms have larger spatial extents in z than level #5 atoms, generally resulting in shallower $V_{\rm ad}(Z)$; this is illustrated for the case of $50D$ in Figure 6.4(a). For most levels, the $V_{\rm ad}(Z)$ maxima coincide with lattice intensity maxima [non-flipped "NF" case in Figure 5.5(a)]. However, for ratios of atom size to lattice period near 1, the $V_{\rm ad}(Z)$ maxima coincide with lattice intensity minima [flipped "FL" case in Figure 5.5(a), also discussed in Section 4.3 and Reference [87]]. As shown in Table 5.2, the modulation depth of the $V_{\rm ad}(Z)$ generally decreases from level A through G. Atomic motion in shallower $V_{\rm ad}(Z)$ cause $\tau_{\rm PI}$ for CMIN and for CMAX to approach each other. Consequently, there is a general drop in the ratios of Figure 5.3 from A to G.

The atomic trajectories in the lattice fall into four cases: atoms prepared with initial condition CMAX or CMIN, in either NF or FL potentials. In the CMAX/NF case [Figure 5.2(b), squares, A-E], the atoms are initially prepared in regions of high intensity that are co-located with $V_{\rm ad}(Z)$ maxima. These atoms tend to quickly move through the lattice wells, sampling regions of both high and low intensity. Consequently, we expect these atoms to experience an average intensity at the nucleus given by $I(Z)$ averaged over Z (in our experiment $\sim$1.2 times the intensity of the ingoing lattice beam, independent of the level). The $\widetilde{\tau}_{\rm PI}$-values in this case are therefore expected to be approximately the same for all tested levels, which is observed in Figure 5.2(b).

In the CMAX/FL case [Figure 5.2(b), squares, F and G], the atoms are initially prepared in regions of high intensity that are co-located with $V_{\rm ad}(Z)$ minima. Com-

paring the estimated initial kinetic energy of the atoms (~ 1.6 MHz) with the depth of the trapping potentials (1.1 and 3.1 MHz for F and G, respectively), I expect atoms in level G to be trapped at locations where the intensity at the atomic nucleus is high; this is illustrated in the phase space plot of Figure 5.5(b). Level G is therefore expected to have one of the shortest $\widetilde{\tau}_{\mathrm{PI}}$, which is indeed observed.

In the CMIN/NF case [Figure 5.2(b), triangles, A-E], the atoms are initially prepared in regions of low intensity that are co-located with $V_{\mathrm{ad}}(Z)$ minima. For deep NF potentials (levels A-C; fourth column in Table 5.2), the atoms are strongly confined near the intensity minima and therefore have particularly long $\widetilde{\tau}_{\mathrm{PI}}$, as observed. For shallower potentials, the atoms are less strongly confined to the intensity minima, and consequently the observed $\widetilde{\tau}_{\mathrm{PI}}$ drop somewhat. For the CMIN/FL case [Figure 5.2(b), triangles, F and G], atoms sample all regions of the lattice fairly uniformly, as seen in Figure 5.5(c), and consequently have shorter $\widetilde{\tau}_{\mathrm{PI}}$ (although still longer than in the CMAX/FL case, since for CMIN the atoms start at locations of low intensity). Deviations in the data from the general trends described above are the result of the systematic variations in day-to-day performance of the experiment discussed earlier, such as variations in lattice intensity and alignment.

5.5 Conclusion

Using a spatially-resolved light probe, I have provided direct experimental evidence that the photoionization of Rydberg atoms by light occurs close to the nucleus in the atom, a fundamental assumption underpinning Rydberg-atom experiments for decades. Photoionization rates measured for several Rydberg states depend on the light field's intensity near the center of the atom, and not on the overlap of the electronic probability distribution with the light field (the measurements are also described in Reference [88]). The measurement result that photoionization occurs near the nucleus accords with the fact that the matrix element M_{r} in Equation 5.1 accumu-

lates within a range that is small with respect to the impinging radiation. The optical lattice is an essential experimental tool in this work, as it enables spatially-resolved photoionization. The storage and manipulation of Rydberg atoms in optical traps is important in several emerging areas already discussed in Section 1.3, including the realization of exotic phases of matter [11], field sensors [15], quantum information processing [2–4], and high-precision measurements of fundamental constants [31]. In these applications, photoionization can either represent a mechanism through which Rydberg atoms are lost, or be exploited as a detection method [69, 89]. In order to gain more insight into the photoionization process for Rydberg atoms in optical fields, in the next chapter I calculate photoionization matrix elements and cross sections. To investigate the role of the electric dipole approximation in these calculations, I derive expressions both without and with the approximation. I find conditions under which the approximation is valid and when it breaks down, and I apply the results to applications of Rydberg-atom optical lattices.

CHAPTER VI

The Role of the Electric Dipole Approximation in Photoionization - A Theoretical Study

In Chapter V, I provided spatially-resolved measurements of photoionization within the volume of a Rydberg atom. Since the size of the atom in these experiments was on the same order as the wavelength of the photoionizing light field, the electric dipole approximation appeared to be invalid in this case. However, the measured photoionization rates demonstrated that the photoionization process occurred within a volume near the nucleus that was smaller than the wavelength of the light, thus revealing the underlying reason for the electric dipole approximation's validity for Rydberg atoms in optical fields. Here, in Chapter VI, I continue the study of the photoionization process for Rydberg atoms in optical fields. To gain a deeper understanding of the role of the electric dipole approximation in this process, I derive expressions for the photoionization matrix elements and photoionization rates with and without making the dipole approximation. In evaluating the expressions, I explore conditions under which the approximation breaks down. Then, I apply the results to consider photoionization effects in experiments with Rydberg-atom optical lattices.

This chapter is organized as follows. In Section 6.1, I review the interaction of an atom with an electromagnetic field and the derivation of matrix elements describing field-induced transitions between atomic states. In Section 6.2, I discuss expressions

for the photoionization matrix elements without the dipole approximation, investigating conditions when dipole transitions dominate and when dipole-violating terms become significant. I briefly describe how the usual forms of the matrix elements that invoke the dipole approximation follow from the expressions. In Section 6.3, I consider photoionization cross sections for Rydberg atoms in an optical lattice. In Section 6.4, I present results for two applications, namely photoionization of Rydberg nD states in low-intensity optical lattices, and photoionization of adiabatic Rydberg states in high-intensity optical lattices. The work presented in this chapter was a collaboration with Y.-J. Chen.

6.1 Atom-field interaction

The Hamiltonian for an N-electron atom with nuclear charge Z is given by

$$H = \sum_{i=1}^{N} \left(\frac{\mathbf{p}_i^2}{2m_\mathrm{e}} - \frac{Ze^2}{4\pi\epsilon_0 r_i} \right) + \frac{1}{4\pi\epsilon_0} \sum_{i>j=1}^{N} \frac{e^2}{|\mathbf{r}_i - \mathbf{r}_j|}. \tag{6.1}$$

The terms inside of the brackets are the kinetic and potential energy of each electron in the Coulomb field of the nucleus. The term outside of the brackets describes the electrostatic repulsion between pairs of electrons. The interaction of the atom with an electromagnetic field can be taken into account by replacing $\mathbf{p}_i$ with $\mathbf{p}_i + |e|\mathbf{A}(\mathbf{r}_i, t)$, where $\mathbf{A}(\mathbf{r}_i, t)$ is the vector potential. The resulting interaction Hamiltonian that is added to Equation 6.1 is

$$H_\mathrm{int} = \sum_{i=1}^{N} \{ \frac{|e|}{2m_\mathrm{e}} [\mathbf{p}_i \cdot \mathbf{A}(\mathbf{r}_i) + \mathbf{A}(\mathbf{r}_i) \cdot \mathbf{p}_i] + \frac{e^2}{2m_\mathrm{e}} \mathbf{A}^2(\mathbf{r}_i) \}.$$

The $\mathbf{A}^2(\mathbf{r}_i)$ term describes two-photon processes. This term gives rise to the ponderomotive potential that is responsible for the trapping of Rydberg atoms in an optical lattice, as explained in Section 1.3.2. For photoionization in plane-wave, low-intensity fields, the $\mathbf{A}^2(\mathbf{r}_i)$ term can be neglected. In the Coulomb gauge, $\nabla \cdot \mathbf{A} = 0$,

and $\mathbf{p}_i$ and $\mathbf{A}(\mathbf{r}_i)$ commute[1]. The interaction Hamiltonian can then be simplified to

$$H_{\text{int}} = \sum_i \left(\frac{|e|}{m_{\text{e}}} \mathbf{A}(\mathbf{r}_i) \cdot \mathbf{p}_i \right).$$

We consider a Rydberg atom with one active electron. In this case, the summation over i in H_{int} may be dropped, and the position and momentum operators $\mathbf{r}$ and $\mathbf{p}$ are for the Rydberg electron. For a source-free radiation field, the electric field and vector potential are related by $\mathbf{E} = -(\partial \mathbf{A}/\partial t)$ [46]. We first assume that the field is a plane wave propagating in the x-direction and polarized in the z-direction[2]. Therefore, $\mathbf{A}(\mathbf{r}, t) = \mathbf{E}/(i\omega) = \frac{E_0}{2i\omega} \hat{\mathbf{z}} e^{i(kx - \omega t)} + cc$, where E_0 is the field amplitude, ω the angular frequency, k the wavenumber, and $\hat{\mathbf{z}}$ the unit vector in the z-direction.

According to Fermi's golden rule, which is given in full in Section 6.3.1, atomic transitions are determined by $|\langle f|H_{\text{int}}|i\rangle|^2$ [45, 90], where $|i\rangle$ and $|f\rangle$ are the initial and final states with wavefunctions ψ_i and ψ_f. Using the expression above for $\mathbf{A}$ and writing the matrix element $\langle f|H_{\text{int}}|i\rangle$ in position representation, $\langle f|H_{\text{int}}|i\rangle$ becomes in the rotating frame

$$\langle f|H_{\text{int}}|i\rangle = -\frac{e\hbar E_0}{2m_{\text{e}}\omega} \int \psi_f^* e^{ikx} \frac{\partial}{\partial z} \psi_i \, d^3r, \tag{6.2}$$

where the dipole approximation has not been made. (The approximation amounts to ignoring the phase variation of the field over the volume of the atom, which is done by setting $e^{ikx} = 1$.)

To express the matrix elements $M = \int \psi_f^* e^{ikx} \frac{\partial}{\partial z} \psi_i \, d^3r$ in a form that can be evaluated numerically, we use spherical coordinates. The wavefunctions are given by $\psi_{n,\ell,m}(r, \theta, \phi) = R_{n,\ell}(r) Y_\ell^m(\theta, \phi)$ [90], and $R_{n,\ell} = u_{n,\ell}(r)/r$. The quantum numbers

[1]Since $\mathbf{p} = -i\hbar\nabla$, if $\nabla \cdot \mathbf{A} = 0$, then $\mathbf{p}_i$ and $\mathbf{A}(\mathbf{r}_i)$ commute.

[2]We assume that the field is propagating in the x-direction and polarized in the z-direction for the convenience of calculating $\frac{\partial}{\partial z}\psi_i$ in Equation 6.2, which is done in spherical coordinates. In Section 6.4, we will switch to assuming a field that is propagating in the z-direction and polarized in the x-direction for the convenience of making the z-direction our quantization axis for m.

(n, ℓ, m) and (n', ℓ', m') denote those of the initial and final states, respectively. The radial wavefunctions are calculated according to Reference [1]. The Jacobi-Anger relation,

$$e^{iacos\phi} = \sum_{\widetilde{m}=-\infty}^{\infty} i^{\widetilde{m}} J_{\widetilde{m}}(a) e^{i\widetilde{m}\phi},$$

expresses e^{ikx} in terms of an azimuthal Fourier series. The matrix elements then become

$$\begin{aligned} M = i^{m'-m} \frac{1}{2} \sqrt{\frac{2\ell'+1}{2\ell+1} \frac{(\ell'-m')!}{(\ell'+m')!} \frac{(\ell-m)!}{(\ell+m)!}} \Bigg\{ \int u_{n',\ell'}(r) [u'_{n,\ell}(r) - \frac{u_{n,\ell}(r)}{r}(\ell+1)] \\ \times \left[\int J_{m'-m}(kr\sin\theta) P_{\ell'}^{m'}(\cos\theta) P_{\ell+1}^{m}(\cos\theta)(\ell-m+1)\sin\theta \, d\theta \right] dr \\ + \int u_{n',\ell'}(r) [u'_{n,\ell}(r) + \frac{u_{n,\ell}(r)}{r}\ell] \\ \times \left[\int J_{m'-m}(kr\sin\theta) P_{\ell'}^{m'}(\cos\theta) P_{\ell-1}^{m}(\cos\theta)(\ell+m)\ \sin\theta \, d\theta \right] dr \Bigg\}. \quad (6.3) \end{aligned}$$

The matrix elements given in Equation 6.3 describe atomic transitions between bound states (and do not include the dipole approximation). For transitions from bound to free states (photoionization), the radial wavefunction $u_{n',\ell'}$ in Equation 6.3 is replaced by a free radial wavefunction $u_{\epsilon',\ell'}$. We use free wavefunctions that are normalized in energy, $\int u_{\epsilon',\ell'}(r) u_{\epsilon,\ell'}(r)\, dr = \delta(\epsilon - \epsilon')$.

6.2 General behavior of the matrix elements

6.2.1 Results without invoking the electric dipole approximation

Equation 6.3 yields a selection rule for allowed transitions that arises from the three functions within the θ integrals (one Bessel function and two associated Legendre functions). Since the θ integrals are performed from 0 to π, we consider the

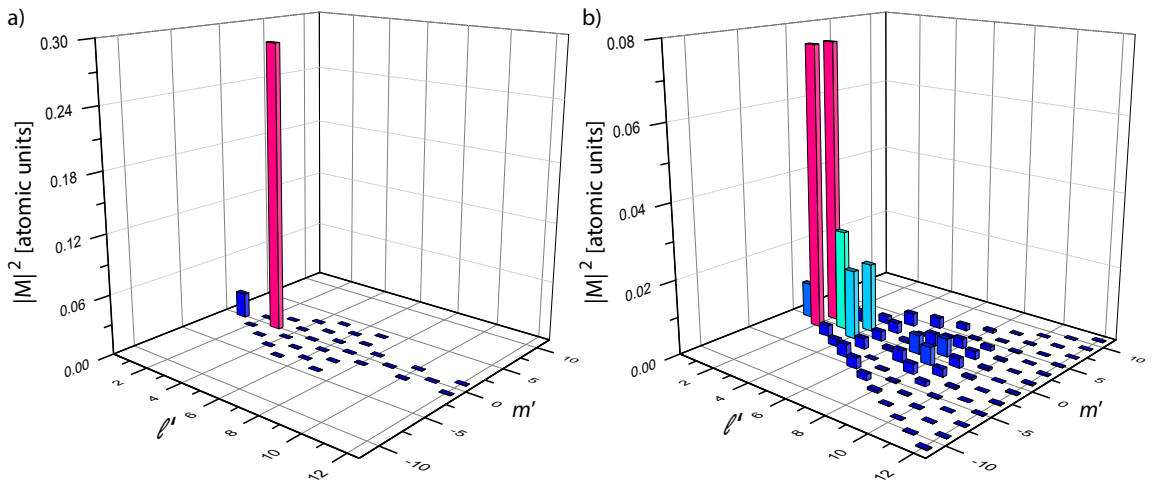

Figure 6.1: a) Matrix elements squared for photoionization with π-polarized light from $|n = 15, \ell = 2, m = 0\rangle$ to the continuum states $|\epsilon' = 0.0830, \ell', m'\rangle$ for Rb, plotted for various values of final ℓ' and m'. The wavelength of the field is 532 nm. The only transitions with matrix elements of non-negligible amplitude are the dipole-allowed transitions. b) Matrix elements squared for the same transitions as in (a), but with the wavelength of the field artificially reduced by a factor of $\kappa = 1000$. Dipole-violating transitions now have matrix elements with large values.

parity behavior of the three functions about $\pi/2$ to determine the selection rule. The Bessel function terms in Equation 6.3 are always even. The associated Legendre functions $P_\ell^m(x)$ are even if the sum $\ell + m$ is even. Therefore, $\ell + m + \ell' + m' + 1$ and $\ell + m + \ell' + m' - 1$ must be even for the first and second θ integrals, respectively, to yield a non-zero result for the integrals. These conditions are fulfilled simultaneously. Therefore, the selection rule is that $\ell + m + \ell' + m' + 1$ must be even.

In the limit $\lambda >> r$ (as when the electric dipole approximation is valid), there are additional selection rules in Equation 6.3. The argument of the Bessel functions, $kr \sin\theta$, tends toward zero, and Bessel functions higher than J_0 can be neglected. Therefore, from the orthogonality of the Legendre polynomials, we find the familiar dipole selection rules $m' - m = \Delta m = 0$ (for z-polarized light) and $\Delta\ell = \pm 1$.

To demonstrate the typical photoionization behavior of Rydberg atoms in light fields, we calculate matrix elements following from Equation 6.3 for a rubidium Rydberg atom interacting with a field of wavelength 532 nm. In Figure 6.1(a), we dis-

play the calculated matrix elements squared, $|M|^2$, for transitions from $|n = 15, \ell = 2, m = 0\rangle$ to the continuum states $|\epsilon' = 0.0830, \ell', m'\rangle$. The only transitions that have non-negligible $|M|^2$ values are the dipole-allowed transitions, for which $\Delta m = 0$ and $\Delta\ell = \pm 1$. The strongest dipole-violating transitions have $|M|^2$ values that are smaller than those of the dipole-allowed transitions by a factor of 10^{-5}.

To explore conditions under which dipole-violating transitions become important, we increase the wavenumber k inside the Bessel function argument in Equation 6.3 by an artificial factor κ, while holding everything else fixed (including the continuum state). While this does not correspond to a physically realizable situation, it allows us to explore where the unexpected validity of the dipole approximation arises when performing the integrations shown in Equation 6.3. By increasing the argument of the Bessel function by κ, we artificially increase the effect of higher order Bessel functions in the resulting matrix elements[3]. Calculated matrix elements for transitions from $|n = 15, \ell = 2, m = 0\rangle$ to the continuum states $|\epsilon' = 0.0830, \ell', m'\rangle$ are shown in Figure 6.1(b) for $\kappa = 1000$. Dipole-violating transitions now have matrix elements with significant values. In Figure 6.1(b), the most significant dipole-violating transitions (to $|\epsilon' = 0.0830, \ell' = 2, m' = \pm 1\rangle$) have $|M|^2$ values that are about a factor of 5 larger than the strongest dipole-allowed transition. In both Figure 6.1(a) and (b), we observe the "checker board" pattern of transitions allowed by the selection rule that $\ell + m + \ell' + m' + 1$ must be even.

It is evident from the results presented in Figure 6.1 that the dipole approximation is valid for Rydberg atoms in optical fields, despite the size of the atom being on the same order as the wavelength of the light. To illustrate why the dipole approximation holds in this seemingly unlikely case, we plot in Figure 6.2 the value of the matrix

[3]If we were to change the wavelength of the light in the calculation, we would also change the continuum state $u_{\epsilon',\ell'}$ in Equation 6.3. In order to avoid complicating matters by changing numerous things at once, we add the factor κ to the argument of the Bessel function. As discussed above, this allows us to effectively investigate the effect of the higher order Bessel functions in the resulting matrix elements while holding everything else fixed.

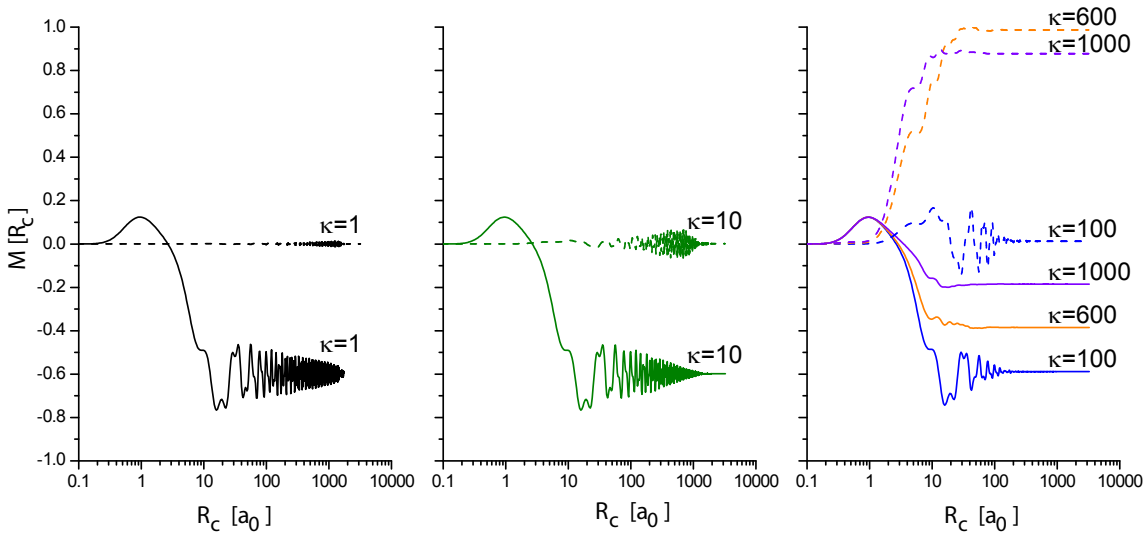

Figure 6.2: Value of the matrix element, M, for the dipole-allowed transition (solid lines) from $|n = 30, \ell = 2, m = 0\rangle$ to the continuum state $|\epsilon' = 0.0850, \ell' = 3, m' = 0\rangle$ and for the dipole-violating transition (dashed lines) from $|n = 30, \ell = 2, m = 0\rangle$ to the continuum state $|\epsilon' = 0.0850, \ell' = 2, m' = 1\rangle$ as a function of cutoff radius, R_c, for Rb. The wavelength of the field is 532 nm. The κ values, explained in the text, are indicated.

element for the transition from $|n = 30, \ell = 2, m = 0\rangle$ to $|\epsilon' = 0.0850, \ell' = 3, m' = 0\rangle$ (solid lines) as a function of cutoff radius in the radial integral. We find that for $\kappa = 1$ the matrix element accumulates within a radius of about 50 a_0 and then oscillates around its asymptotic value at larger radii. This is a similar result to that shown in Figure 5.4. Since the value of the matrix element is essentially unchanged outside of the small volume with $r \lesssim 50\ a_0$, the effective range of the radiative interaction is confined to this small region around the nucleus. The Rydberg atom tends to photoionize close to the nucleus. This finding is in accordance with calculations performed elsewhere [81]. Since the matrix element accumulates to its asymptotic value in a volume that is much smaller than the physical wavelength of the light, the phase variation of the field in the outer regions $r \gtrsim 50\ a_0$ is irrelevant because there is no more accumulation for M. The electric dipole approximation therefore applies in the physical case (i.e. for $\kappa = 1$).

We further illustrate in Figure 6.2 how the build-up of the matrix element for

the transition from $|n = 30, \ell = 2, m = 0\rangle$ to $|\epsilon' = 0.0850, \ell' = 3, m' = 0\rangle$ (solid lines) changes when the wavelength of the light is effectively reduced (by increasing κ). We plot the value of the matrix element as a function of integration cutoff radius for $\kappa = 10, 100, 600,$ and 1000. For $\kappa \lesssim 100$, deviations from the $\kappa = 1$ result are very small. Major deviations are observed for $\kappa = 600$ and 1000, corresponding to effective wavelengths of about 20 a_0. In this short-wavelength case, the phase of the field does vary substantially over the volume with $r \lesssim 50\ a_0$, within which the matrix element accumulates to its asymptotic value. Under such conditions, the electric dipole approximation breaks down. This is verified by Figure 6.1(b), where dipole-violating matrix elements have values larger than dipole-allowed values. It is also verified by the dashed lines in Figure 6.2, which show the value of the matrix element for the strongest dipole-violating transition from $|n = 30, \ell = 2, m = 0\rangle$ to $|\epsilon' = 0.0850, \ell' = 2, m' = 1\rangle$. For $\kappa \lesssim 100$, the dipole-violating matrix elements accumulate to values near zero, while for $\kappa = 600$ and 1000, they reach large asymptotic values.

6.2.2 Results with the electric dipole approximation

In Section 6.2.1, we have established that the electric dipole approximation applies to Rydberg atoms in optical fields, with $|M|^2$ values of the strongest non-dipole terms at a typical relative level of one part in 10^5. In the electric dipole approximation, Equation 6.2 for $\langle f|H_{\rm int}|i\rangle$ can be simplified by setting $e^{ikx} = 1$. In terms of the momentum operator $\mathbf{p} = \frac{\hbar}{i}\nabla$, $\langle f|H_{\rm int}|i\rangle$ then becomes

$$\langle f|H_{\rm int}|i\rangle = -\frac{ieE_0}{2m_{\rm e}\omega}\hat{\mathbf{n}} \cdot \int \psi_f^* \, \frac{\hbar}{i}\nabla \, \psi_i \, d^3r,$$

where the unit vector $\hat{\mathbf{n}}$ now refers to a general linear-polarization direction. The matrix elements for z-polarized light, $M = \int \psi_f^* \, \frac{\hbar}{i}\frac{\partial}{\partial z} \, \psi_i \, d^3r$, are given by

$$M = \sqrt{\frac{(\ell_> + m)(\ell_> - m)}{(2\ell_> + 1)(2\ell_> - 1)}} \times \begin{cases} \int u_{n',\ell'}(r)[u'_{n,\ell}(r) - \frac{u_{n,\ell}(r)}{r}\ell_>]\, dr & \text{if } \ell_> = \ell' = \ell + 1 \\ \int u_{n',\ell'}(r)[u'_{n,\ell}(r) + \frac{u_{n,\ell}(r)}{r}\ell_>]\, dr & \text{if } \ell_> = \ell = \ell' + 1 \end{cases}. \tag{6.4}$$

When the matrix elements are expressed in terms of the momentum operator, as shown above, this is known as the "velocity" form of the matrix elements. In the dipole approximation, the matrix elements can also be expressed in other forms using commutation relations between operators. The relation $[\mathbf{r}, H_0] = \frac{i\hbar}{m}\mathbf{p}$, which follows from the fundamental position-momentum uncertainty relation, allows the matrix elements to be written in terms of the position operator. This form of the matrix elements is known as the "length" form. The validity of this commutation relation, and hence of the length form of the matrix elements, depends on the potential in the field-free atomic Hamiltonian, H_0, being a function only of position, not momentum. In the length form, $\langle f|H_{\text{int}}|i\rangle$ becomes

$$\langle f|H_{\text{int}}|i\rangle = \frac{eE_0}{2}\hat{\mathbf{n}} \cdot \int \psi_f^*\, \mathbf{r}\, \psi_i\, d^3r, \tag{6.5}$$

where the matrix elements $M_{\text{r}} = \hat{\mathbf{n}} \cdot \int \psi_f^*\, \mathbf{r}\, \psi_i\, d^3r$ are given in Reference [90] (equation 60.7 and following).

Alternatively, the matrix elements may be expressed in the "acceleration" form. In this form, the commutation relation $[\mathbf{p}, H_0] = -i\hbar\nabla V$ is used to express the matrix elements in terms of $[(Z\mathbf{r})/r^3]$. The validity of this form depends on the potential in H_0 being equal to the Coulomb potential [90], clearly making this the most restrictive form. In the length, velocity, and acceleration forms, the matrix elements accumulate to their asymptotic values at large, intermediate, and small values of r, respectively (which is discussed in References [81, 90, 91]). However, no matter what the form, the value of the matrix elements builds up within a small

radius of the nucleus and undergoes oscillations about a steady-state value for larger radii (as observed in Figure 6.2).

6.3 Photoionization cross sections

For the applications that will be discussed in Section 6.4, the effect of photoionization is most conveniently accounted for using photoionization cross sections. In the present section, we provide the relevant equations that relate the computed matrix elements with the cross sections.

6.3.1 Case of a plane wave

The transition rate between atomic states is given by Fermi's golden rule, $P_{i\to f} = \frac{2\pi}{\hbar}|\langle f|H_{\rm int}|i\rangle|^2\rho(E_f)$. For photoionization, the unbound final states ψ_f are normalized per unit energy, and the density of final states $\rho(E_f)$ is equal to 1. To find the expression for the photoionization rates, we use Fermi's golden rule and the expression for $\langle f|H_{\rm int}|i\rangle$ in Equation 6.2. The photoionization rates are proportional to the intensity (even if the electric dipole approximation does not apply). The range of relevant photoionization channels (i.e. the ℓ' and m' quantum numbers of the continuum state for a given initial state; see Figure 6.1) depends on how well the electric dipole approximation is satisfied.

The photoionization cross section $\sigma_{\rm PI}$ is determined by dividing the photoionization rate by the photon flux density [field intensity over energy per photon, $I/(\hbar\omega)$]. In SI units, without the electric dipole approximation, and for linearly polarized light (polarization unit vector $\hat{\mathbf{n}}$) with wavevector $\mathbf{k}$, the photoionization cross section is

$$\sigma_{\rm PI} = \frac{\pi e^2\hbar^2}{\epsilon_0 m_{\rm e}^2\omega c}\left|\hat{\mathbf{n}}\cdot\int\psi_f^*\, e^{i\mathbf{k}\cdot\mathbf{r}}\,\nabla\psi_i\, d^3r\right|^2\left(\frac{1}{27.2\text{ eV}\times a_0^2}\right). \tag{6.6}$$

The matrix elements are computed in atomic units, and the term in brackets converts

the matrix elements to SI units. If the electric dipole approximation is made and the radial matrix elements $M_{\rm r}$ are expressed in length form, the photoionization cross section is

$$\sigma_{\rm PI} = \frac{\pi e^2 \omega}{\epsilon_0 c} \left| \hat{\mathbf{n}} \cdot \int \psi_f^* \, \mathbf{r} \, \psi_i \, d^3 r \right|^2 \left(\frac{a_0^2}{27.2 \text{ eV}} \right). \tag{6.7}$$

The photoionization cross sections depend on all initial and final state quantum numbers and on the polarization of the incident field. If the m sublevels of the initial state ψ_i are unresolved, the photoionization cross section must be averaged over m. The resulting shell-averaged photoionization cross section is given by

$$\bar{\sigma}_{\rm av} = \frac{\pi e^2 \omega}{3 \epsilon_0 c} \frac{\ell_>}{2\ell + 1} |M_{\rm r}|^2 \left(\frac{a_0^2}{27.2 \, \text{eV}} \right), \tag{6.8}$$

where $\ell_>$ is the larger of ℓ and ℓ', and $M_{\rm r}$ is the radial matrix element calculated in atomic units, $M_{\rm r} = \int u_{\epsilon',\ell'} u_{n,\ell} r \, dr$. Averaging over the initial-state m value in a polarized field yields the same result for $\bar{\sigma}_{\rm av}$ as summing over allowed transitions for a fixed initial m state in an unpolarized field.

It is convenient to calculate photoionization cross sections for m- and polarization-specific transitions using $\bar{\sigma}_{\rm av}$. For light polarized in the z-direction and $\bar{\sigma}_{\rm av}$ given by Equation 6.8, the photoionization cross section for an initial m state is given by

$$\sigma_z(m) = \frac{3}{4} \frac{(\ell_>^2 - m^2)}{(2\ell_> + 1)(2\ell_> - 1)} \frac{(2\ell + 1)}{\ell_>} \bar{\sigma}_{\rm av}. \tag{6.9}$$

In the applications discussed in Section 6.4 below, it is convenient to assume a light field that is propagating in z and polarized in x. We therefore also give the photoionization cross section for a field polarized in the x-direction (σ_x and σ_y are the same),

$$\sigma_x(m) = \frac{3}{2} \frac{(\ell'(\ell' + 1) + m^2)}{(2\ell_> + 1)(2\ell_> - 1)} \frac{(2\ell + 1)}{\ell_>} \bar{\sigma}_{\rm av}. \tag{6.10}$$

6.3.2 Case of an optical lattice

The results that we have given so far are for a plane wave. In an optical lattice, the field is composed of two counter-propagating plane waves, and the expression for the matrix elements must be modified accordingly. For the case of an optical lattice propagating along $\pm x$ and polarized along z, the electric field is

$$\mathbf{E}(x,t) = \frac{E_0}{2}\hat{\mathbf{z}}[e^{i(kx-\omega t+\alpha/2)} + e^{i(-kx-\omega t-\alpha/2)}] + cc,$$

where $\pm\alpha/2$ are the beam phases at the atom's center-of-mass location. In the rotating frame, the electric field becomes

$$\mathbf{E}(x) = \hat{\mathbf{z}}E_0 \cos(kx + \alpha/2). \tag{6.11}$$

Using the relation $\mathbf{A} = \mathbf{E}/(i\omega)$, spherical coordinates, and the Jacobi-Anger relation, the vector potential for the optical lattice is expressed

$$\mathbf{A}(r,\theta,\phi) = \hat{\mathbf{z}}\frac{E_0}{2i\omega}\sum_{m'-m=-\infty}^{\infty} i^{m'-m}J_{m'-m}(kr\,\sin\theta)e^{i(m'-m)\phi} \times \begin{cases} 2\,\cos(\alpha/2) & \text{if } m'-m \text{ is even} \\ 2i\,\sin(\alpha/2) & \text{if } m'-m \text{ is odd} \end{cases}. \tag{6.12}$$

With this expression for $\mathbf{A}$ and $m' - m = \Delta m$, the matrix elements M for an optical lattice may be obtained by multiplying those for a plane wave (Equation 6.3) by $2\,\cos(\alpha/2)$ for the Δm even terms and $2i\,\sin(\alpha/2)$ for the Δm odd terms.

Photoionization in the case of an optical lattice provides further insight into the nature of the photoionization process. When the dipole approximation holds, $\Delta m = 0$, and $|M|^2$ is proportional to $\cos^2(\alpha/2)$, as seen from Equation 6.12. In an optical lattice, the intensity at the center-of-mass position is also proportional to $\cos^2(\alpha/2)$,

which follows from Equation 6.11. Therefore, when the dipole approximation is valid, the photoionization cross sections are determined by the intensity at the exact center-of-mass location of the Rydberg atom. It is irrelevant how the field varies over the atomic diameter (which, for a Rydberg atom, is on the order of the wavelength). If the dipole approximation were not valid, Δm would take on many values, and the photoionization cross sections would contain terms that would no longer be proportional to the intensity at the center-of-mass of the Rydberg atom [as both the $\cos(\alpha/2)$ and the $\sin(\alpha/2)$ terms in Equation 6.12 would be important]. The fact that the photoionization cross section for a Rydberg atom in a strongly inhomogeneous light field only depends on the intensity at the center-of-mass location re-emphasizes the propensity of such atoms to photoionize close to the nucleus. This in turn ties into the validity of the electric dipole approximation.

6.4 Experimental applications

We now apply the equations that have been derived throughout the chapter to applications with Rydberg atoms in optical lattices. We divide the applications into two general classes: applications of low-intensity lattices and of high-intensity lattices. This thesis has dealt mainly with low-intensity lattices thus far. As discussed in Sections 1.3.2 and 4.2.2, lattice-induced shifts to the atomic energy levels in low-intensity lattices are on the order of 10 MHz, while lattice-induced state-mixing is negligible. These Rydberg-atom lattices are therefore attractive for such applications as quantum computing [30] or high-precision spectroscopy [31]. In quantum computing applications, the optical lattice would allow for sequential gate operations utilizing the same atoms in a trap that is compatible with optical lattice traps for ground-state atoms. Furthermore, in both quantum computing and high-precision spectroscopy applications, it is possible to achieve magic-wavelength traps, which would minimize trap-induced shifts on transitions of interest [33].

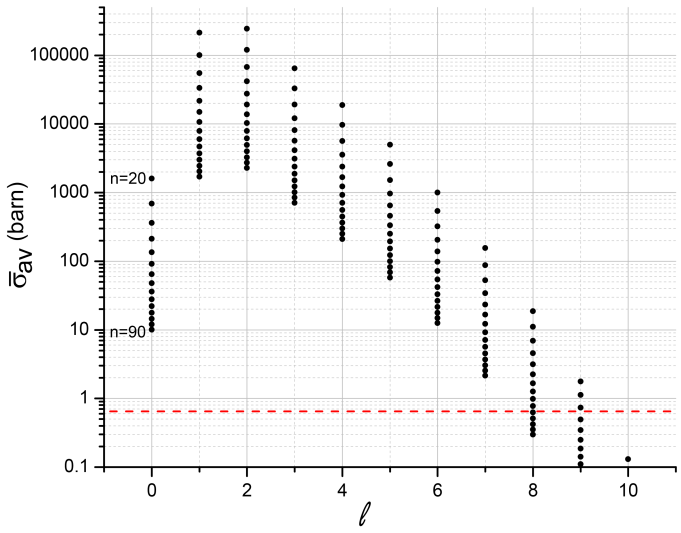

Figure 6.3: Shell-averaged photoionization cross sections for Rb Rydberg n and ℓ states in a plane-wave 1064 nm field, calculated following Equation 6.8 (1 barn $= 10^{-28}$ m^2). For each ℓ, the n values range from 20 to 90 in steps of 5. The red dashed line represents the Thomson scattering cross section (0.665 barn). (Any photoionization cross sections below this value should be replaced with the Thomson scattering cross section.)

In the case of high-intensity lattices, the ponderomotive potential is on the same order as the Kepler frequency ($\sim$ 1 GHz; see Section 1.2.1). The lattice in this case not only traps the Rydberg atoms, but also induces strong ℓ state-mixing of the levels. The resulting structure of the adiabatic potentials in the lattice is more complex than for low-intensity lattices [53]. Near the inflection points, the lattice-induced potential is approximately linear for small Rydberg atoms, resulting in a level structure that resembles the Stark effect. Near the nodes and anti-nodes, the lattice-induced potential is approximately quadratic, resulting in a level structure that resembles the diamagnetic problem. Spectroscopic studies of such novel high-intensity lattices will reveal these structures.

In both classes of applications described above, photoionization of Rydberg atoms in the lattice may be a concern. To illustrate the photoionization probability trends for different Rydberg states, Figure 6.3 shows calculated photoionization cross sections for Rb as a function of n and ℓ. The photoionization cross sections are generally

quite large for low ℓ. The S states are an exception, however. They exhibit very small photoionization cross sections due to a Cooper minimum that results from the S- and P-state quantum defects of Rb being different by almost exactly 0.5 (see Section 3.4.3 and Reference [26]). The photoionization cross sections fall off as ℓ increases and reach very small values for high-ℓ states ($\ell \gtrsim 10$). The red dashed line in Figure 6.3 indicates the Thomson scattering cross section ($\sigma = 0.665$ barn), which describes the QED effect of scattering of light from an electron [92]. A photoionization cross section (which is computed semi-classically) that is lower than the Thomson scattering cross section should be replaced with this value.

In the remainder of this chapter, we consider in Section 6.4.1 the photoionization of Rb nD states in low-intensity lattices, a case in which photoionization is easy to measure since these states have some of the highest photoionization rates (as seen in Figure 6.3). In Section 6.4.2, we consider the photoionization of the adiabatic Rb Rydberg states in high-intensity lattices. Due to state-mixing in this case, all adiabatic states contain some low-ℓ character, and consequently, it must be considered whether these states will photoionize at rates that would noticeably broaden spectroscopic structures or affect applications of such deep Rydberg-atom optical lattices. All calculations in the following sections are performed for a one-dimensional optical lattice.

6.4.1 Photoionization of nD states in low-intensity lattices

Both the adiabatic potentials and photoionization rates are generally m-dependent. In low-intensity optical lattices ($\sim 10^6$ W/cm^2), the m-dependence of the potentials and photoionization rates can be measured, for instance, as an $|m_\mathrm{j}|$-dependence of Rydberg D state lattice depths and photoionization rates (where $m_\mathrm{j} = m + m_\mathrm{s}$, with spin magnetic quantum number m_s). In the present section, we calculate adiabatic potentials and photoionization rates for $|m_\mathrm{j}|$ sublevels of nD states in a low-intensity

optical lattice, with a DC electric field applied to lift $|m_{\rm j}|$ degeneracies.

The potentials for Rydberg atoms in an optical lattice are calculated by finding and diagonalizing the Hamiltonian

$$H_{\rm lat} = H_0 + V_{\rm p}(z + Z_0) \tag{6.13}$$

as a function of the atom's center-of-mass position Z_0 in the lattice (the z represents the relative z-coordinate of the Rydberg electron). Further, $V_{\rm p}(z + Z_0) = e^2E^2(z + Z_0)/(4m_{\rm e}\omega^2)$ is the free-electron ponderomotive potential in the lattice field with position-dependent amplitude $E(z+Z_0)$ (see Section 1.3.2). The adiabatic potentials are then constructed by plotting the energy eigenvalues as a function of the position Z_0 [53]. The adiabatic potentials, $V_{\rm ad}$, for the center-of-mass motion of the Rydberg atoms in a one-dimensional lattice (propagating in z and polarized in x) are given by

$$V_{\rm ad}\left(Z_0\right) = \int d^3r\, V_{\rm p}\left(z + Z_0\right) |\psi\left(\mathbf{r}\right)|^2, \tag{6.14}$$

which is a spatial average of $V_{\rm p}$ weighted by the Rydberg wavefunction, ψ, and is discussed in Section 1.3.2. The wavefunction ψ generally is a superposition of the lattice-free atomic states due to lattice-induced state mixing. The $V_{\rm ad}$ potentials for Rydberg atoms have been investigated for low-intensity lattices in Chapter IV and Reference [41].

Examples of the adiabatic potentials $V_{\rm ad}$ for $50D$ in a lattice of depth 40 MHz are shown in Figure 6.4(a). This depth can be achieved by focusing two counter-propagating 1064 nm laser beams, each with a power of 1 W, into a confocal spot with $w_0 = 13\ \mu$m. In Figure 6.4(a), a DC electric field of strength 1 V/cm is applied in the z-direction to lift degeneracies of the $|m_{\rm j}|$ sublevels. The $50D_{3/2}$ and $50D_{5/2}$ levels split into a total of five components in the DC field, as described in Section 4.2.1. The components are labeled in Figure 6.4(a) in order of increasing energy, following

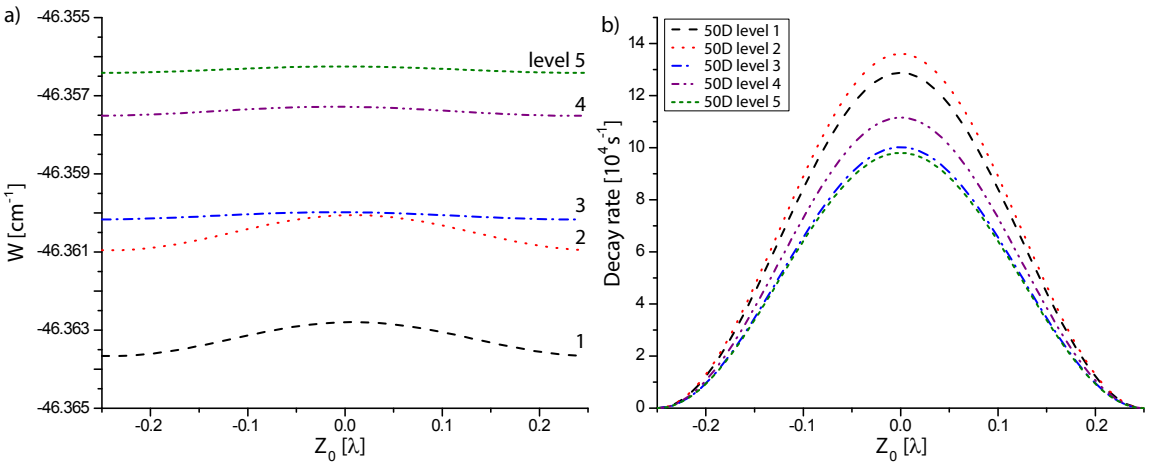

Figure 6.4: a) Adiabatic potentials in wavenumbers, W, for $50D$ of Rb in an optical lattice of depth 40 MHz and a superimposed DC electric field of 1 V/cm pointing in the lattice-beam direction. Potentials are plotted as a function of Rydberg-atom center-of-mass position in the lattice, Z_0, and are labeled in order of increasing energy in the DC field. b) Photoionization decay rates for the same levels and experimental parameters as in (a).

the convention used in Sections 4.2.1 and 5.1. In the limit of small DC field, the five components connect with the following levels: (1) $50D_{3/2}$ $|m_j|$=3/2, (2) $50D_{5/2}$ $|m_j|$=5/2, (3) $50D_{3/2}$ $|m_j|$=1/2, (4) $50D_{5/2}$ $|m_j|$=3/2, and (5) $50D_{5/2}$ $|m_j|$=1/2. The $|m_j|$-dependence of the potentials is clearly observed in Figure 6.4(a), as the modulation depth of the adiabatic potentials for the five levels varies from strongly modulated (levels 1-2) to barely modulated (levels 3-5). The five sublevels vary in modulation depth because of differences in the extent of the wavefunctions along the axis of the lattice, resulting in varying amounts of averaging in Equation 6.14 (see Section 4.1 and Reference [87]). The sublevels with wavefunctions that are extended in the direction of the lattice axis experience shallower potentials, since they average over more of the free-electron ponderomotive potential. Levels 3-5 in Figure 6.4(a) therefore have wavefunctions with larger extents in the direction of the lattice axis than levels 1-2.

To illustrate the m-dependence of the photoionization rates, we begin with a hypothetical example that exhibits an extreme difference in photoionization behavior

for the different magnetic sublevels. We consider photoionization of a P state, without fine structure. We also assume a Cooper minimum for photoionization into D states in the continuum, so that the only available photoionization channel is into S states. For a π-polarized laser field, the $\Delta m = \pm 1$ transitions are not allowed by selection rules. The only allowed photoionization channel is then $|nP, m = 0\rangle \rightarrow |\epsilon' S', m' = 0\rangle$. Therefore, for such a model atom, one magnetic substate would photoionize at high rates, while the other two ($|nP, m = \pm 1\rangle$) are protected from photoionization by angular momentum selection rules.

To quantitatively include the effect of photoionization in the same optical lattice as in Figure 6.4(a), we add imaginary contributions to the energy eigenvalues of the basis states that account for the photoionization-induced decay. The resultant effective Hamiltonian is

$$H(Z_0) = H_{\mathrm{lat}}(Z_0) + \sum_{n\ell j m_{\mathrm{j}}} |n\ell j m_{\mathrm{j}}\rangle\langle n\ell j m_{\mathrm{j}}| \left(-i \frac{\hbar \Gamma_{n\ell j m_{\mathrm{j}}}(Z_0)}{2} \right), \tag{6.15}$$

with H_{lat} defined in Equation 6.13. The second term above introduces the imaginary contributions to the diagonal terms of the Hamiltonian. The decay rates, $\Gamma_{n\ell j m_{\mathrm{j}}}(Z_0)$, are related to photoionization cross sections and the lattice intensity $I(Z_0)$ via

$$\Gamma_{n\ell j m_{\mathrm{j}}}(Z_0) = \sigma_{n\ell j m_{\mathrm{j}}} \frac{I(Z_0)}{\hbar\omega} = \frac{2c\epsilon_0 m_{\mathrm{e}} \omega}{e^2 \hbar} \sigma_{n\ell j m_{\mathrm{j}}} V_{\mathrm{p}}(Z_0).$$

The decay rates are proportional to the position-dependent ponderomotive potential, $V_{\mathrm{p}}(Z_0)$, defined above. The decay rates are also proportional to the photoionization cross section $\sigma_{n\ell j m_{\mathrm{j}}}$, which for x-polarized light is a weighted average of $\sigma_x(n, \ell, m = m_{\mathrm{j}} + 1/2)$ and $\sigma_x(n, \ell, m = m_{\mathrm{j}} - 1/2)$ from Equation 6.10 using the Clebsh-Gordon coefficients as the weighting factors (and we sum over $\ell' = \ell - 1$ and $\ell' = \ell + 1$). Note that the decay rates are determined by the intensity at the center-of-mass location of the Rydberg atom, Z_0. To obtain the photoionization rates of the adiabatic

Rydberg states in the optical lattice, the imaginary parts of the eigenvalues found after diagonalization are multiplied with $2/\hbar$.

In Figure 6.4(b), we plot the photoionization rates $\Gamma(Z_0)$ in the lattice for the $|m_\mathrm{j}|$ sublevels of $50D$. For $Z_0 = 0$, the photoionization rates are maximal for the five sublevels, since the atomic center-of-mass is located at an intensity maximum. The peak values of $\Gamma(Z_0)$ vary for the five levels and translate into photoionization lifetimes of about a few μs, which would be readily observed in the lifetimes of the levels (radiative lifetime for $50D$ is ≈ 100 μs at 77 K). The effect of photoionization-induced line broadening would still be negligible, as it is only a few tenths of the linewidths of typical excitation lasers (~ 1 MHz). For $Z_0 = \pm\lambda/4$ in Figure 6.4(b), the photoionization rates for all sublevels vanish, since the atomic center-of-mass is located at intensity minima. The $|m_\mathrm{j}|$-dependence of the photoionization rates is clearly visible, as the peak photoionization rates vary over a relative range of 16%. This dependence is less significant than the variations seen for the adiabatic-potential depths. This is because the adiabatic potentials depend on the long-range structure of the wavefunctions, while the photoionization rates depend only on the intensity near the center-of-mass of the atom. The shape of the wavefunction therefore has a larger effect on the adiabatic potentials than on the photoionization rates.

6.4.2 Photoionization of adiabatic states in high-intensity lattices

In high-intensity optical lattices ($\sim 10^8$ W/cm^2), with depths on the order of a few GHz, the lattice mixes states of different ℓ (and, under absence of cylindrical symmetry, also m). The adiabatic states in the lattice are now linear superpositions of a wide range of angular momentum states. Lattice-induced mixing of a large number of nearly degenerate states gives rise to a rich structure of adiabatic potentials in the lattice. This structure is illustrated in Figure 6.5, where the adiabatic potentials for $n = 50$, $m_\mathrm{j} = 1/2$ (including fine structure in the calculation; for a detailed description

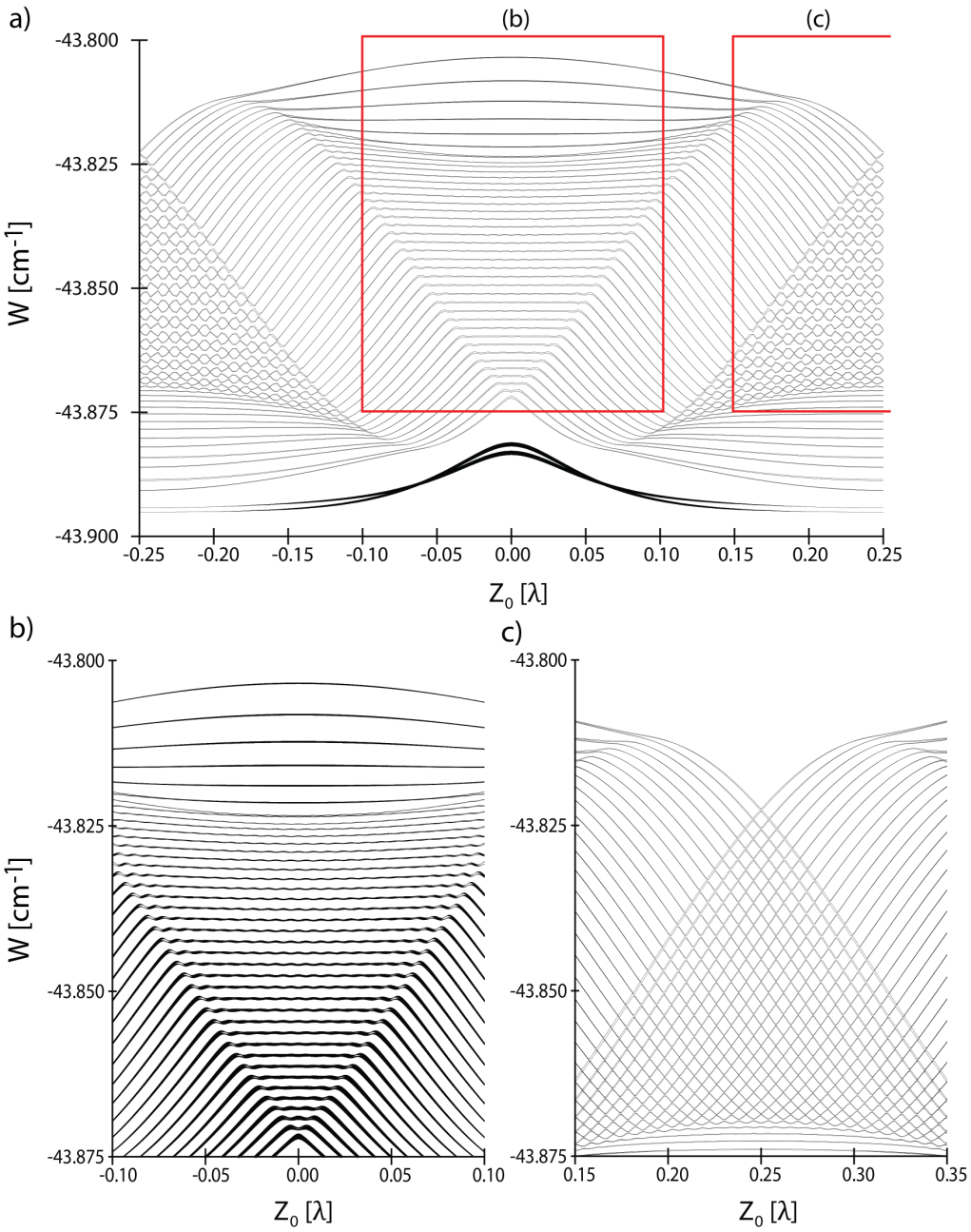

Figure 6.5: Adiabatic potentials in wavenumbers, W, for $n = 50$, $m_j = 1/2$ of Rb in an optical lattice with depth of 3 GHz. The boxed regions in (a) correspond to the regions in panels (b) and (c). The widths of the energy levels equals the FWHM of the photoionization-induced linewidth multiplied with an enhancement factor of 100 (a) and 1000 (b,c). (The enhancement factor is necessary for the photoionization-induced level width to become visible.)

of the calculation, see Reference [53]) are plotted as a function of atomic center-of-mass position in the lattice. The lattice primarily mixes states of zero quantum defect;

the thickest curves in Figure 6.5(a) are F states, which are depressed in energy due to their quantum defect and consequently are less mixed with the hydrogenic states. Near the inflection points of the lattice [$Z_0 = \pm\lambda/8$ in Figure 6.5(a)], the straight, non-intersecting structure of the adiabatic potentials resembles the level structure obtained with the DC Stark effect. Since the free-electron ponderomotive potential, V_p, in these regions is linear, the analogy to the DC Stark effect (which also involves a linear perturbation potential) is expected. The lattice is therefore interpreted as providing an effective electric field in these regions. Near the nodes and anti-nodes of the lattice [$Z_0 = 0, \pm\lambda/4$ in Figure 6.5(a)], the levels resemble the rotational and vibrational energy level series in the diamagnetic problem [52, 93–95]. In both the diamagnetic problem and in the lattice potential near the nodes and anti-nodes, the perturbation is quadratic. The lattice can therefore be interpreted as providing an effective magnetic field in these regions. The structure of the adiabatic potentials in high-intensity lattices and its interpretation is described in detail in Reference [53].

Due to lattice-induced state-mixing, even the hydrogen-like states acquire some lower-ℓ character and may consequently photoionize. In spectroscopic studies of the adiabatic potentials, it must be considered whether photoionization-induced line broadening will hinder resolution of the adiabatic potentials. To investigate this, we calculate photoionization rates using the same procedure as in Section 6.4.1 for the adiabatic states in a lattice of depth 3 GHz. This depth can be achieved by focusing two counter-propagating 1064 nm laser beams, each with a power of 200 W, into a confocal spot with $w_0 = 21$ μm. Such a lattice could be prepared, for instance, by using a concentric field enhancement cavity, with the Rydberg atoms at the center. In Figure 6.5, the plotted width of the adiabatic potentials equals the FWHM of the photoionization-induced linewidth of the potentials[4], multiplied by an enhancement factor. For the level widths to become visible in Figure 6.5, the enhancement factor

[4]It is important not to neglect the factor of 2π when converting linewidth to decay rate. The linewidth of the potentials equals 2π times the decay rate.

is 100 in Figure 6.5(a) and 1000 in Figure 6.5(b), (c).

Maximum photoionization-induced decay rates in Figure 6.5 are about 1.6×10^6 s^{-1} for the F-like states at $Z_0 = 0$, where the lattice intensity is maximal. For the hydrogen-like states within the range of Figure 6.5(b), which is near an intensity maximum, the maximum decay rates are about 10^5 s^{-1}. For the hydrogen-like states within the range of Figure 6.5(c), which is near an intensity minimum, the maximum decay rates are about 2×10^4 s^{-1}. Since the radiative decay rates of Rydberg levels around $n = 50$ are on the order of 10^4 s^{-1}, the effect of photoionization-induced decay on the lifetimes of the states would be discernable in measurements of atom number as a function of time (such as those in Section 5.2). However, photoionization-induced line broadening would be about 10^{-2} times smaller than anticipated widths of the adiabatic potentials in spectroscopic studies (determined by the linewidths of the excitation lasers and the decay rate of any intermediate states used in the laser excitation). Therefore, photoionization-induced line-broadening will not play a role in these spectroscopic studies.

In the center regions of the spectrum near $Z_0 = \pm\lambda/4$ in Figure 6.5(a) and (c), the structure of the adiabatic potentials takes the form of a series of small wells with a periodicity of 10 nm. We emphasize that this periodicity of 10 nm is achieved using a laser wavelength of 1064 nm; it is therefore much smaller than the $\lambda/2$ limit that usually sets the lower bound on the periodicity of optical lattices. For the intensities used in Figure 6.5(c), the small wells have a depth of 10-100 MHz, sufficient to support about 10 quantum levels (for a Rb atom). By decreasing the intensity of the lattice, the depth of the wells could be made shallow enough that tunneling becomes important. These wells may therefore become attractive for quantum state manipulation and control experiments.

6.5 Conclusion

We have analyzed matrix elements describing the photoionization of Rydberg atoms by optical fields, and we have discussed implications of our calculations for experiments with Rydberg atoms in optical lattices. The matrix elements derived for Rb Rydberg states in a field of wavelength 532 nm without making the electric dipole approximation accumulate within a small volume near the nucleus with $r \lesssim 50\ a_0$. For that case, non-dipole terms have matrix-element-squared values that are 10^{-5} times smaller than the dipole-allowed values. The electric dipole approximation is therefore well satisfied. A noticeable breakdown of the approximation is expected for wavelengths $\lesssim 10$ nm. Applications of Rydberg atoms in optical fields include low- and high-intensity lattices. For low-intensity lattices, photoionization will have a strong, m-dependent effect on the lifetimes of the Rydberg states. For high-intensity lattices, photoionization will have no effect on the linewidths of the states but will be discernable in the states' lifetimes.

The thorough characterization of the photoionization process given in this chapter and Chapter V provides a solid, fundamental understanding of the role of photoionization in experiments with Rydberg atoms in optical fields. This understanding, together with the ability to trap the atoms efficiently as in Chapter III and to tune the trapping potentials by choice of Rydberg state as in Chapter IV, makes the Rydberg-atom optical lattice ready for applications. In the next chapter, I describe some future directions for this Rydberg-atom trap, including work already underway towards using the ponderomotive optical lattice in microwave spectroscopy applications.

CHAPTER VII

Future Directions

In this thesis, I have developed a novel Rydberg-atom trap that uses standing-wave optical fields to confine the Rydberg atoms. Optical traps for Rydberg atoms, in contrast to those for ground-state atoms, utilize the ponderomotive potential acting on the quasi-free Rydberg electron to trap the atoms. My accomplishments in the realization and characterization of this trap include a demonstration of ^{85}Rb Rydberg-atom trapping in a 1064 nm optical lattice with 90% efficiency. Since the Rydberg atoms were initially prepared near lattice potential maxima, the high trapping efficiency was only possible with a lattice inversion applied immediately after Rydberg-atom preparation, placing potential minima at the location of the atoms. I have also investigated the trapping potentials experienced by Rydberg atoms in the lattice and their dependence on the angular portion of the Rydberg wavefunction. The modulation depth of the potentials was demonstrated, by choice of Rydberg state, to be tunable over a wide range, including a sign change such that the Rydberg- and ground-state potentials were sign-matched. Further, I have characterized the process by which the Rydberg atoms are ionized by the relatively intense lattice light. Since the lattice intensity was maximally inhomogeneous within the volume of the Rydberg atom, it served as a spatially-resolving light probe to study where the photoionization process occurred. Photoionization was found to occur close to the nucleus. In the theoretical

description of photoionization, I have shown that photoionization happens close to the nucleus because the matrix elements describing this process accumulate within a small radius of the nucleus, and I have determined conditions under which we may expect this localization of photoionization to break down. Finally, I have applied this understanding of photoionization to consider applications of Rydberg atoms in optical lattices. Therefore, through this work, the ponderomotive optical lattice for Rydberg atoms has progressed from being essentially a proposal to being a well developed and understood trap, ready for employment in the applications discussed in Section 1.3. In the remainder of this chapter, I outline some future directions for the Rydberg-atom optical lattice system, with an emphasis on applications in microwave spectroscopy.

7.1 Three-dimensional trapping

In experiments presented earlier in this thesis, Rydberg atoms were trapped in an optical lattice with 90% efficiency in the longitudinal z-direction of the lattice. Since the lattice was one-dimensional, the atoms left the lattice in the transverse direction within tens of μs. A future direction for the work presented in this thesis is therefore to achieve three-dimensional confinement of Rydberg atoms, which would enable long Rydberg-atom trapping times. Long trapping times are necessary for applications such as high-precision spectroscopy, which depends on long atom-field interaction times for high levels of precision and accuracy in the measurements.

Since Rydberg atoms are, in general, attracted to intensity minima in the lattice, a three-dimensional Rydberg-atom trap requires a dark volume surrounded on all sides by light. A way to achieve such a light-field profile in the current experimental setup (i.e. in the "cryoMOT" setup) would be to adjust the spot sizes and powers of the two counter-propagating lattice beams as illustrated in Figure 7.1. One beam would have less power and would be focused more tightly, while the other would have

Figure 7.1: Laser beam diagram for a three-dimensional bottle trap for Rydberg atoms. The foci and powers of the two counter-propagating lattice beams are adjusted to achieve intensity matching on-axis, surrounded by a non-zero light field.

more power and would be focused less tightly. This would result in a region of perfect constructive and destructive interference on-axis that is surrounded on all sides by light. Such a trap profile is referred to as a "bottle trap" [73, 96].

To implement such a bottle trap with minimal changes to the existing experimental setup, one could offset the foci of the ingoing and return lattice beams to match the on-axis intensities in the two beams (for a description of the existing lattice setup and an explanation of why the lattice beams are not currently intensity-matched when their foci are overlapped, see Section 2.3). In the current setup, the maximum ingoing lattice beam power, which is denoted by P_1 and is limited by power restrictions of the optical fiber that carries the 1064 nm light to the chamber, is 1.5 W. The confocal spot of the ingoing beam (w_{01}) is 11 μm. As discussed in Section 2.3, the return beam power (P_2) is attenuated by 0.56, and the return beam focus is enlarged to a confocal spot (w_{02}) of 21 μm. For these experimental parameters, the intensity-matching condition may be calculated with the ingoing beam focus at $z + \delta$ and the return beam focus at z, where δ is the offset needed to match the on-axis intensities of the two beams.

To find the trapping potentials in a lattice with the parameters given above, I calculate the shift of the Rydberg levels in such a lattice. The shift of the Rydberg levels in units of Hz is $W = (-\frac{1}{4}\alpha_{\mathrm{R}}E^2)/h$, where E is the electric field amplitude discussed below in Equation 7.1, and α_{R} is the state-dependent polarizability of the Rydberg

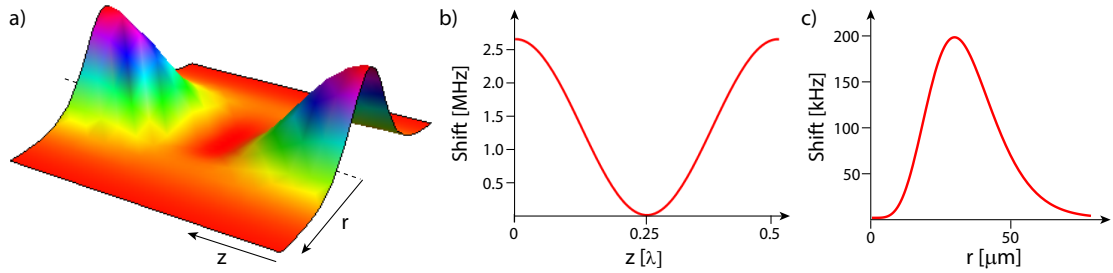

Figure 7.2: a) Calculated $45S$ trapping potential, for a configuration with a single, retroreflected $\lambda = 1064$ nm beam. The ingoing lattice beam is offset and the return beam attenuated to match intensities on-axis. b) The modulation depth of the longitudinal trapping potential is 2.7 MHz. c) The modulation depth of the transverse trapping potential is 195 kHz.

state discussed in Section 3.1. Here, I consider the case of $45S$, a relatively small state, so that the wavefunction averages over less of the free-electron ponderomotive potential (in Equation 1.6) and the trapping potentials are consequently deeper. For $45S$, the polarizability is $\alpha_{45S} = 0.706 \times \alpha_{\mathrm{p}}$, where α_{p} is the free-electron polarizability (see Section 3.1). The total electric field in the lattice, with the offset δ for the ingoing beam included, is

$$E(r,z) = \sqrt{\frac{4P_1}{\pi c \epsilon_0 w_1^2(z+\delta)}} e^{-r^2/[w_1^2(z+\delta)]} e^{ikz} + \sqrt{\frac{4P_2}{\pi c \epsilon_0 w_2^2(z)}} e^{-r^2/[w_2^2(z)]} e^{-ikz}, \qquad (7.1)$$

where k is the wavenumber, and w_1 and w_2 are the position-dependent $1/e^2$ radii of the two Gaussian beams.

A calculated trapping potential for the experimental parameters given above is shown in Figure 7.2(a), along with slices of the trapping profile along the axis of the lattice (z-direction) in Figure 7.2(b) and transverse to the axis of the lattice (radial r-direction) in Figure 7.2(c). In order to reach the deepest trap possible in the radial direction, the return beam must be attenuated further (beyond the 0.56 factor already present), to 0.2 times the power of the ingoing beam. This corresponds to an offset $\delta = 1.5$ mm. These parameters are used in Figure 7.2. While the depth of

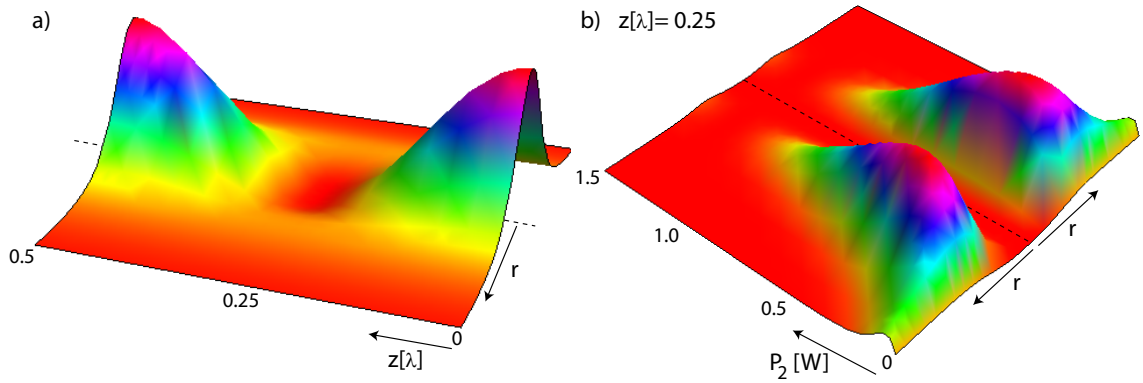

Figure 7.3: a) Calculated $45S$ trapping potential, for a configuration with two independently controllable $\lambda = 1064$ nm lattice beams. For the deepest transverse potential [as determined in (b)], one lattice beam has a power P_1 of 1.5 W and a focal spot w_{10} of 26 μm. The other lattice beam has a power P_2 of 0.3 W and a focal spot w_{20} of 11 μm. b) The transverse trapping potential at $z = 0.25\lambda$ as a function of power P_2. The deepest transverse potential is found for $P_2 = 0.3$ W to be 700 kHz [used in (a)], and the depth of the longitudinal potential in this case is 11 MHz.

the trapping potential in the z-direction is almost 3 MHz, the trapping potential in the r-direction is only about 200 kHz. This corresponds to an atomic temperature of about 20 μK, which is too cold to be easily achievable in the current experimental setup. The trapping efficiency in the radial direction would therefore be limited.

If the lattice is formed by two independently controllable, counter-propagating lattice beams instead of by retroreflection of a single beam (as in the current setup, see Section 2.3), the potential in the radial direction can become deeper. In the following calculation, the foci of the two beams are assumed to be coincident with each other. I assume a maximum power in one beam (P_1) of 1.5 W (which is the limit due to the damage threshold of the optical fibers) and a minimum focal spot (w_{20}) of 11 μm in the other beam. I then calculate the power of the second beam (P_2, which also determines the focus of the first beam, $w_{01} = w_{02}\sqrt{\frac{P_1}{P_2}}$) that is necessary to match intensities. The resulting trapping potential is shown in Figure 7.3(a), and the transverse trapping potential at $z = 0.25\lambda$ is shown in Figure 7.3(b) as a function of P_2. As seen in Figure 7.3(b), the value of P_2 that gives the deepest transverse potential is 0.3 W; the resulting transverse potential depth is 700 kHz. This trap

depth corresponds to temperatures of 67 μK. Atomic temperatures in this range have been demonstrated in the cryoMOT setup using an additional molasses cooling phase (in which the detuning of the MOT was increased and the power of the MOT reduced, see B. Knuffman's Ph.D. thesis). Note that switching off the MOT magnetic fields, which is typically done during molasses cooling, is not an option in the cryoMOT setup due to eddy currents in the system that persist for $\approx$ 50 ms (see the senior thesis work of K. Crimmins). The longitudinal potential depth in Figure 7.3(a) is 11 MHz. Therefore, it would be possible to achieve three-dimensional confinement for the Rydberg atoms using this configuration.

An alternative way to achieve a three-dimensional trap for Rydberg atoms in a different experimental setup is by inserting a concentric resonator inside the vacuum chamber. By coupling the 1064 nm lattice light into the resonator, the cavity acts as a mode filter, allowing for a near perfect mode structure and hence optical lattice. This is in contrast to the setup utilized in this thesis where the retroreflected lattice beam is attenuated and distorted by the additional components in the return beam path. By fine-tuning the alignment of the cavity, high order Laguerre- or Hermite-Gaussian modes [97] can be readily achieved, which could be used to create a light-field profile necessary for three-dimensional confinement of Rydberg atoms. The resonator also acts as a field-enhancement cavity, which would enable spectroscopic studies of the adiabatic potentials described in Section 6.4.2. Such a configuration is currently being pursued in the Raithel lab.

7.2 Amplitude-modulated ponderomotive optical lattice

A novel technique enabled by the ponderomotive optical lattice allows for a new method of performing microwave spectroscopy with Rydberg atoms. In traditional microwave spectroscopy with Rydberg atoms, transitions are driven by direct application of microwave radiation, as done in Section 3.3. However, by modulating the

amplitude of the optical lattice at the appropriate microwave frequency, transitions may be driven between two Rydberg states. This method is unique in comparison to traditional spectroscopic methods because it allows one to drive transitions between Rydberg states that bypass the usual dipole selection rules that govern spectroscopy. Further, since the amplitude-modulated light for driving the Rydberg transitions may be focused to μm-scale spot sizes, this innovative method would allow one to drive site-selective microwave transitions between Rydberg states. It would therefore combine the high spectral resolution of microwave spectroscopy with the spatial resolution of optical spectroscopy. Driving transitions between Rydberg states in this manner is ideal for performing high-precision spectroscopy to improve determinations of fundamental atomic constants (see Section 7.3 and References [27, 98]).

The origin of the transitions driven by amplitude modulation of the optical lattice is distinct from that of usual spectroscopy, in that it engages the $\mathbf{A} \cdot \mathbf{A}$ term of the atom-field interaction Hamiltonian, H_{int}, in contrast to the usual $\mathbf{p} \cdot \mathbf{A}$ term. Without the amplitude modulation of the optical lattice, the $\mathbf{A} \cdot \mathbf{A}$ term results in trapping potentials, as shown in Section 1.3.2. With the amplitude modulation, the term also drives transitions between Rydberg states. As discussed in Section 6.1, atomic transitions from an initial state $|i\rangle$ to a final state $|f\rangle$ are found by time-dependent perturbation theory to be described by Fermi's golden rule, in which the probability for a transition is given by the square of the matrix elements, $|\langle f|H_{\text{int}}|i\rangle|^2$. Rydberg states are orthogonal, and therefore in order for matrix elements for a transition to be non-zero, the operator for H_{int} must have a position dependence. The traditional method of driving atomic transitions via the $\mathbf{p} \cdot \mathbf{A}$ term of H_{int} is described in Section 6.1. For the $\mathbf{p} \cdot \mathbf{A}$ operator, the position dependence comes from the $\mathbf{p}$. In utilizing the $\mathbf{A} \cdot \mathbf{A}$ term to drive Rydberg transitions in an optical lattice, the time dependence of the amplitude modulation allows us to apply time-dependent perturbation theory, and the spatial dependence required for the matrix elements to be

non-zero arises from the interference pattern in the lattice intensity.

The Hamiltonian for the Rydberg electron in an amplitude-modulated optical lattice, which has wavenumber k, is propagating along z, and is modulated in intensity at angular frequency Ω, is given in atomic units by

$$H = -\frac{1}{r} + V_{\mathrm{c}}(r) + (A + B\cos(\Omega t))[1 + \cos(2k(z - Z_0))]. \tag{7.2}$$

Here, the first term is the Coulomb potential, and V_{c} is a short-range core potential that takes into account the quantum defects (see Section 1.2.2). The last term in Equation 7.2 represents the ponderomotive lattice potential that both varies in space and is modulated in amplitude, where z is the relative coordinate of the Rydberg electron, Z_0 is the center-of-mass coordinate of the atom, $2A$ is the time-averaged depth of the lattice, and $2B$ is the amplitude of the modulation. The lattice perturbation described by this term varies over the size of the Rydberg atom. Therefore, when the spatial part of the perturbation is expanded, the higher order terms have significant values and are able to drive transitions for a wide range of $\Delta\ell$ values. A full derivation of the matrix elements is found in Reference [31].

In collaboration with K. Moore, I have made progress towards implementing this technique for driving Rydberg transitions in the laboratory. Transitions between Rydberg states are in the tens of GHz regime, and therefore in order to realize this novel method for driving Rydberg transitions, we must modulate the lattice intensity at these frequencies. To accomplish the intensity modulation, we use a high-frequency electro-optic modulator (EOM) of the Mach-Zehnder type (EOSpace, Inc., $\Omega \lesssim 2\pi \times 40$ GHz). Since the high-frequency EOM can only tolerate low laser powers ($\lesssim 200$ mW), technical challenges are associated with this experiment. High lattice power (≈ 1 W) is needed to achieve a potential depth that confines the atoms, so as to eliminate motion of the atoms through the lattice. This is important because Rabi frequencies of the transitions driven by the amplitude-modulated lattice have

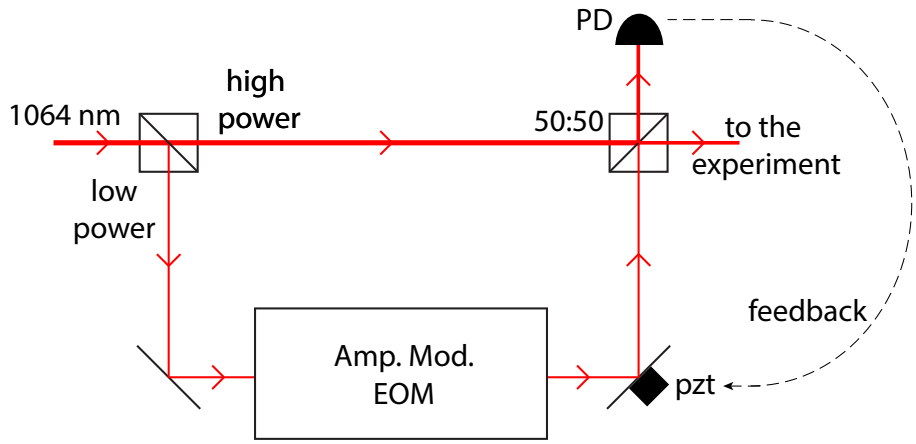

Figure 7.4: Schematic of the experimental setup for driving Rydberg transitions by lattice amplitude modulation. A Mach-Zehnder interferometer setup is used to lock a high-power beam in phase with a low-power beam that is modulated in intensity using a high-frequency EOM.

different signs at different regions within the lattice; if the atoms were able to travel through the lattice and sample many regions, evidence of transitions may be impossible to observe. We must therefore develop a way to perform a lattice modulation while maintaining a deep enough atom trap.

To achieve a deep atom trap with some amplitude modulation, we use an interferometric setup to combine a high-power beam in phase with a low-power, intensity-modulated beam. The setup is illustrated in Figure 7.4. A low-power beam is initially split from the high-power input. The low-power light is sent through the high-frequency EOM for intensity modulation. The high- and low-power arms are then recombined at the second, 50:50 beamsplitter. To lock the two arms in phase with one another, one of the mirrors in the interferometric setup is mounted on a piezoelectric transducer (pzt). The length of that arm can thereby be translated, changing the phase acquired by the beam in that arm. The interference signal at one output of the interferometer is monitored on a photodiode (PD). The interference signal is passed to electronics (a lock-in amplifier and a lockbox) that provide feedback to the pzt/mirror such that the two arms are kept in phase.

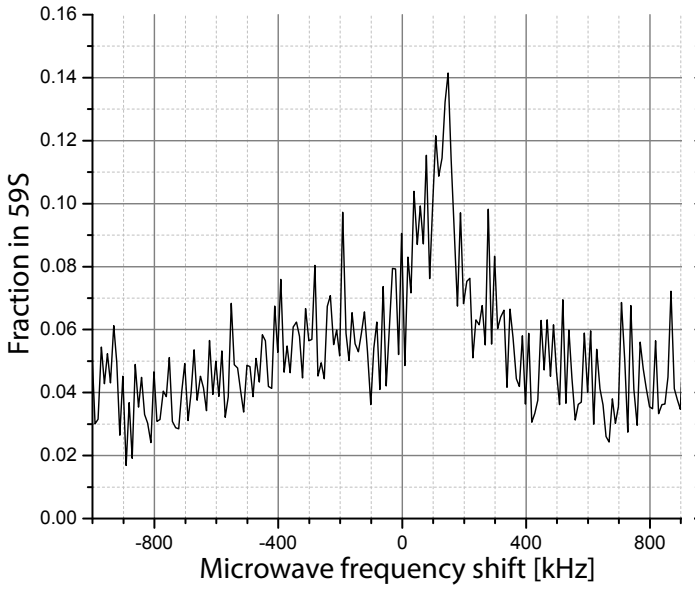

Figure 7.5: Experimental microwave spectrum for the $58S \rightarrow 59S$ transition, driven by lattice amplitude modulation.

While the interferometer plays the role of providing an atom trap while including some amplitude modulation for driving transitions, the method of combining the two beams has even more significance. By combining the two arms, we achieve a larger Rabi frequency than would be possible with a single amplitude-modulated beam alone. This can be seen by considering the Rabi frequency for this setup, which is proportional to $I_{\mathrm{lo}}(1+\sqrt{2I/I_{\mathrm{lo}}})$. Here, I_{lo} is the maximum intensity of the low-power, modulated arm of the interferometer, and I is the intensity of the high-power arm. In our setup, the ratio of high-to-low intensity (I/I_{lo}) at the output of the interferometer is about 130:1. Therefore, the Rabi frequency in our setup is about 17 times higher than it would be if the transitions were driven by a single amplitude-modulated beam.

In testing the new method, we have tried driving the $58S \rightarrow 59S$ transition by modulating the lattice intensity at frequencies near the one-photon transition frequency. The $58S \rightarrow 59S$ transition is chosen for these tests because of its high Rabi frequency (calculated in Reference [31]). Preliminary microwave spectroscopy results, acquired by K. Moore, are shown in Figure 7.5. We observe that transitions

are in fact driven from $58S \rightarrow 59S$, indicating that the lattice amplitude modulation technique is indeed effective in driving multipole Rydberg transitions. The x-axis in Figure 7.5 is scaled such that 0 corresponds to twice the two-photon frequency at which the lattice-free $58S \rightarrow 59S$ transition is observed ($\approx$ 38.77 GHz). The blue-shift of the signal in Figure 7.5 is likely due to lattice-induced shifts of the transition frequency for atoms located primarily near potential minima, along the lines of those described in Section 3.3 (a lattice inversion is performed in the experiments presented in Figure 7.5). Other preliminary results show that running the microwave generator with the amplitude-modulated light blocked (in the interferometric setup) results in no transitions. The transitions that we observe are therefore driven by amplitude-modulation of the lattice light and not by microwave radiation leaking into the chamber from the outside. Further experiments will involve driving higher order transitions, for example $\Delta\ell \geq 2$ transitions.

7.3 High-precision measurement of the Rydberg constant

An application that is enabled by the ponderomotive optical lattice, by both the lattice's Rydberg-atom trapping capability and the technique for driving Rydberg transitions by lattice amplitude modulation, is a high-precision measurement of the Rydberg constant. Measurements of fundamental constants, such as the Rydberg constant, are important because they test our current understanding of nature. By comparing theoretical and experimental values for the constants, we may assess existing theories. The Rydberg constant, R_∞, is an important fundamental constant because it is related to the fine structure constant, α, and other fundamental quantities, $R_\infty = \alpha/(4\pi a_0) = \alpha^2 m_e c/(4\pi\hbar)$. Previously, the Rydberg constant has been measured using one-electron quantum cyclotron experiments [99], atom interferometry [100], and precision measurements of transitions between low-lying states of hydrogen [101]. Note that these methods rely heavily on the accuracy and precision

of corrections based on QED calculations.

The Rydberg constant can also be extracted from high-precision measurements of transition frequencies between circular Rydberg states (which are Rydberg states of maximal angular momentum, see Section 1.2.2). The transition frequency is related to the Rydberg constant via $\Delta\nu = cR_\infty \frac{M}{m_\mathrm{e}+M}(\frac{1}{n_\mathrm{i}^2} - \frac{1}{n_\mathrm{f}^2})$, where M is the mass of the nucleus, m_e is the mass of the electron, and n_i and n_f are the principal quantum numbers of the initial and final circular Rydberg states, respectively. Circular Rydberg states are ideal for this precision measurement because of their long lifetimes (for example, $\tau = 30$ ms for $n = 50$ at 4 K) and their relative insensitivity to stray electric fields, both of which allow for the narrowest possible transition resonance linewidths. In addition, the electronic probability distributions of the circular Rydberg states take the shape of a thin torus that does not penetrate into the nuclear core, making corrections to the measured transition frequencies due to nuclear overlap, QED effects, fine structure, or hyperfine structure minimal.

Interest in a new measurement of the Rydberg constant has been kindled recently due to results from R. Pohl and co-workers [9], whose determination of the proton radius deviates from previously measured results (CODATA value [102]) by 5σ. The group concludes that in order to resolve this discrepancy either the value of the Rydberg constant must be shifted, or the QED calculations in atomic or muonic hydrogen are inadequate. A measurement of the Rydberg constant via spectroscopy of circular Rydberg states is therefore timely, as the method does not rely heavily on QED corrections (in contrast to previously mentioned measurements). It would thus provide an independent measurement that could be instrumental in resolving the current discrepancy.

An effort to measure the Rydberg constant through high-precision spectroscopy of circular-state Rydberg atoms in the ponderomotive optical lattice is underway in the Raithel research group. In our proposed procedure, cold ground-state ^{85}Rb

samples are first prepared in a shallow optical lattice. These atoms are excited to low-ℓ Rydberg states and then transformed into circular Rydberg states using either the $E \times B$ method [38, 103, 104] or the adiabatic rapid passage method [105, 106]. After this circularization procedure to prepare the initial state, transitions to a near-circular final state are driven by lattice intensity modulation, using the high-frequency EOM as described in Section 7.2. A promising target transition for the spectroscopy is $|n, n_1 = 0, n_2 = 0, |m| = n - 1\rangle \rightarrow |n + 2, n_1 = 1, n_2 = 1, |m| = n - 1\rangle$, where n_1 and n_2 are the parabolic quantum numbers (see Reference [26]) that are related to the spherical quantum numbers by $n = n_1 + n_2 + |m| + 1$. This transition is attractive because it has no linear Stark or Zeeman shifts. The transition is also an electric quadrupole transition, which requires the lattice amplitude modulation technique to drive in first order. After a long atom-field interaction time, the Rydberg-state distribution is measured through state-selective electric field ionization (see Section 2.2.2).

The ponderomotive optical lattice is an integral tool in this high-precision measurement. The technique for driving transitions by lattice amplitude modulation is critical for performing the spectroscopy, as described above. The lattice also allows for confinement of the atoms in a localized region where stray fields have been carefully minimized. The lattice is tailored so as to be minimally perturbing to the circular Rydberg states and so that the two states have identical lattice trapping potentials to cancel trap-induced shifts to the transition frequency. The ponderomotive optical lattice therefore plays an important role in propelling this method of measuring the Rydberg constant into competitive levels of precision.

The example given in this section of an imminent application of the ponderomotive optical lattice illustrates how the Rydberg-atom trap studied in this thesis is now developed to the point where it is ready to be used. The trap is now poised to make contributions with implications on our understanding of nature, through

high-precision measurements such as those described above, and on our ability to harness this understanding for our purposes, such as in quantum computing. In recent decades, the advent of laser cooling and trapping has revolutionized the study of atoms, offering not only a new process for investigating atoms but also an unprecedented means for controlling them. The work presented in this thesis provides an innovative approach that both augments and extends the reach of these powerful methods for laser-based cooling and manipulation of atoms.

APPENDICES

APPENDIX A

Atomic Units

Atomic units are designed to make calculations in atomic physics convenient. The units are defined such that all of the relevant parameters for the ground state of hydrogen are equal to 1. Analyzing Equation 1.3 for the energy of the ground state of hydrogen, one finds that in atomic units the electron charge e, the electron mass m_{e}, Planck's constant $\hbar$, and $1/(4\pi\epsilon_0)$ all have a magnitude of 1.

Table A.1 summarizes some of the conversion factors between atomic and SI units that are relevant to this thesis. As an example, the atomic unit of energy is the Hartree, E_{h}. To convert an energy calculated in atomic units to SI units, one must simply multiply by E_{h}, given in the Table. (Note that instead of remembering the value of a Hartree given in Joules below, it may be simpler to remember that one Hartree is twice the binding energy of the hydrogen ground state, or 27.2 eV.)

Table A.1: Atomic units.

Quantity	Definition	Value in SI units
Charge	Elementary charge, e	1.602×10^{-19} C
Mass	Electron mass, m_e	9.109×10^{-31} kg
Length	Bohr radius, a_0	0.529×10^{-10} m
Energy	Hartree, $E_\mathrm{h} = (\hbar^2)/(a_0^2 m_\mathrm{e})$	4.360×10^{-18} J
Electric field	$(\hbar^2)/(a_0^3 m_\mathrm{e} e)$	5.142×10^{11} V/m
Electric potential	$(\hbar^2)/(a_0^2 m_\mathrm{e} e)$	27.21 V
Dipole moment	$e\, a_0$	8.478×10^{-30} C·m
Polarizability	$4\pi\epsilon_0 a_0^3$	1.649×10^{-41} $\mathrm{C^2 m^4/J}$

APPENDIX B

Determining $5S$ and Rydberg Level Shifts

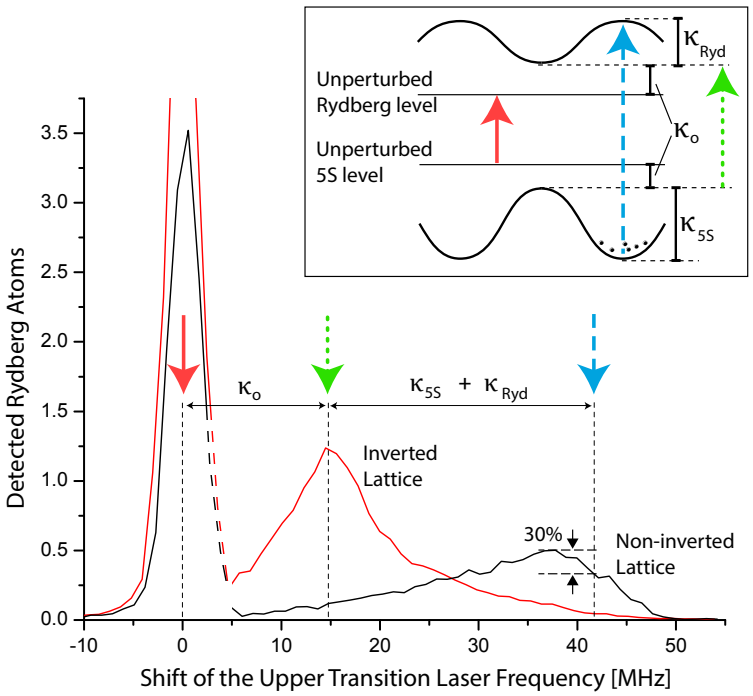

Figure B.1: Optical excitation spectra for level 2 of Figure 4.3 in a transverse DC field and a non-inverted lattice and inverted lattice. Spectral features, indicated by arrows, enable a measurement of the Rydberg-state lattice depth (κ_{Ryd}).

To determine the $5S$- and Rydberg-state modulation depths (κ_{o} and κ_{Ryd}, respectively) in Chapter IV, we use a combination of experimental results and calculations. From the experiment, we obtain a measurement of $\kappa_{\mathrm{o}} + \kappa_{5\mathrm{S}} + \kappa_{\mathrm{Ryd}}$ from the optical

excitation spectrum in the lattice without inversion and a measurement of κ_{o} from the optical spectrum in the lattice with inversion, as described in Section 4.2.2 and illustrated again in Figure B.1 above. By subtracting these two measurements, we obtain

$$\Delta\kappa = \kappa_{5\mathrm{S}} + \kappa_{\mathrm{Ryd}}. \tag{B.1}$$

In our calculations, we compute the modulation depth for the Rydberg level in the lattice, $\kappa_{\mathrm{Ryd,C}}$, assuming a free-electron ponderomotive modulation depth of 20 MHz. The depth of the Rydberg level and the $5S$ level are then related by the ratio

$$\beta = \left(\frac{|\alpha_{\mathrm{p}}|}{|\alpha_{5\mathrm{S}}|}\right) \cdot \left(\frac{\kappa_{\mathrm{Ryd,C}}}{20\ \mathrm{MHz}}\right), \tag{B.2}$$

so that $\kappa_{\mathrm{Ryd}} = \beta\kappa_{5\mathrm{S}}$. Here, α_{p} is the free-electron polarizability and is equal to $-4\pi\epsilon_0 \times 545a_0^3$ in SI units at 1064 nm. The polarizability of the $5S$ ground-state $\alpha_{5\mathrm{S}} = 4\pi\epsilon_0 \times 711a_0^3$ in SI units at 1064 nm [71].

Therefore, with the experimentally determined $\Delta\kappa$ in Equation B.1 and the calculated value of β in Equation B.2, we extract κ_{Ryd} and $\kappa_{5\mathrm{S}}$.

BIBLIOGRAPHY

BIBLIOGRAPHY

[1] A. Reinhard, T. Cubel Liebisch, B. Knuffman, and G. Raithel. Level shifts of rubidium rydberg states due to binary interactions. *Phys. Rev. A*, 75:032712, Mar 2007.

[2] D. Jaksch, J. I. Cirac, P. Zoller, S. L. Rolston, R. Côté, and M. D. Lukin. Fast quantum gates for neutral atoms. *Phys. Rev. Lett.*, 85:2208–2211, Sep 2000.

[3] M. D. Lukin, M. Fleischhauer, R. Cote, L. M. Duan, D. Jaksch, J. I. Cirac, and P. Zoller. Dipole blockade and quantum information processing in mesoscopic atomic ensembles. *Phys. Rev. Lett.*, 87:037901, Jun 2001.

[4] M. Saffman, T. G. Walker, and K. Mølmer. Quantum information with rydberg atoms. *Rev. Mod. Phys.*, 82:2313–2363, Aug 2010.

[5] X. L. Zhang, L. Isenhower, A. T. Gill, T. G. Walker, and M. Saffman. Deterministic entanglement of two neutral atoms via rydberg blockade. *Phys. Rev. A*, 82:030306, Sep 2010.

[6] T. Wilk, A. Gaëtan, C. Evellin, J. Wolters, Y. Miroshnychenko, P. Grangier, and A. Browaeys. Entanglement of two individual neutral atoms using rydberg blockade. *Phys. Rev. Lett.*, 104:010502, Jan 2010.

[7] L. Isenhower, E. Urban, X. L. Zhang, A. T. Gill, T. Henage, T. A. Johnson, T. G. Walker, and M. Saffman. Demonstration of a neutral atom controlled-not quantum gate. *Phys. Rev. Lett.*, 104:010503, Jan 2010.

[8] I. Mourachko, D. Comparat, F. de Tomasi, A. Fioretti, P. Nosbaum, V. M. Akulin, and P. Pillet. Many-body effects in a frozen rydberg gas. *Phys. Rev. Lett.*, 80:253–256, Jan 1998.

[9] T. Pohl, E. Demler, and M. D. Lukin. Dynamical crystallization in the dipole blockade of ultracold atoms. *Phys. Rev. Lett.*, 104:043002, Jan 2010.

[10] A. Schwarzkopf, R. E. Sapiro, and G. Raithel. Imaging spatial correlations of rydberg excitations in cold atom clouds. *Phys. Rev. Lett.*, 107:103001, Aug 2011.

[11] Peter Schauß, Marc Cheneau, Manuel Endres, Takeshi Fukuhara, Sebastian Hild, Ahmed Omran, Thomas Pohl, Christian Gross, Stefan Kuhr, and Immanuel Bloch. Observation of spatially ordered structures in a two-dimensional rydberg gas. *Nature*, 491:87–91, Nov 2012.

[12] Serge Haroche and Jean-Michel Raimond. *Exploring the Quantum: Atoms, Cavities, and Photons*. Oxford University Press, 1 edition, 2006.

[13] B. Olmos, R. González-Férez, and I. Lesanovsky. Fermionic collective excitations in a lattice gas of rydberg atoms. *Phys. Rev. Lett.*, 103:185302, Oct 2009.

[14] Hendrik Weimer, Markus Muller, Igor Lesanovsky, Peter Zoller, and Hans Peter Buchler. A rydberg quantum simulator. *Nat. Phys.*, 6:382–388, May 2010.

[15] Jonathon A. Sedlacek, Arne Schwettmann, Harald Kubler, Robert Löw, Tilman Pfau, and James P. Shaffer. Microwave electrometry with rydberg atoms in a vapour cell using bright atomic resonances. *Nat. Phys.*, 8:819–824, Nov 2012.

[16] A. Osterwalder and F. Merkt. Using high rydberg states as electric field sensors. *Phys. Rev. Lett.*, 82:1831–1834, Mar 1999.

[17] Ulrich D. Jentschura, Peter J. Mohr, Joseph N. Tan, and Benedikt J. Wundt. Fundamental constants and tests of theory in rydberg states of hydrogenlike ions. *Phys. Rev. Lett.*, 100:160404, Apr 2008.

[18] G. Gabrielse, S.L. Rolston, L. Haarsma, and W. Kells. Antihydrogen production using trapped plasmas. *Physics Letters A*, 129(1):38 – 42, 1988.

[19] G.B. Andresen, M.D. Ashkezari, M. Baquero-Ruiz, W. Bertsche, P.D. Bowe, C.C. Bray, E. Butler, C.L. Cesar, S. Chapman, M. Charlton, J. Fajans, T. Friesen, M.C. Fujiwara, D.R. Gill, J.S. Hangst, W.N. Hardy, R.S. Hayano, M.E. Hayden, A.J. Humphries, R. Hydomako, S. Jonsell, L.V. Jrgensen, L. Kurchaninov, R. Lambo, N. Madsen, S. Menary, P. Nolan, K. Olchanski, A. Olin, A. Povilus, P. Pusa, F. Robicheaux, E. Sarid, S. Seif El Nasr, D.M. Silveira, C. So, J.W. Storey, R.I. Thompson, D.P. van der Werf, D. Wilding, J.S. Wurtele, and Y. Yamazaki. Search for trapped antihydrogen. *Physics Letters B*, 695(14):95 – 104, 2011.

[20] J. M. Raimond, M. Brune, and S. Haroche. Manipulating quantum entanglement with atoms and photons in a cavity. *Rev. Mod. Phys.*, 73:565–582, Aug 2001.

[21] S. Haroche, M. Brune, and J.-M. Raimond. Schrodinger cat states and decoherence studies in cavity qed. *The European Physical Journal Special Topics*, 159(1):19–26, 2008.

[22] T.C. Killian, T. Pattard, T. Pohl, and J.M. Rost. Ultracold neutral plasmas. *Physics Reports*, 449(45):77 – 130, 2007.

[23] M. Robert-de Saint-Vincent, C. S. Hofmann, H. Schempp, G. Günter, S. Whitlock, and M. Weidemüller. Spontaneous avalanche ionization of a strongly blockaded rydberg gas. *Phys. Rev. Lett.*, 110:045004, Jan 2013.

[24] Chris H. Greene, A. S. Dickinson, and H. R. Sadeghpour. Creation of polar and nonpolar ultra-long-range rydberg molecules. *Phys. Rev. Lett.*, 85:2458–2461, Sep 2000.

[25] W. Li, T. Pohl, J. M. Rost, Seth T. Rittenhouse, H. R. Sadeghpour, J. Nipper, B. Butscher, J. B. Balewski, V. Bendkowsky, R. Löw, and T. Pfau. A homonuclear molecule with a permanent electric dipole moment. *Science*, 334(6059):1110–1114, 2011.

[26] Thomas F. Gallagher. *Rydberg Atoms*. Cambridge University Press, 1994.

[27] Wenhui Li, I. Mourachko, M. W. Noel, and T. F. Gallagher. Millimeter-wave spectroscopy of cold rb rydberg atoms in a magneto-optical trap: Quantum defects of the *ns*, *np*, and *nd* series. *Phys. Rev. A*, 67:052502, May 2003.

[28] Richard R. Freeman and Daniel Kleppner. Core polarization and quantum defects in high-angular-momentum states of alkali atoms. *Phys. Rev. A*, 14:1614–1619, Nov 1976.

[29] Jianing Han, Yasir Jamil, D. V. L. Norum, Paul J. Tanner, and T. F. Gallagher. Rb *nf* quantum defects from millimeter-wave spectroscopy of cold ^{85}rb rydberg atoms. *Phys. Rev. A*, 74:054502, Nov 2006.

[30] S. Zhang, F. Robicheaux, and M. Saffman. Magic-wavelength optical traps for rydberg atoms. *Phys. Rev. A*, 84:043408, Oct 2011.

[31] B. Knuffman and G. Raithel. Multipole transitions of rydberg atoms in modulated ponderomotive potentials. *Phys. Rev. A*, 75:053401, May 2007.

[32] A. Gaetan, Y. Miroshnychenko, T. Wilk, A. Chotia, M. Viteau, D. Comparat, P. Pillet, A. Browaeys, and P. Grangier. Observation of collective excitation of two individual atoms in the rydberg blockade regime. *Nat. Phys.*, 5:115–118, Feb 2009.

[33] M. S. Safronova, Carl J. Williams, and Charles W. Clark. Optimizing the fast rydberg quantum gate. *Phys. Rev. A*, 67:040303, Apr 2003.

[34] William H. Wing. Electrostatic trapping of neutral atomic particles. *Phys. Rev. Lett.*, 45:631–634, Aug 1980.

[35] Thomas Breeden and Harold Metcalf. Stark acceleration of rydberg atoms in inhomogeneous electric fields. *Phys. Rev. Lett.*, 47:1726–1729, Dec 1981.

[36] S. D. Hogan and F. Merkt. Demonstration of three-dimensional electrostatic trapping of state-selected rydberg atoms. *Phys. Rev. Lett.*, 100:043001, Jan 2008.

[37] J.-H. Choi, J. R. Guest, A. P. Povilus, E. Hansis, and G. Raithel. Magnetic trapping of long-lived cold rydberg atoms. *Phys. Rev. Lett.*, 95:243001, Dec 2005.

[38] D. A. Anderson, A. Schwarzkopf, R. E. Sapiro, and G. Raithel. Production and trapping of cold circular rydberg atoms. *Phys. Rev. A*, 88:031401, Sep 2013.

[39] Igor Lesanovsky and Peter Schmelcher. Magnetic trapping of ultracold rydberg atoms. *Phys. Rev. Lett.*, 95:053001, Jul 2005.

[40] S. K. Dutta, J. R. Guest, D. Feldbaum, A. Walz-Flannigan, and G. Raithel. Ponderomotive optical lattice for rydberg atoms. *Phys. Rev. Lett.*, 85:5551–5554, Dec 2000.

[41] K. C. Younge, B. Knuffman, S. E. Anderson, and G. Raithel. State-dependent energy shifts of rydberg atoms in a ponderomotive optical lattice. *Phys. Rev. Lett.*, 104:173001, Apr 2010.

[42] P.H. Bucksbaum. Atoms in intense optical fields: Ponderomotive forces and above-threshold ionization. In K.T. Taylor, M.H. Nayfeh, and C.W. Clark, editors, *Atomic Spectra and Collisions in External Fields*, Physics of Atoms and Molecules, pages 359–373. Springer US, 1988.

[43] George Schmidt. *Physics of High Temperature Plasmas*. Academic Press, Inc., 3 edition, 1979.

[44] Ernest S. Abers. *Quantum Mechanics*. Addison-Wesley, 1 edition, 2003.

[45] Harald Friedrich. *Theoretical Atomic Physics*. Springer, 3 edition, 1965.

[46] John David Jackson. *Classical Electrodynamics*. John Wiley and Sons, Inc., 3 edition, 1999.

[47] Daniel L. Freimund, Kayvan Aflatooni, and Herman Batelaan. Observation of the kapitza-dirac effect. *Nature*, 413:142–143, Sept 2001.

[48] Wolfgang Paul. Electromagnetic traps for charged and neutral particles. *Rev. Mod. Phys.*, 62:531–540, Jul 1990.

[49] Antoine Rousse, Kim Ta Phuoc, Rahul Shah, Alexander Pukhov, Eric Lefebvre, Victor Malka, Sergey Kiselev, Fréderic Burgy, Jean-Philippe Rousseau, Donald Umstadter, and Daniéle Hulin. Production of a kev x-ray beam from synchrotron radiation in relativistic laser-plasma interaction. *Phys. Rev. Lett.*, 93:135005, Sep 2004.

[50] Alexander Pukhov. Strong field interaction of laser radiation. *Reports on Progress in Physics*, 66(1):47, 2003.

[51] James West and Carlos Stroud. Visualization of the core-scattering dynamics of rydberg wave packets. *Opt. Express*, 1(1):31–39, Jul 1997.

[52] J.C. Gay and D. Delande. The hydrogen atom in a magnetic field. symmetries in the low field diamagnetic limit. *Comments At. Mol. Phys.*, 13(6):275–279, 1837.

[53] Kelly Cooper Younge, Sarah Elizabeth Anderson, and Georg Raithel. Adiabatic potentials for rydberg atoms in a ponderomotive optical lattice. *New Journal of Physics*, 12(2):023031, 2010.

[54] Harold J. Metcalf and Peter van der Straten. *Laser Cooling and Trapping*. Springer, 1999.

[55] R. Mukherjee, J. Millen, R. Nath, M. P. A. Jones, and T. Pohl. Many-body physics with alkaline-earth rydberg lattices. *Journal of Physics B: Atomic, Molecular and Optical Physics*, 44(18):184010, 2011.

[56] William D. Phillips and Harold Metcalf. Laser deceleration of an atomic beam. *Phys. Rev. Lett.*, 48:596–599, Mar 1982.

[57] Steven Chu, J. E. Bjorkholm, A. Ashkin, and A. Cable. Experimental observation of optically trapped atoms. *Phys. Rev. Lett.*, 57:314–317, Jul 1986.

[58] E. L. Raab, M. Prentiss, Alex Cable, Steven Chu, and D. E. Pritchard. Trapping of neutral sodium atoms with radiation pressure. *Phys. Rev. Lett.*, 59:2631–2634, Dec 1987.

[59] M. Saffman and T. G. Walker. Analysis of a quantum logic device based on dipole-dipole interactions of optically trapped rydberg atoms. *Phys. Rev. A*, 72:022347, Aug 2005.

[60] Christopher J. Foote. *Atomic Physics*. Oxford University Press, 2005.

[61] Rudolf Grimm, Matthias Weidemller, and Yurii B. Ovchinnikov. Optical dipole traps for neutral atoms. volume 42 of *Advances In Atomic, Molecular, and Optical Physics*, pages 95 – 170. Academic Press, 2000.

[62] C.J. Hawthorn, K.P. Weber, and R.E. Scholten. Littrow configuration tunable external cavity diode laser with fixed direction output beam. *Rev. Sci. Instrum.*, 72:4477–4479, Sept 2001.

[63] P. A. Franken, A. E. Hill, C. W. Peters, and G. Weinreich. Generation of optical harmonics. *Phys. Rev. Lett.*, 7:118–119, Aug 1961.

[64] E. Hansis, T. Cubel, J.-H. Choi, J. R. Guest, and G. Raithel. Simple pressure-tuned fabry-pérot interferometer. *Review of Scientific Instruments*, 76(3):–, 2005.

[65] Joseph Ladislas Wiza. Microchannel plate detectors. *Nuclear Instruments and Methods*, 162(13):587 – 601, 1979.

[66] S. E. Anderson, K. C. Younge, and G. Raithel. Trapping rydberg atoms in an optical lattice. *Phys. Rev. Lett.*, 107:263001, Dec 2011.

[67] Charles S. Adams, Heun Jin Lee, Nir Davidson, Mark Kasevich, and Steven Chu. Evaporative cooling in a crossed dipole trap. *Phys. Rev. Lett.*, 74:3577–3580, May 1995.

[68] Dieter Meschede and Arno Rauschenbeutel. Manipulating single atoms. volume 53 of *Advances In Atomic, Molecular, and Optical Physics*, pages 75 – 104. Academic Press, 2006.

[69] E. Urban, T. A. Johnson, T. Henage, L. Isenhower, D. D. Yavuz, T. G. Walker, and M. Saffman. Observation of rydberg blockade between two atoms. *Nat. Phys.*, 5:110–114, Feb 2009.

[70] Turker Topcu and Andrei Derevianko. Intensity landscape and the possibility of magic trapping of alkali-metal rydberg atoms in infrared optical lattices. *Phys. Rev. A*, 88:043407, Oct 2013.

[71] M. Marinescu, H. R. Sadeghpour, and A. Dalgarno. Dynamic dipole polarizabilities of rubidium. *Phys. Rev. A*, 49:5103–5104, Jun 1994.

[72] Amnon Yariv and Pochi Yeh. *Optical Waves in Crystals: Propagation and Control of Laser Radiation*. John Wiley and Sons, Inc., 2003.

[73] Kelly Cooper Younge, Sarah Elizabeth Anderson, and Georg Raithel. Rydberg-atom trajectories in a ponderomotive optical lattice. *New Journal of Physics*, 12(2):113036, 2010.

[74] I. I. Beterov, I. I. Ryabtsev, D. B. Tretyakov, and V. M. Entin. Quasiclassical calculations of blackbody-radiation-induced depopulation rates and effective lifetimes of rydberg ns, np, and nd alkali-metal atoms with $n \leq 80$. *Phys. Rev. A*, 79:052504, May 2009.

[75] J. Dalibard and C. Cohen-Tannoudji. Laser cooling below the doppler limit by polarization gradients: simple theoretical models. *J. Opt. Soc. Am. B*, 6(11):2023–2045, Nov 1989.

[76] P. J. Ungar, D. S. Weiss, E. Riis, and Steven Chu. Optical molasses and multilevel atoms: theory. *J. Opt. Soc. Am. B*, 6(11):2058–2071, Nov 1989.

[77] P.S. Jessen and I.H. Deutsch. Optical lattices. volume 37 of *Advances In Atomic, Molecular, and Optical Physics*, pages 95 – 138. Academic Press, 1996.

[78] O. Hemmers, R. Guillemin, E. P. Kanter, B. Krässig, D. W. Lindle, S. H. Southworth, R. Wehlitz, J. Baker, A. Hudson, M. Lotrakul, D. Rolles, W. C. Stolte, I. C. Tran, A. Wolska, S. W. Yu, M. Ya. Amusia, K. T. Cheng, L. V. Chernysheva, W. R. Johnson, and S. T. Manson. Dramatic nondipole effects in low-energy photoionization: Experimental and theoretical study of xe $5s$. *Phys. Rev. Lett.*, 91:053002, Aug 2003.

[79] J. Tallant, D. Booth, and J. P. Shaffer. Photoionization rates of cs rydberg atoms in a 1064-nm far-off-resonance trap. *Phys. Rev. A*, 82:063406, Dec 2010.

[80] U. Fano. Propensity rules: An analytical approach. *Phys. Rev. A*, 32:617–618, Jul 1985.

[81] A. Giusti-Suzor and P. Zoller. Rydberg electrons in laser fields: A finite-range-interaction problem. *Phys. Rev. A*, 36:5178–5188, Dec 1987.

[82] H. B. van Linden van den Heuvell, H. G. Muller, J. W. J. Verschuur, and A. ten Wolde. Time domain effects in photoionisation of rydberg atoms. *J. Phys. B: At. Mol. Phys.*, 20(16):L517–L524, 1987.

[83] A. ten Wolde, L. D. Noordam, A. Lagendijk, and H. B. van Linden van den Heuvell. Observation of radially localized atomic electron wave packets. *Phys. Rev. Lett.*, 61:2099–2101, Oct 1988.

[84] John A. Yeazell, Mark Mallalieu, and C. R. Stroud. Observation of the collapse and revival of a rydberg electronic wave packet. *Phys. Rev. Lett.*, 64:2007–2010, Apr 1990.

[85] R. M. Potvliege and C. S. Adams. Photo-ionization in far-off-resonance optical lattices. *New J. Phys.*, 8:163, 2006.

[86] G. Leuchs, S. J. Smith, S. N. Dixit, and P. Lambropoulos. Observation of interference between quadrupole and dipole transitions in low-energy (2-ev) photoionization from a sodium rydberg state. *Phys. Rev. Lett.*, 56:708–711, Feb 1986.

[87] S. E. Anderson and G. Raithel. Dependence of rydberg-atom optical lattices on the angular wave function. *Phys. Rev. Lett.*, 109:023001, Jul 2012.

[88] Sarah E. Anderson and Georg Raithel. Ionization of rydberg atoms by standing-wave light fields. *Nat. Comm.*, 4(2967):1–7, Dec 2013.

[89] L. D. Noordam and R. R. Jones. Probing rydberg electron dynamics. *J. of Mod. Opt.*, 44:2515–2532, 1997.

[90] Hans A. Bethe and Edwin E. Salpeter. *Quantum Mechanics of One- and Two-Electron Atoms*. Dover Publications, 2008.

[91] H. G. Muller and H. B. van Linden van den Heuvell. A new gauge for convenient description of photoionization. *Laser Physics*, 3(3):694–698, 1993.

[92] J. J. Sakuri. *Advanced Quantum Mechanics*. Addison-Wesley Publishing Company, Inc., 1967.

[93] Myron L. Zimmerman, Jarbas C. Castro, and Daniel Kleppner. Diamagnetic structure of na rydberg states. *Phys. Rev. Lett.*, 40:1083–1086, Apr 1978.

[94] P. Cacciani, E. Luc-Koenig, J. Pinard, C. Thomas, and S. Liberman. Experimental studies of a diamagnetic multiplet in odd rydberg states of lithium. *Phys. Rev. Lett.*, 56:1124–1127, Mar 1986.

[95] T. van der Veldt, W. Vassen, and W. Hogervorst. Helium rydberg states in parallel electric and magnetic fields. *Journal of Physics B: Atomic, Molecular and Optical Physics*, 26(13):1945, 1993.

[96] L. Isenhower, W. Williams, A. Dally, and M. Saffman. Atom trapping in an interferometrically generated bottle beam trap. *Opt. Lett.*, 34(8):1159–1161, Apr 2009.

[97] William T. Silfvast. *Laser Fundamentals*. Cambridge University Press, 2 edition, 2004.

[98] J. Liang, M. Gross, P. Goy, and S. Haroche. Circular rydberg-state spectroscopy. *Phys. Rev. A*, 33:4437–4439, Jun 1986.

[99] D. Hanneke, S. Fogwell, and G. Gabrielse. New measurement of the electron magnetic moment and the fine structure constant. *Phys. Rev. Lett.*, 100:120801, Mar 2008.

[100] Rym Bouchendira *et al.* New determination of the fine structure constant and test of the quantum electrodynamics. *Phys. Rev. Lett.*, 106:080801, Feb 2011.

[101] Christian G. Parthey, Arthur Matveev, Janis Alnis, Birgitta Bernhardt, Axel Beyer, Ronald Holzwarth, Aliaksei Maistrou, Randolf Pohl, Katharina Predehl, Thomas Udem, Tobias Wilken, Nikolai Kolachevsky, Michel Abgrall, Daniele Rovera, Christophe Salomon, Philippe Laurent, and Theodor W. Hänsch. Improved measurement of the hydrogen $1s - 2s$ transition frequency. *Phys. Rev. Lett.*, 107:203001, Nov 2011.

[102] Peter J. Mohr, Barry N. Taylor, and David B. Newell. Codata recommended values of the fundamental physical constants: 2006. *Rev. Mod. Phys.*, 80:633–730, Jun 2008.

[103] J. Hare, M. Gross, and P. Goy. Circular atoms prepared by a new method of crossed electric and magnetic fields. *Phys. Rev. Lett.*, 61:1938–1941, Oct 1988.

[104] R.J. Brecha, G. Raithel, C. Wagner, and H. Walther. Circular rydberg states with very large n. *Optics Communications*, 102(34):257 – 264, 1993.

[105] Randall G. Hulet and Daniel Kleppner. Rydberg atoms in "circular" states. *Phys. Rev. Lett.*, 51:1430–1433, Oct 1983.

[106] A. Nussenzweig, J. Hare, A. M. Steinberg, L. Moi, M. Gross, and S. Haroche. A continuous beam of circular rydberg atoms for fundamental tests and applications in metrology. *EPL (Europhysics Letters)*, 14(8):755, 1991.